

SURFACE MODIFICATION OF MULTI-CRYSTALLINE SILICON IN
PHOTOVOLTAIC CELL BY LASER TEXTURING

A THESIS SUBMITTED TO
THE GRADUATE SCHOOL OF NATURAL AND APPLIED SCIENCES
OF
MIDDLE EAST TECHNICAL UNIVERSITY

BY

BEHRAD RADFAR

IN PARTIAL FULFILLMENT OF THE REQUIREMENTS
FOR
THE DEGREE OF MASTER OF SCIENCE
IN
MICRO AND NANOTECHNOLOGY

JANUARY 2019

Approval of the thesis:

**SURFACE MODIFICATION OF MULTI-CRYSTALLINE SILICON IN
PHOTOVOLTAIC CELL BY LASER TEXTURING**

submitted by **BEHRAD RADFAR** in partial fulfillment of the requirements for the degree of **Master of Science in Micro and Nanotechnology Department, Middle East Technical University** by,

Prof. Dr. Halil Kalıpçılar
Dean, Graduate School of **Natural and Applied Sciences**

Prof. Dr. Almıla Güvenç Yazıcıoğlu
Head of Department, **Micro and Nanotechnology**

Prof. Dr. Raşit Turan
Supervisor, **Micro and Nanotechnology, METU**

Assist. Prof. Dr. Selçuk Yerci
Co-Supervisor, **Micro and Nanotechnology, METU**

Examining Committee Members:

Prof. Dr. Hüsni Emrah Ünalın
Micro and Nanotechnology, Middle East Technical University

Prof. Dr. Raşit Turan
Micro and Nanotechnology, METU

Assoc. Prof. Dr. Alpan Bek
Micro and Nanotechnology, Middle East Technical University

Prof. Dr. Barış Akaoğlu
Physics Engineering Department, Ankara University

Assist. Prof. Dr. Ihor Pavlov
Department of Physics, Middle East Technical University

Date: 03.01.2019

I hereby declare that all information in this document has been obtained and presented in accordance with academic rules and ethical conduct. I also declare that, as required by these rules and conduct, I have fully cited and referenced all material and results that are not original to this work.

Name, Surname: Behrad Radfar

Signature:

ABSTRACT

SURFACE MODIFICATION OF MULTI-CRYSTALLINE SILICON IN PHOTOVOLTAIC CELL BY LASER TEXTURING

Radfar, Behrad
Master of Science, Micro and Nanotechnology
Supervisor: Prof. Dr. Raşit Turan
Co-Supervisor: Assist. Prof. Dr. Selçuk Yerci

January 2019, 127 pages

Surface of crystalline silicon solar cell plays an important role in its performance. It affects the optical properties which can be determined by surface' reflectance. To minimize the reflection from the flat surface, thus, improve light trapping, the crystalline silicon wafers must be textured. Through the texturing process, roughness is introduced at the surface, so the incident light has a larger probability of being absorbed into the solar cell. Monocrystalline silicon solar cells can typically be textured using anisotropic alkaline etchants which create randomly distributed pyramids on the surface. However, most of the texturing methods used for monocrystalline silicon wafer are not suitable for multi-crystalline silicon wafer due to grains of random crystallographic orientations. Therefore, isotropic texturing methods are developed. Laser texturing is an isotropic texturing process which utilizes a laser to create pits on the front surface of monocrystalline and multi-crystalline silicon wafers. Then, a special etching procedure should be applied to remove laser-induced damages and other residues. In the following work, the laser processing parameters are going to be justified experimentally. Later, the post texture cleaning process is to be optimized to obtain the required surface morphology. In order to determine the effectiveness of proposed methods, the reflectance and scanning

electron microscopy (SEM) images of the textured surface are going to be considered. The aim of the work is finding optimum parameters for laser texturing and also, for post-texture cleaning to improve the efficiency of multi-crystalline silicon solar cell.

Keywords: Solar Cell, Crystalline Silicon, Surface Modification, Laser Texturing

ÖZ

FOTOVOLTAİK HÜCRELERDE ÇOK KRİSTALLİ SİLİSYUMUN LAZER DOKULAMA İLE YÜZEY MODİFİKASYONU

Radfar, Behrad
Yüksek Lisans, Mikro ve Nanoteknoloji
Tez Danışmanı: Prof. Dr. Raşit Turan
Ortak Tez Danışmanı: Dr. Öğr. Üyesi Selçuk Yerci

Ocak 2019, 127 sayfa

Kristal silisyum güneş hücresinin yüzeyi, performansında önemli bir rol oynamaktadır. Yüzey, optik özellikleri etkiler ve bunu yüzeyin yansıması ile belirtebiliriz. Düz yüzeyden yansımayı en aza indirmek ve böylece ışığı yakalamayı iyileştirmek için kristal silisyum gofretler dokulu olmalıdır. Doku işleme yöntemiyle, yüzeyde pürüzlülük ortaya çıkmaktadır, bu yüzden gelen ışık güneş hücresine emilme olasılığını artmaktadır. Monokristal silisyum güneş hücreleri tipik olarak yüzeyde rastgele dağılmış piramitler yaratan anizotropik alkalın eterler kullanılarak dokulu edilebilir. Ancak, monokristal silisyum gofret için kullanılan dokulu etme yöntemlerinin çoğu, rastgele kristalografik yönelimli taneleri nedeniyle çok kristalli silisyum gofret için uygun değildir. Bu nedenle izotropik dokulama yöntemleri geliştirilmiştir. Lazer dokulama, monokristal ve çok kristalli silisyum gofretlerin ön yüzeyinde çukurlar oluşturmak için bir dokulama yöntemidir. Daha sonra, lazer kaynaklı hasarları ve diğer kalıntıları gidermek için özel bir aşındırma işlemi uygulanmalıdır. Aşağıdaki çalışmada, lazer işleme parametreleri deneysel olarak gerekçelendirilmektedir. Daha sonra, doku sonrası temizlik işlemi, istenen yüzey morfolojisini elde etmek için optimize edilmelidir. Önerilen yöntemlerin etkisini belirlemek için, dokulu yüzeyin yansıtma ve taramalı elektron mikroskobu (SEM)

görüntüleri dikkate alınacaktır. Çalışmanın amacı, lazer dokulama için ve ayrıca çok kristalli silisyum güneş hücrenin verimliliğini arttırmak için doku sonrası temizlik için en uygun parametreleri bulmaktır.

Anahtar Kelimeler: Güneş Pili, Kristalli Silikon, Yüzey Modifikasyonu, Lazer
Tekstüre

To my Dearest Dear & Family who support me all the times

ACKNOWLEDGMENTS

I want to gratefully thank my advisor Prof. Dr. Raşit Turan for his ultimate support through my study and giving me the opportunity to perform my experiments in GUNAM. I want to thank Dr. Firat Es from whom I have learned a lot.

I want to thank my dear friend Shokoofeh Parvin and my family for their patience all these years and supporting me by all means.

I acknowledge Hande Ciftpinar and Gulsen Baytemir for their contribution to solar cell fabrication steps and TUBITAK for partially funding the experiments. I want to thank my friends Seyedehnasim Seyedpour Esmailzad, Mona Zolfaghari Borra, Parisa Sharif for their assistance.

TABLE OF CONTENTS

| | |
|--|-------|
| ABSTRACT | v |
| ÖZ | vii |
| ACKNOWLEDGMENTS | x |
| TABLE OF CONTENTS | xi |
| LIST OF TABLES | xv |
| LIST OF FIGURES | xvii |
| LIST OF ABBREVIATIONS | xxv |
| LIST OF SYMBOLS | xxvii |
| 1. INTRODUCTION | 1 |
| 1.1. Importance of Energy | 1 |
| 1.2. Properties of Solar Energy | 3 |
| 1.3. Physics of Photovoltaic Devices | 5 |
| 1.3.1. Materials | 5 |
| 1.3.1.1. Metals | 6 |
| 1.3.1.2. Semiconductors | 6 |
| 1.3.1.3. Insulators | 7 |
| 1.3.2. Doping | 7 |
| 1.3.3. Junctions | 8 |
| 1.3.3.1. Metal-Semiconductor (Ohmic / Schottky Junction) | 8 |
| 1.3.3.2. P-N Junction | 10 |
| 1.4. Solar Cells | 12 |
| 1.4.1. Solar Cell Working Principles | 12 |

| | |
|--|----|
| 1.4.2. Different Types of Solar Cells..... | 17 |
| 1.4.2.1. Crystalline Si Solar Cells..... | 18 |
| 1.4.2.2. Thin Film Solar Cells..... | 19 |
| 1.4.2.3. Emerging Photovoltaics..... | 20 |
| 1.4.3. Solar Cell Fabrication Steps | 21 |
| 1.4.3.1. Wafer Preparation..... | 21 |
| 1.4.3.2. Texturing..... | 22 |
| 1.4.3.3. Doping | 24 |
| 1.4.3.4. Anti -Reflection Coating..... | 24 |
| 1.4.3.5. Metallization..... | 26 |
| 2. A LITERARURE SURVEY ON SURFACE TEXTURING OF SI WAFER... | 29 |
| 2.1. Solar Cells..... | 29 |
| 2.2. Texturing..... | 30 |
| 2.2.1. Mono Crystalline..... | 30 |
| 2.2.2. Multi Crystalline..... | 31 |
| 2.3. Laser Texturing with Post-Texture Cleaning..... | 34 |
| 3. EXPERIMENTAL METHODS | 41 |
| 3.1. Introduction..... | 41 |
| 3.2. Laser Texturing | 42 |
| 3.3. Post-Texture Cleaning..... | 44 |
| 3.4. Solar Cell Fabrication | 45 |
| 3.4.1. Wafer Preparation..... | 45 |
| 3.4.2. Texturing | 45 |
| 3.4.3. Doping..... | 46 |

| | |
|--|----|
| 3.4.4. ARC Deposition..... | 46 |
| 3.4.5. Metallization | 46 |
| 3.4.6. Cleaning Step..... | 47 |
| 3.5. Characterization Methods..... | 47 |
| 3.5.1. Scanning Electron Microscopy (SEM)..... | 48 |
| 3.5.2. Reflection Measurement | 48 |
| 3.5.3. Quantum Efficiency Measurement | 50 |
| 3.5.4. Lifetime Measurement..... | 50 |
| 3.5.5. I-V Curve Measurement | 50 |
| 3.5.6. TLM Measurement | 51 |
| 3.6. Quokka 2 Analysis | 52 |
| 4. RESULTS AND DISCUSSIONS | 55 |
| 4.1. Laser Texturing | 55 |
| 4.1.1. Uniformity Across the Wafer | 56 |
| 4.1.2. Effects of Draw Step and Step Period | 57 |
| 4.1.3. Effects of Pattern and Laser Line Spacing..... | 62 |
| 4.1.4. Effects of Laser Pulse Frequency | 64 |
| 4.1.5. Effects of Laser Power..... | 66 |
| 4.1.6. Effects of Iteration | 68 |
| 4.2. Post-Texture Cleaning | 71 |
| 4.3. Effects of Anti Reflection Coating and Passivation Layer on implied Open Circuit Voltage and Reflection..... | 77 |
| 4.4. Solar Cell Performance | 82 |
| 4.5. Quokka 2 Analysis | 90 |

| | | |
|------------|---|-----|
| 5. | CONCLUSION AND FUTURE STUDY | 95 |
| 6. | PUBLISHED ARTICLES FROM THESIS WORK..... | 101 |
| | REFERENCES | 103 |
| APPENDICES | | |
| A. | SEM Images of Texturing Using NaOH Solution | 107 |
| B. | MATLAB Code for Reflection and Weighted Reflection Calculation..... | 109 |
| C. | Quokka 2 Analysis Code..... | 115 |
| D. | Uniformity Across Wafer..... | 119 |
| E. | Post-Texture Cleaning..... | 121 |
| F. | Effects of ARC and Passivation Layer..... | 123 |
| G. | SEM Images of Solar Cells | 125 |
| H. | Reflection Curves of Solar Cells..... | 127 |

LIST OF TABLES

TABLES

| | |
|--|----|
| Table 2.1. <i>Solar cell performance and optical results achieved by Ximello Quiebras</i> | 31 |
| Table 2.2. <i>Result of fabricated double-sided buried contact solar cell reported by Abbott and Cotter</i> | 34 |
| Table 2.3. <i>Comparison between solar cell parameter and weighted reflection reported by Zeilke et al.</i> | 37 |
| Table 2.4. <i>Solar cell performance and weighted reflection comparison reported by Dobrzanski et al.</i> | 40 |
| Table 4.1. <i>Laser parameters used for checking the uniformity across the wafer</i> | 56 |
| Table 4.2. <i>Common parameters for investigating the effects of draw step and step period</i> | 58 |
| Table 4.3. <i>Changing parameters and their resulting speed and overlap</i> | 58 |
| Table 4.4. <i>Common parameters for investigating the effects of draw step and step period</i> | 59 |
| Table 4.5. <i>Changing parameters and their resulting speed and overlap</i> | 60 |
| Table 4.6. <i>Common parameters of effects of draw step and step period</i> | 61 |
| Table 4.7. <i>Changing parameters of effects of draw step and step period</i> | 62 |
| Table 4.8. <i>Common laser parameters for determining the effect of pattern and laser line spacing</i> | 63 |
| Table 4.9. <i>Changing parameter of pattern and line spacing</i> | 63 |
| Table 4.10. <i>Common laser parameters for determining the effects of laser pulse frequency on surface morphology and reflection</i> | 65 |
| Table 4.11. <i>Frequency changes in determining the effects of laser pulse frequency on surface morphology and reflection</i> | 65 |
| Table 4.12. <i>Common laser parameters for determining the effect of laser power</i> ... | 67 |

| | |
|--|-----|
| Table 4.13. <i>Changing laser parameters for determining the effect of laser power...</i> | 67 |
| Table 4.14. <i>Common laser texturing parameters of effects of iteration</i> | 69 |
| Table 4.15. <i>Changing laser texturing parameters of effects of iteration.....</i> | 69 |
| Table 4.16. <i>Common laser texturing parameters for investigating post-texture cleaning.....</i> | 72 |
| Table 4.17. <i>Changing laser texturing parameters for investigating post-texture cleaning.....</i> | 72 |
| Table 4.18. <i>Laser parameters for determining effect of high concentration temperature KOH solution</i> | 74 |
| Table 4.19. <i>Post-texture cleaning parameter using KOH solution</i> | 74 |
| Table 4.20. <i>Common parameters for investigating effects of the passivation layer..</i> | 78 |
| Table 4.21. <i>Changing parameters for investigating effects of the passivation layer</i> | 78 |
| Table 4.22. <i>Laser texturing and post-texture cleaning parameters for investigating effect of ARC layer.....</i> | 80 |
| Table 4.23. <i>Common laser texturing parameters for solar cell fabrication</i> | 83 |
| Table 4.24. <i>Changing laser texturing and post-texture cleaning parameters for solar cell fabrication.....</i> | 83 |
| Table 4.25. <i>Parameters of sample simulated using Quokka 2</i> | 93 |
| Table 4.26. <i>Comparison between experimental data and simulation results.....</i> | 93 |
| Table E.1. <i>Common laser texturing parameters for investigating post-texture cleaning</i> | 121 |
| Table E.2. <i>Changing laser texturing parameters for investigating post-texture cleaning.....</i> | 121 |

LIST OF FIGURES

FIGURES

| | |
|---|----|
| <i>Figure 1.1.</i> (left) Glucose molecule as a basic form of energy for living species; (right) ATP molecule as a cell's energy currency; figures are illustrated using The Cambridge Crystallographic Data Centre (CCDC)-Mercury software. | 1 |
| <i>Figure 1.2.</i> Global energy consumption in 2017 and share of renewable energies and solar energy | 3 |
| <i>Figure 1.3.</i> Solar spectral irradiance | 4 |
| <i>Figure 1.4.</i> Absorption of sunlight at different wavelengths from different molecules | 4 |
| <i>Figure 1.5.</i> Air mass as a light's traveling distance to reach the surface..... | 5 |
| <i>Figure 1.6.</i> Material categories based on their electrical conductivity | 6 |
| <i>Figure 1.7.</i> Electronic transition from valence band to the conduction band by photon absorption..... | 7 |
| <i>Figure 1.8.</i> Doping process for silicon with (right) Boron and (left) Phosphorous..... | 8 |
| <i>Figure 1.9.</i> Schematic of metal work function which is the energy difference between metal Fermi level and vacuum level | 8 |
| <i>Figure 1.10.</i> Different Fermi level position in the doped semiconductor..... | 9 |
| <i>Figure 1.11.</i> (top) Band diagram aligns in a way that their vacuum levels are in the same level (bottom) Fermi level, valence band, and the conduction band of semiconductor bend in a way that Fermi level of semiconductor become at the same level of Fermi level of metal | 9 |
| <i>Figure 1.12.</i> Schematic of an ohmic contact for the metal-semiconductor junction. The n-type semiconductor has a higher work function than metal or p-type semiconductor has a lower work function than metal. | 10 |

Figure 1.13. Schematic of Schottky junction for metal- semiconductor. The n-type semiconductor has a lower work function than metal or p-type semiconductor has a higher work function than metal..... 10

Figure 1.14. (top) Diffusion of majority carrier (middle) recombination of a minority with majority in opposite region with increasing drift force (bottom) depletion region formation and remaining ions 11

Figure 1.15. In an n-type semiconductor, Fermi level is closer to the conduction band and in the p-type semiconductor, Fermi level is closer to the valence band 11

Figure 1.16. Band bending in a way that Fermi levels in two semiconductors align with each other..... 11

Figure 1.17. Working phenomena of solar cells 12

Figure 1.18. Electron-hole pair generation, separation due to ions electric field in the depletion region, traveling through an external circuit..... 13

Figure 1.19. Equivalent electrical circuit for a solar cell 13

Figure 1.20. I-V curve of a solar cell under illumination and dark condition..... 13

Figure 1.21. Illustration of R_s , R_{sh} , I_{sc} , V_{oc} , and maximum power and power point of a solar cell..... 15

Figure 1.22. EQE curve indicating number of generated carriers over number of incoming photons..... 16

Figure 1.23. Usable part of incident light versus bandgap of absorbing the material 17

Figure 1.24. National Renewable Energy Laboratory (NREL) - Best Research-cell Efficiencies chart at 17.08.2018 18

Figure 1.25. (right) Monocrystalline and (left) multi-crystalline silicon solar cell... 19

Figure 1.26. Schematic of (left) Amorphous silicon solar cell, (middle) CdTe solar cell, and (right) CIGS solar cell 19

Figure 1.27. Schematic of (left) Dye-Sensitized Solar Cells (DSSC), (middle) Organic Solar Cells, and (right) Perovskite Solar Cells 20

Figure 1.28. Market share of different types of solar cell in 2017 20

Figure 1.29. Schematic process flow of solar cell fabrication 21

| | |
|---|----|
| <i>Figure 1.30.</i> Schematic of (left) Czochralski growth system and (right) Float zone growth system | 22 |
| <i>Figure 1.31.</i> Diamond coated wire silicon slicing system | 22 |
| <i>Figure 1.32.</i> (right) Reflection of incident light from the flat surface (left) reflection of incident light from the textured surface which increases the absorption..... | 23 |
| <i>Figure 1.33.</i> Pyramids with the angle of 54.7° as a result of chemical texturing using KOH solution | 23 |
| <i>Figure 1.34.</i> Penetration depth of doping for two steps of pre-deposition and drive-in | 24 |
| <i>Figure 1.35.</i> Chamber of the solid-state diffusion furnace..... | 24 |
| <i>Figure 1.36.</i> Refractive Index of Blue: Silicon, Red: Optimum Material, Green: Si_3N_4 | 25 |
| <i>Figure 1.37.</i> Schematic of PECVD Chamber | 26 |
| <i>Figure 1.38.</i> Steps of the screen-printing technique..... | 26 |
| <i>Figure 1.39.</i> Front Surface of the solar cell with (left) three busbars, (middle) four busbars; (right) back surface of a solar cell | 26 |
| <i>Figure 2.1.</i> Becquerel's discovery of photovoltaic effect..... | 29 |
| <i>Figure 2.2.</i> SEM of achieved morphology using TMAH reported by Papet et al. | 30 |
| <i>Figure 2.3.</i> SEM images of KOH-IPA (left) and KOH -PVA (right) reported by Ximello Quiebras | 31 |
| <i>Figure 2.4.</i> SEM image of a textured multi-crystalline Silicon sample reported by Es et al..... | 32 |
| <i>Figure 2.5.</i> Reflection curves of (left) high concentration NaOH and (right) low concentration NaOH reported by Hylton et al. | 32 |
| <i>Figure 2.6.</i> Reflection curves of samples (left) without ARC and (right) with ARC reported by Macdonald et al..... | 33 |
| <i>Figure 2.7.</i> SEM images of (top right) acidic texturing (top left) alkaline texturing (bottom right) masked RIE (bottom left) mask-less RIE reported by Macdonald et al. | 33 |

| | |
|--|----|
| <i>Figure 2.8.</i> SEM images (left) as-textured, (middle) anisotropic post-texture cleaned, and (right) isotropic post-texture cleaned reported by Abbott and Cotter..... | 34 |
| <i>Figure 2.9.</i> SEM images (left) as-textured, (middle) post-texture cleaned, and (right) after metallization reported by Nayak et al..... | 35 |
| <i>Figure 2.10.</i> I-V curve of a sample reported by Nayak et al. | 35 |
| <i>Figure 2.11.</i> SEM images of (top left) as-textured and post-texture cleaned using NaOH with durations of (top right) 5sec (bottom left) 10sec (bottom right) 20 sec reported by Nayak et al..... | 36 |
| <i>Figure 2.12.</i> SEM image of the final structure reported by Zeilke et al..... | 37 |
| <i>Figure 2.13.</i> SEM images of textured samples with femtosecond laser in (left) air and (right) DI water mediums reported by Parmar and Shin | 38 |
| <i>Figure 2.14.</i> Reflection curves of samples textured with femtosecond laser in air and DI water mediums reported by Parmar and Shin | 38 |
| <i>Figure 2.15.</i> SEM images of (left) as-textured and post-texture cleaned for (middle) 10min and (right) 20min for line groove pattern reported by Dobrzanski et al. | 39 |
| <i>Figure 2.16.</i> SEM images of (left) as-textured and post-texture cleaned for (middle) 10min and (right) 20min for criss-cross pattern reported by Dobrzanski et al..... | 39 |
| <i>Figure 2.17.</i> Reflection curves of (left) line grooves and (right) criss-cross pattern reported by Dobrzanski et al..... | 39 |
| <i>Figure 3.1.</i> Effect of texturing on the surface | 41 |
| <i>Figure 3.2.</i> Laser equipment. Stage, N2 Gas, protective Glass, Optical Lens | 42 |
| <i>Figure 3.3.</i> Interface of laser setup software showing Drawing, Magnification, and Alignment sections (left), Laser and scanner parameters (right)..... | 43 |
| <i>Figure 3.4.</i> Geometry options of (left) elliptic arc (right) square..... | 44 |
| <i>Figure 3.5.</i> Schematic of solar cell fabrication process in which blue blocks are fabrication steps and yellow blocks are characterization steps | 45 |
| <i>Figure 3.6.</i> Picture of Semco Qtherm PECVD / solid state diffusion system..... | 46 |
| <i>Figure 3.7.</i> Picture of EKRA screen printing system..... | 46 |
| <i>Figure 3.8.</i> Picture of BTU International firing system | 47 |
| <i>Figure 3.9.</i> MATLAB GUI for reflection/transmission/EQE/IQE calculation..... | 48 |

| | |
|---|----|
| <i>Figure 3.10.</i> First reflection/transmission/EQE measurement setup | 49 |
| <i>Figure 3.11.</i> Bentham PVE300 Photovoltaic EQE (IPCE) and IQE | 49 |
| <i>Figure 3.12.</i> QuickSun 120CA-XL for measuring I-V curve (left) and corresponding software (right)..... | 51 |
| <i>Figure 3.13.</i> Schematic of TLM measurement resistance | 51 |
| <i>Figure 3.14.</i> Resulting graph from TLM measurement..... | 52 |
| <i>Figure 3.15.</i> Figure of Quokka 2 simulation software..... | 53 |
| <i>Figure 3.16.</i> Input parameters of OPAL 2 simulation tool | 53 |
| <i>Figure 3.17.</i> Output of OPAL 2 simulation tool..... | 54 |
| <i>Figure 4.1.</i> Overlap between laser spots..... | 55 |
| <i>Figure 4.2.</i> Different achievable morphologies depending on overlap | 56 |
| <i>Figure 4.3.</i> Optical and SEM images of a wafer divided into 64 samples and textured with laser parameters Set 1 | 57 |
| <i>Figure 4.4.</i> Optical and SEM images of the textured wafer with laser parameters of Set 2..... | 57 |
| <i>Figure 4.5.</i> Optical image of textured wafer for investigating the effects of draw step and step period | 59 |
| <i>Figure 4.6.</i> Optical image of textured sample for investigating the effects of draw step and step period | 60 |
| <i>Figure 4.7.</i> SEM images of textured wafer to investigate the effects of draw step and step period CP2 | 60 |
| <i>Figure 4.8.</i> Reflection curves of all sets with CP2 | 61 |
| <i>Figure 4.9.</i> SEM images of Set 1 and Set 2..... | 62 |
| <i>Figure 4.10.</i> Reflection curves of Set 1 and Set 2 | 62 |
| <i>Figure 4.11.</i> Top view SEM images from textured samples with line pattern and CP1 | 64 |
| <i>Figure 4.12.</i> Top view and cross-section view SEM images from textured samples with criss-cross pattern and CP2 | 64 |
| <i>Figure 4.13.</i> SEM images of effects of the laser pulse frequency of CP1 | 65 |
| <i>Figure 4.14.</i> Reflection curves of effects of the laser pulse frequency of CP1 | 66 |

| | |
|---|----|
| <i>Figure 4.15.</i> SEM images of effects of the laser pulse frequency of CP2 | 66 |
| <i>Figure 4.16.</i> Top view and cross-section view SEM images from textured samples with CP1 | 67 |
| <i>Figure 4.17.</i> Top view and cross-section view SEM images from textured samples with CP2 | 68 |
| <i>Figure 4.18.</i> Top view and cross-section view SEM images from textured samples with CP3 | 68 |
| <i>Figure 4.19.</i> Optical image of sets of CP1 and CP2..... | 70 |
| <i>Figure 4.20.</i> SEM images of sets of CP1 | 70 |
| <i>Figure 4.21.</i> SEM images of sets of CP2 | 70 |
| <i>Figure 4.22.</i> Weighted reflection of sets of CP1 and CP2 | 70 |
| <i>Figure 4.23.</i> Top view SEM images of sets of CP3 | 71 |
| <i>Figure 4.24.</i> Cross section view SEM images of sets of CP3 | 71 |
| <i>Figure 4.25.</i> SEM images of CP1..... | 72 |
| <i>Figure 4.26.</i> SEM images of CP2..... | 73 |
| <i>Figure 4.27.</i> Weighted reflection of CP1 and CP2..... | 73 |
| <i>Figure 4.28.</i> Top view SEM images of samples with different concentration and duration at 60°C..... | 74 |
| <i>Figure 4.29.</i> Top view SEM images of samples with different post-texture cleaning concentration and duration at 80°C | 75 |
| <i>Figure 4.30.</i> 45° tilted view SEM images of samples with different post-texture cleaning concentration and duration at 60°C..... | 75 |
| <i>Figure 4.31.</i> 45° tilted view SEM images of samples with different post-texture cleaning concentration and duration at 80°C..... | 76 |
| <i>Figure 4.32.</i> Weighted reflection of the sample with different post-texture cleaning concentrations and durations at (left) 80°C and (right) 60°C | 76 |
| <i>Figure 4.33.</i> Reflection curves of the sample with relatively low weighted reflection at (left) 80°C and (right) 60°C..... | 77 |
| <i>Figure 4.34.</i> SEM images of Set 1, prepared for depositing the passivation layer ... | 79 |
| <i>Figure 4.35.</i> SEM images of Set 2, prepared for depositing the passivation layer ... | 79 |

| | |
|--|----|
| <i>Figure 4.36.</i> Implied Voc (left) and weighted reflection (right) of samples with the passivation layer..... | 80 |
| <i>Figure 4.37.</i> Optical image of samples with different ARC thicknesses..... | 81 |
| <i>Figure 4.38.</i> Weighted reflection of all samples (left) and reflection curve of Set 2 with 2min KOH solution..... | 81 |
| <i>Figure 4.39.</i> Optical image of the final solar cell indicating the size of samples and their placement regarding the wafer..... | 82 |
| <i>Figure 4.40.</i> Optical image of all samples | 83 |
| <i>Figure 4.41.</i> Top view SEM images of all samples | 84 |
| <i>Figure 4.42.</i> Saw damage etched sample (left), Un-textured reference (middle), and laser textured sample (right)..... | 85 |
| <i>Figure 4.43.</i> Weighted reflection of samples (left) without and (right) with ARC layer | 85 |
| <i>Figure 4.44.</i> Top view SEM images of fingers on all samples..... | 86 |
| <i>Figure 4.45.</i> 45° tilted view SEM images of fingers on all samples | 86 |
| <i>Figure 4.46.</i> Cross section view SEM images of fingers on all samples..... | 86 |
| <i>Figure 4.47.</i> Efficiency (left) and fill factor (right) of fabricated solar cells..... | 87 |
| <i>Figure 4.48.</i> Jsc (left) and Voc (right) of fabricated solar cells..... | 88 |
| <i>Figure 4.49.</i> Contact resistance of fabricated solar cells | 88 |
| <i>Figure 4.50.</i> EQE of the fabricated solar cells post-textured for (left) 2min and (right) 4min | 89 |
| <i>Figure 4.51.</i> IQE of the fabricated solar cells post-textured for (left) 2min and (right) 4min | 89 |
| <i>Figure 4.52.</i> (left) I-V curves and (right) IQE and reflection curves of the best fabricated solar cell and reference solar cell | 90 |
| <i>Figure 4.53.</i> Defined geometry for Quokka 2 analysis with (left) two fingers and (right) one finger | 90 |
| <i>Figure 4.54.</i> Input parameters for OPAL 2 analysis | 91 |
| <i>Figure 4.55.</i> Surface morphology used for OPAL 2 analysis (left) the planar fraction and (right) the characteristics angle | 91 |

Figure 4.56. Reflection curve and IQE of the sample in thick lines and reflection, transmission, and absorption of the fitted curve in thin lines. 92

Figure 4.57. RMSE error of fitting OPAL 2 92

Figure 4.58. I-V curve of the simulated solar cell..... 93

LIST OF ABBREVIATIONS

ABBREVIATIONS

| | |
|----------|---|
| ALD | Atomic Layer Deposition |
| ARC | Anti Reflection Coating |
| ATP | Adenosine Triphosphate |
| BSF | Back Surface Field |
| c-Si | Crystalline Silicon |
| CIGS | Copper Indium Gallium Selenide |
| CVD | Chemical Vapor Deposition |
| DI Water | Deionized Water |
| DR | Detector Responsivity |
| DSSC | Dye-Sensitized Solar Cells |
| EDP | Ethylenediamine Pyrocatechol |
| EHT | Electron High Tension |
| EQE | External Quantum Efficiency |
| F.F. | Fill Factor |
| IPA | Isopropyl Alcohol |
| IQE | Internal Quantum Efficiency |
| PECVD | Plasma Enhanced Chemical Vapor Deposition |
| PVA | Polyvinyl Alcohol |
| QSS | Quasi-Steady-State Lifetime |

| | |
|------|--------------------------------|
| RIE | Reactive Ion Etching |
| TLM | Transmission Line Measurement |
| TMAH | Tetramethyl Ammonium Hydroxide |
| UI | User Interface |

LIST OF SYMBOLS

SYMBOLS

| | |
|--------------------------------|---|
| α | Absorption Coefficient |
| Ag | Silver |
| Al | Aluminum |
| Al ₂ O ₃ | Alumina |
| c | Speed of Light in Vacuum ($3 \times 10^8 \text{ m.s}^{-1}$) |
| CH ₄ | Methane |
| CO ₂ | Carbon Dioxide |
| h | Planck Constant ($6.626 \times 10^{-34} \text{ J.s}$) |
| H ₂ O | Water |
| H ₂ O ₂ | Hydrogen Peroxide |
| HCl | Hydrochloric Acid |
| HNA | HF/Nitric/Acetic Acid |
| I ₀ | Reverse Saturation Current |
| I _d | Diode Current |
| I _{ph} | Photogenerated Current |
| I _{sc} | Short Circuit Current |
| iV _{oc} | impliedVoc |
| J _{sc} | Short Circuit Current Density |
| k | Extinction Coefficient |

| | |
|------------|---|
| k_B | Boltzmann Constant |
| N_2 | Nitrogen |
| NH_4 | Ammonia |
| NH_4OH | Ammonium Hydroxide |
| O_2 | Oxygen |
| O_3 | Ozone |
| q | Electronic Charge Constant (1.6×10^{-19} C) |
| R_m | Metal Resistance |
| R_{m-sc} | Metal-Semiconductor Resistance |
| R_s | Series Resistance |
| R_{sc} | Semiconductor Resistance |
| R_{sh} | Shunt Resistance |
| Si | Silicon |
| Si_3N_4 | Silicon Nitride |
| SiH_4 | Silane |
| T | Temperature in Kelvin |
| V_{oc} | Open Circuit Voltage |
| V_T | Thermal Voltage |

CHAPTER 1

INTRODUCTION

1.1. Importance of Energy

Every living organism requires energy to live. For all species on the earth, almost every sources of energy are directly or indirectly related to solar energy. Plants with green leaves use a specific process to directly produce energy from sunlight which it is called photosynthesis. These plants consume Carbon Dioxide (CO₂) from the air with leaves and water (H₂O) from the ground with roots to generate Oxygen (O₂) and Glucose (Figure 1.1 (left)) which is the source of energy inside cells. One of the reactants is Chlorophyll molecules which are a type of the many green pigments of green leaves. The equation leading to energy generation is mentioned in Eq. 1.1. Later, plants can convert Glucose to Adenosine Triphosphate (ATP) which is a cell's energy currency. This molecule is shown in Figure 1.1 (right). This discovery awarded Chemistry Nobel Prize in 1997 to Prof. Paul D. Boyer (University of California, USA) and Dr. John E. Walker (Cambridge, United Kingdom) for their elucidation of the enzymatic mechanism underlying the synthesis of Adenosine Triphosphate and with one half to Prof. Jens C. Skou (Aarhus University, Denmark) for the first discovery of an ion-transporting enzyme, Na⁺, K⁺-ATPase [1].

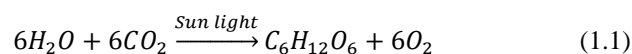


Figure 1.1. (left) Glucose molecule as a basic form of energy for living species; (right) ATP molecule as a cell's energy currency; figures are illustrated using The Cambridge Crystallographic Data Centre (CCDC)-Mercury software.

On the other hands, living species other than plants cannot convert solar energy into the consumable type of energy. Thus, some animals consume plants to be able to gain energy and some other eat other animals which consumed plants. In the animal's body, every cell needs the energy to operate. The body extracts energy from Hydrocarbons and burning them with O_2 which produce energy and CO_2 . This process also applies to the human's body. Human's body, like other species, needs the energy to perform any activity from breathing to running or even thinking. Human's body also gets the energy from the food which s/he eats. The main source of energy for all species to keep them alive and active is sun which they can get energy directly or indirectly.

Moreover, a human being requires energy not only for its own body but also for all other works it does. Humans are masters of tools. Through history, humans made many different types of tools to make works easier for them. They built spear to help them catch animals or sickle to help them gather plants. At the beginning stages, the energy required for making tools was low. However, with the current expansion of manufacturing, required energy for making tools is enormous. Also, energy is not only used for making tools, it's also used for many purposes like heating, cooling, lighting, and others. For decades, the main source of energy for different purposes was coal from 4000 years ago [2]. Coal got more attention after the industrial revolution in 18th [3]. Later, Oil, as another source of energy, was discovered more than 2000 years ago [4]. These traditional energy sources were the main sources of energy for many years and they played a significant role in the industrial revolution. These energy sources have three main drawbacks. One of the most important disadvantages of traditional sources of energy is that they pollute the environment. Another drawback is that they produce CO_2 which is one of the greenhouse gases. The greenhouse effect is a process which several gases in the atmosphere absorbs reflected solar radiation from the earth and re-emits energy toward the earth in the infrared region. This effect causes global warming which affects the earth's environment. The greenhouse gases are water vapor, CO_2 , Methane (CH_4), Ozone (O_3). Another drawback of traditional energy sources is that they are limited. The estimations indicate that maximum of extraction

of oil (peak oil) will occur in 2020 [5] and maximum production of coal (peak coal) will occur in 2030 [6]. After these years, oil and coal production decrease is unavoidable. Thus, the depleting time for oil and coal is not far.

Hence, humans have to find new sources of energy which have less environmental damages and also, can be used for a longer time. Renewable energy sources also known as green energies which are replenishable by nature. These energies consist of solar energy, wind energy, geothermal heat, and hydroelectric power. Among these solar energy offers a clean, infinite, and cheap alternative to all others. It has the potential to cover all energy needs of human being. The direct conversion of solar energy to electricity can be done using photovoltaic devices also known as Solar Cells.

In 2017, around 10.4% of global energy consumption belongs to renewable energy in which 7.1% of them is due to photovoltaic technology. Figure 1.2 shows the global energy production at the end of 2017 from the total generated power of 415 GW [9] [10] which is still developing [12].

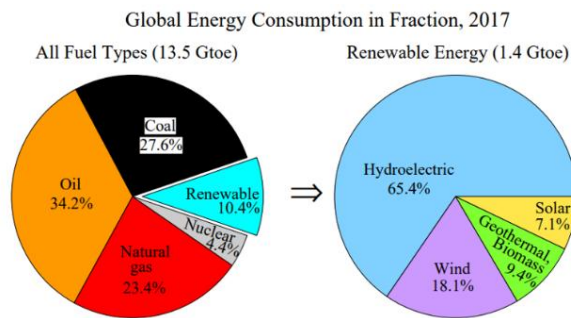


Figure 1.2. Global energy consumption in 2017 and share of renewable energies and solar energy

1.2. Properties of Solar Energy

The sun is at a distance of 1.496×10^8 kilometers from the earth which receives 1368 W/m² at the outer space while the total energy released from the sun is 3.846×10^{26} J per second. The solar energy is radiated in the form of an electromagnetic wave which is usually defined by the wavelength. The power density of each wavelength per surface area is called spectral irradiance. The spectral irradiance formula is shown in Eq. 1.2 and sun's spectral irradiance is shown in Figure 1.3.

$$F(\lambda) = \phi q \frac{1.24}{\lambda(\mu\text{m})} \frac{1}{\Delta\lambda(\mu\text{m})} \quad (1.2)$$

In the equation, $F(\lambda)$ is the spectral irradiance in $\text{Wm}^{-2}\mu\text{m}^{-1}$, Φ is the photon flux which is a number of photons per unit area per time [$\text{m}^{-2}\text{sec}^{-1}$], λ is the wavelength of the photon in μm , and q is electronic charge constant of 1.6×10^{-19} C.

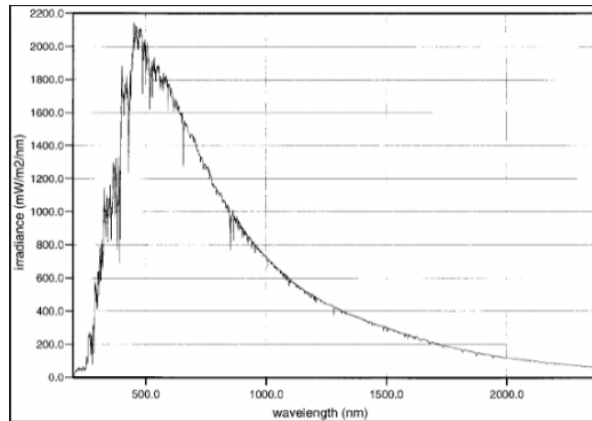


Figure 1.3. Solar spectral irradiance

This spectral irradiance is measured for the outer space of earth. When the sunlight enters the atmosphere, molecules can absorb, scatter, or reflect the incoming photons. Different molecules interact with photons at a specific wavelength. Figure 1.4 shows the interactions of different molecules with sunlight at different wavelengths. For instance, Ozon molecules absorb light in ultraviolet and visible region and water and Carbon Dioxide molecules absorb light in red and infrared regions.

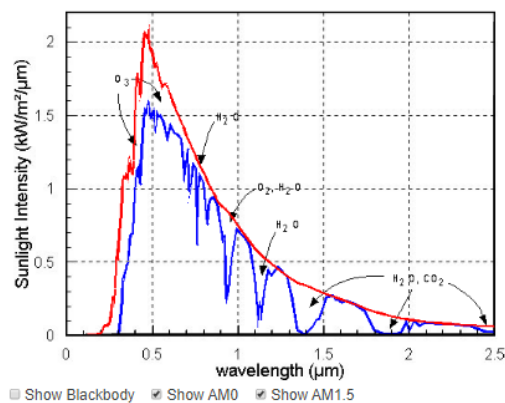


Figure 1.4. Absorption of sunlight at different wavelengths from different molecules

Another parameter which affects the intensity of sunlight at the earth's surface is air mass. Air mass is a distance that light travels to reach the surface, can be quantified based on the angle between sun direction and the perpendicular line at earth. This angle (θ) is called Zenith angle. When sunlight is perpendicular to the earth, the air mass is 1 and when the angle of sunlight from the vertical line is 48.2° , the air mass is 1.5. The air mass illustrated in Figure 1.5 and its formula is denoted in Eq. 1.3.

$$AM = \frac{1}{\cos \theta} \quad (1.3)$$

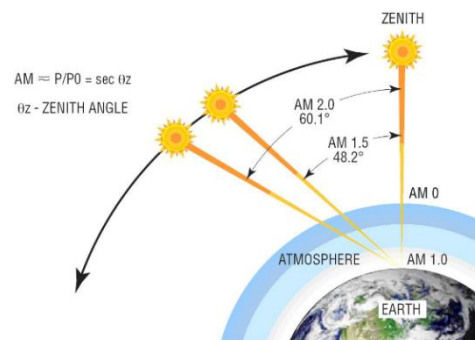


Figure 1.5. Air mass as a light's traveling distance to reach the surface

Based on the given information, the solar energy on the earth's surface with air mass of 1.5 is about 1000.4 W/m^2 which is considered as 1 SUN in the measurement's standards. This standard is named as AM1.5 condition.

1.3. Physics of Photovoltaic Devices

In this section, information about different types of materials and their specific properties are explained. In addition, detailed information about valance and conduction band, Fermi level, and band bending are given.

1.3.1. Materials

It is possible to categorize materials in different ways. Here, materials are categorized based on their electrical conductivity. Electrical and as well as optical properties of materials are a strong function of the forbidden energy gap origination from the discrete nature of atomic energy states. Figure 1.6 shows a schematics of material classification and its dependence on the energy band gap of the materials.

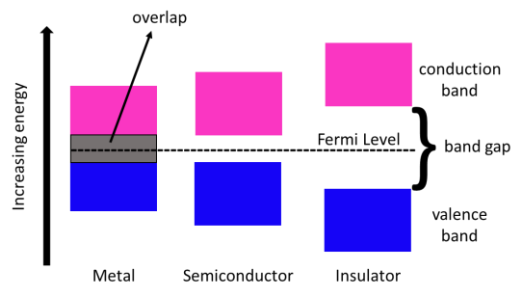


Figure 1.6. Material categories based on their electrical conductivity

A short description of these types of materials is given in the following sections.

1.3.1.1. Metals

Metals are the type of materials having almost free electrons giving rise to high conductivity in the range of 10^{-4} to $10^{-6} \Omega\text{cm}$. This is due to fact that valence band and conduction band are overlapping so that electrons from the valence band can easily participate in the conduction band very easily.

1.3.1.2. Semiconductors

Semiconductors are another type of materials that have a relatively small band gap between valence band and conduction band, so that under certain conditions (high temperature or light illumination) electrons can be excited to the conduction band and participate in the conduction process. For instance, silicon, the most widely used semiconductor, has band gap energy of 1.12 eV which is sufficiently low for electron excitation and sufficiently high for carrier lifetime. For this reason, Si has become the most important semiconductor in the microelectronic and optoelectronic applications.

In optoelectronic applications such as solar cells, electrons in the valence band can absorb a photon with energy higher than the bandgap and make the electrical transition to the conduction band. The empty positions of electrons in the valence band are called holes which are also considered as electrical charge carriers that can move through the valence band. The electron transition and remaining hole are schematically shown in Figure 1.7. Presence of a band gap makes also sure that electrons residing in the conduction band spend some time (life time) there before a recombination takes place.

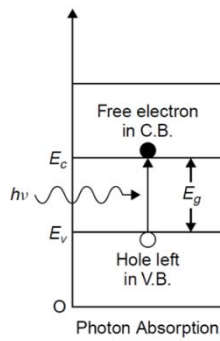


Figure 1.7. Electronic transition from valence band to the conduction band by photon absorption

1.3.1.3. Insulators

Insulators are the type of materials in which their bandgap is so high that the energy required for electron transition from valence band to conduction band is too high and electrons cannot be provided to the conduction process easily. These materials are not electrically conductive at normal situations, but they become conductive if severe situation applies to them like applying a high voltage.

1.3.2. Doping

It is possible to increase the conductivity of semiconductors by doping. The undoped semiconductors are called intrinsic. The doping process is basically adding specific impurity materials to the semiconductor by substituting original semiconductor's atoms which introduce extra charge carrier. In this way, the number of free carriers in the conduction band and valence band can be controlled. For instance, as illustrated in Figure 1.10, when a Phosphorous atom with 5 valence electrons is added to Si crystal 4 of these electrons are used to make covalent bonds with Si atoms, while the fifth one is almost free in the crystal lattice. This free electron which is residing in the conduction band increases the conduction. Similarly, when a Boron atom with 3 valence electrons are added to Si, one of the bonds is not occupied, which creates a free hole in the valence band. The doped semiconductor which has extra electrons is called n-type and a doped semiconductor which has fewer electrons is called p-type material. The amount of increase in conductivity depends on the level of doping. Figure 1.8 shows the doping process for silicon with Boron (a) and Phosphorous (b).

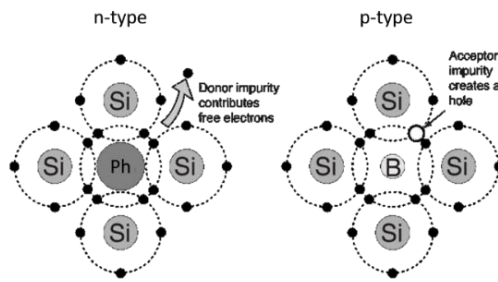


Figure 1.8. Doping process for silicon with (right) Boron and (left) Phosphorous

1.3.3. Junctions

When two different materials attach to each other, their electronic structure at the junction region undergoes a transition leading to formation of a discontinuity in the potential profile. Any discontinuity in the potential energy profile has a corresponding electric field which plays a crucial role in the device operation. In these following sections, a short description of different junctions is given.

1.3.3.1. Metal-Semiconductor (Ohmic / Schottky Junction)

As mentioned in 1.3.1.1, metals do not have bandgap so when they attach to semiconductors, their work function aligns with semiconductor's Fermi level. The work function is the required thermodynamic energy to remove an electron from a metal to the vacuum level. The schematic of this energy is shown in Figure 1.9. For an intrinsic semiconductor, the Fermi level is in the middle of the bandgap. It is closer to the conduction band for an n-type material and to valence band for a p-type material. The different Fermi level positions in the semiconductor are shown in Figure 1.10

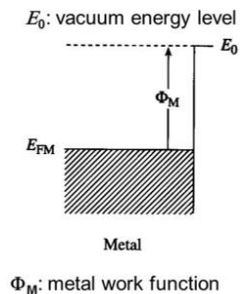


Figure 1.9. Schematic of metal work function which is the energy difference between metal Fermi level and vacuum level

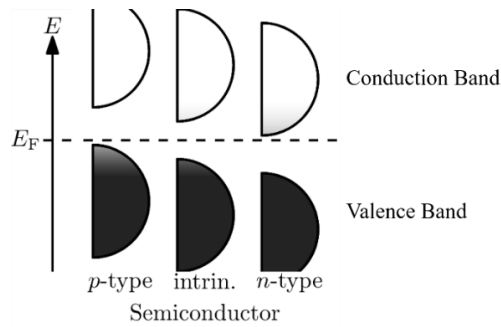


Figure 1.10. Different Fermi level position in the doped semiconductor

When a metal is attached to the semiconductor, the Fermi level of semiconductor and metal should be aligned at equilibrium when there is no particle transport between two sides of the junction. In order to meet this fundamental requirement of the thermodynamics, the valence and conduction band should bend as shown Figure 1.11.

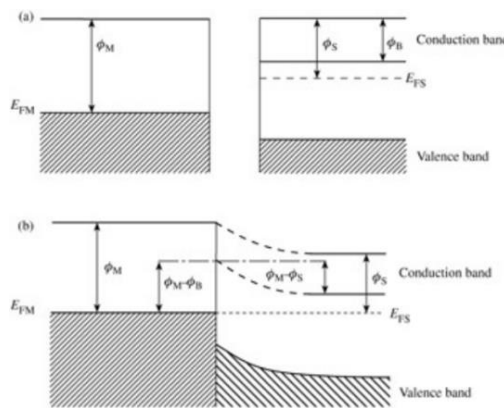


Figure 1.11. (top) Band diagram aligns in a way that their vacuum levels are in the same level (bottom) Fermi level, valence band, and the conduction band of semiconductor bend in a way that Fermi level of semiconductor become at the same level of Fermi level of metal

Based on the doping type of semiconductor and the difference between the work functions of metal and semiconductor, the junction can be either ohmic or Schottky. Ohmic contact, Figure 1.12, happens when n-type semiconductor has a higher work function than metal or p-type semiconductor has a lower work function than metal. In contrast, Schottky contact, Figure 1.13, happens when n-type semiconductor has a lower work function than metal or p-type semiconductor has a higher work function than metal. In the Schottky contact, there are barriers called Schottky barrier either for electrons in n-type semiconductor or holes in the p-type semiconductor at the junction.

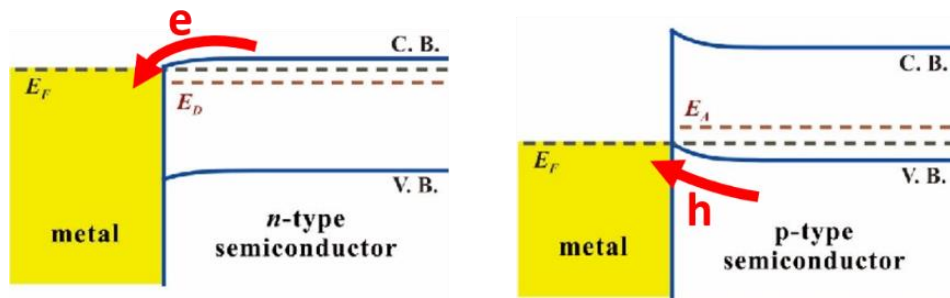


Figure 1.12. Schematic of an ohmic contact for the metal-semiconductor junction. The n-type semiconductor has a higher work function than metal or p-type semiconductor has a lower work function than metal.

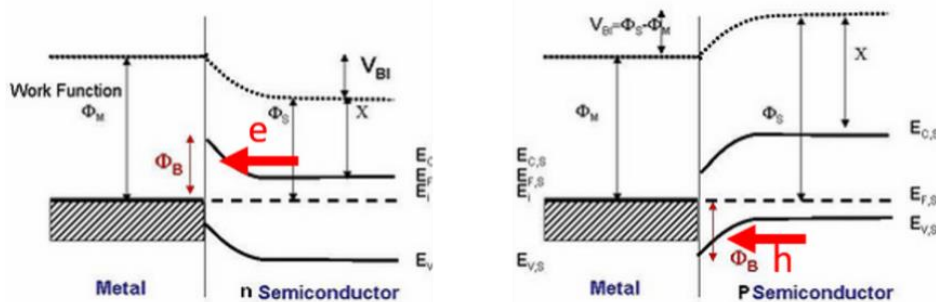


Figure 1.13. Schematic of Schottky junction for metal-semiconductor. The n-type semiconductor has a lower work function than metal or p-type semiconductor has a higher work function than metal.

1.3.3.2. P-N Junction

When two semiconductors with two different types of doping attach to each other, some electrons from n-type region diffuses to p-type region and recombine with some of the majority carriers in p-type which are holes as shown in Figure 1.14 (top). Also, some holes from p-type move to n-type region and recombine with majority carriers in n-type which are electrons. As these minority carriers recombine the majority carriers at the interface, a transition region called depletion region with not free charge carriers is created. When the free carriers are removed by recombination, fixed dopant atoms become ionized and create a dipole system at the interface. A corresponding electric field giving rise to the drift force and a drift electric current is then developed as shown in Figure 1.14 (middle). At a certain point, drift and diffusion become equal and this prevents further carrier transportation through depletion region under zero bias condition as shown in Figure 1.14 (bottom).

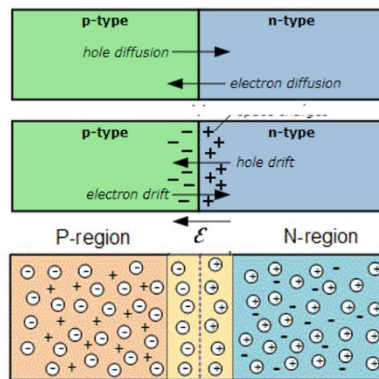


Figure 1.14. (top) Diffusion of majority carrier (middle) recombination of a minority with majority in opposite region with increasing drift force (bottom) depletion region formation and remaining ions

Like in the metal semiconductor junction described above, electron and hole transfer and formation of the dipole system leads to band bending at the interface of two regions. In n-type semiconductor, Fermi level is closer to the conduction band and in p-type semiconductor, Fermi level is closer to valence band as shown in Figure 1.15.

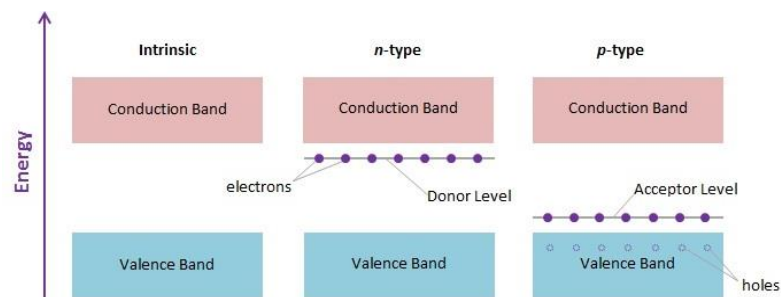


Figure 1.15. In an n-type semiconductor, Fermi level is closer to the conduction band and in the p-type semiconductor, Fermi level is closer to the valence band

In the band bending, conduction band and valence band bend in a way that Fermi level in two sides of semiconductor aligns with each other which is shown in Figure 1.16.

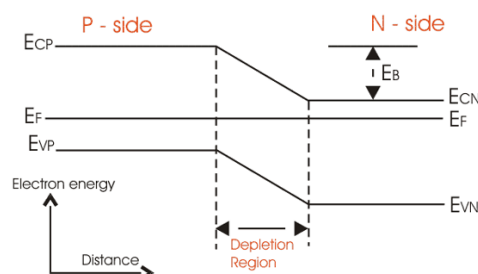


Figure 1.16. Band bending in a way that Fermi levels in two semiconductors align with each other

1.4. Solar Cells

Solar cells are photovoltaic devices which are mostly fabricated from semiconductors. In the solar cells, solar radiation provides photons with enough energy to the electrons for a transition from the valence band to the conduction band, thus electrons can travel through the solar cell and external circuit as shown in Figure 1.17. In this section, the working principals of a solar cell and different types of solar cells are introduced.

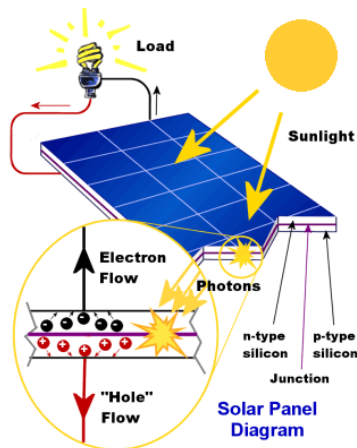


Figure 1.17. Working phenomena of solar cells

1.4.1. Solar Cell Working Principles

Conventional solar cells are made from two parts with two different doping types. These parts can be made from either same material which is called homojunction solar cell or two different materials which are called heterojunction solar cell. The working principles are almost the same for both cases. When incident sunlight hits the solar cell, photons penetrate inside the solar cell. The photons with energy higher than the bandgap of material are absorbed by electrons making electronic transitions which create electrons-hole pairs. The importance of using two different doping types is to separate electron-hole pair before they recombine with each other. Because of the electric field generated by ions in the depletion region at the interface, electrons or holes move toward the region where they are the majority. The holes generated in n-type region move toward p-type region and electrons generated in p-type move toward n-type region. Since minority carriers are separated from the remaining majority

carriers, they have a small chance for the recombination, so they can travel through an external circuit and generate an electrical current as shown in Figure 1.18.

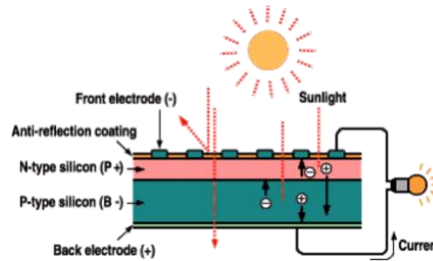


Figure 1.18. Electron-hole pair generation, separation due to ions electric field in the depletion region, traveling through an external circuit

In order to analyze the solar cell's output voltage and current, the equivalent electrical circuit shown in Figure 1.19 is used. In this figure, I_{ph} is photogenerated current from absorbed photons, I_d is diode current which comes from pn junction, R_s is series resistance and R_{sh} is shunt resistance.

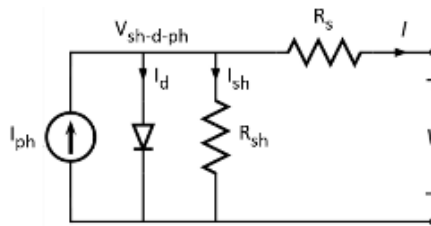


Figure 1.19. Equivalent electrical circuit for a solar cell

The I-V curve of solar cell in dark is basically that of a diode used in microelectronics. The I_d represents diode current and shown in Eq. 1.5. The I-V curves of the solar cell under illumination and in the dark case are shown in Figure 1.20.

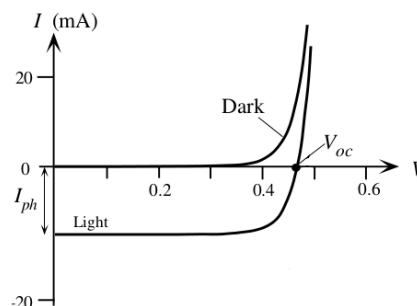


Figure 1.20. I-V curve of a solar cell under illumination and dark condition

In order to calculate I-V relation under illumination, following parameters are used: T is temperature in Kelvin, k_B is Boltzmann constant, q is electronic charge constant, V_T is thermal voltage, and I_0 is reverse saturation current. In addition, ideality factor, n, is a measure of the quality of the diode. In the ideal case (n=1), recombination is limited by minority carriers. Non-ideal diode has n>1 in which other recombination methods are also present. So, the total current in a solar cell can be written as

$$I = I_{ph} - I_d - I_{sh} \quad (1.4)$$

Where I_{ph} is the photogenerated current and I_d (the dark current of the diode) is

$$I_d = I_0 \left(\exp \left[\frac{V_{sh-d-ph}}{nV_T} \right] - 1 \right) \quad (1.5)$$

Where $V_{sh-d-ph}$ is the voltage drop across the diode and given by

$$V_{sh-d-ph} = V + IR_s \quad (1.6)$$

Where V_T as thermal voltage is

$$V_T = \frac{k_B T}{q} \quad (1.7)$$

$$I_{sh} = \frac{V_{sh-d-ph}}{R_{sh}} \quad (1.8)$$

I_{sh} represents the shunt current. Finally, the terminal current is found as

$$I = I_{ph} - I_0 \left(\exp \left[\frac{V - IR_s}{nV_T} \right] - 1 \right) - \frac{V + IR_s}{R_{sh}} \quad (1.9)$$

The ideal case for working solar cell is the case that R_s is zero, R_{sh} is high enough to neglect and ideality factor is one. In this case, Eq. 1.9 can be rewritten as

$$I = I_{ph} - I_0 \left(\exp \left[\frac{V}{V_T} \right] - 1 \right) \quad (1.10)$$

When the current is zero, open circuit voltage (V_{oc}) can be calculated and when a voltage is zero, short circuit current (I_{sc}) can be calculated as Eq. 1.11 and Eq. 1.12.

$$V_{oc} = V_T \ln \left(\frac{I_{ph}}{I_0} + 1 \right) \quad (1.11)$$

$$I_{sc} = I_{ph} \quad (1.12)$$

The ideal I-V curve approaches a rectangle as shown in Figure 1.21. In this case, the maximum power is $P_{max}=I_{sc} \times V_{oc}$. However, due to effect R_s and R_{sh} , actual I-V curve deviates from the rectangular shape. The maximum possible power is called maximum power point is calculated from the relationship $P_{mpp}=I_{mpp} \times V_{mpp}$. The effect of R_{sh} is mostly seen because of the defects at the junction interface. Increasing recombination leads to low R_{sh} which decrease open circuit voltage and thus, maximum power point. The increase in the contact resistance like metal contact and silicon or resistance of top and rear metal contacts leads to increase of R_s which decreases fill factor and I_{sc} and thus, maximum power point. The ratio of actual maximum power point to ideal maximum power is called fill factor (Eq. 1.13) which corresponds to the ratio of the area of two rectangles shown in Figure 1.21.

$$F.F. = \frac{P_{mpp}}{P_{max}} = \frac{I_{mpp} \times V_{mpp}}{I_{sc} \times V_{oc}} \quad (1.13)$$

The R_s and R_{sh} formulas are introduced in Eq. 1.14 and Eq. 1.15. Figure 1.21 shows the R_s , R_{sh} , I_{sc} , V_{oc} , maximum power, maximum power point graphically.

$$R_s = \frac{1}{\lim_{I \rightarrow 0} \frac{dI}{dV}} \quad \text{which is at } V_{oc} \text{ point} \quad (1.14)$$

$$R_{sh} = \frac{1}{\lim_{V \rightarrow 0} \frac{dV}{dI}} \quad \text{which is at } I_{sc} \text{ point} \quad (1.15)$$

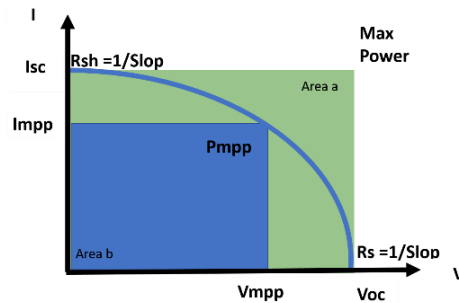


Figure 1.21. Illustration of R_s , R_{sh} , I_{sc} , V_{oc} , and maximum power and power point of a solar cell

The most important parameter about solar cells is conversion efficiency which is defined as the ratio of the output electrical power to the input optical power as given in Eq. 1.16. It gives how much of the solar power is converted to the electrical power.

$$\eta = \frac{P_{out}}{P_{in}} = \frac{I_{mpp} \times V_{mpp}}{P_{in}} = \frac{I_{sc} \times V_{oc} \times F.F.}{P_{in}} \quad (1.16)$$

The solar power on the earth's surface at AM 1.5 (P_{in}) is 1000.4 W/m^2 which means the solar cells with a size of $15.6\text{cm} \times 15.6\text{cm}$ receives input power (P_{in}) of 24.3 W . Another parameter determining the solar cell's performance is quantum efficiency. The external quantum efficiency (EQE) is the number of generated carriers per one incoming photons at each wavelength. In addition, the internal quantum efficiency (IQE) is the number of generated carriers over the number of absorbed photons at each wavelength. The relation between IQE and EQE is presented in Eq. 1.17. A typical EQE curve for Si solar cell is displayed in Figure 1.22.

$$IQE = \frac{EQE}{1 - \text{Reflection} - \text{Transmission}} \quad (1.17)$$

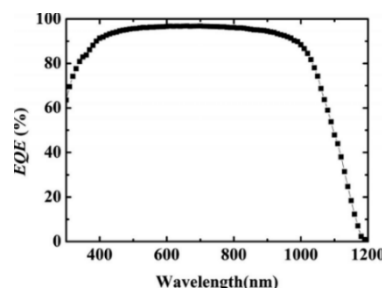


Figure 1.22. EQE curve indicating number of generated carriers over number of incoming photons

The conversion efficiency of different types of solar cells is quite versatile. The maximum achievable efficiency is increasing by advancing in the technology. However, there is a fundamental and physical limitation for efficiency, which is called Shockley–Queisser limit [7]. The Shockley–Queisser limit applies to single pn junction solar cell and consists of different efficiency loss mechanisms:

a) Blackbody radiation

Any material above absolute zero ($0^\circ \text{ Kelvin} = -273.15^\circ \text{ Celsius}$) emits electromagnetic wave which depends on its temperature. This emission is responsible for around 7% of energy loss in a solar cell.

b) Spectrum losses

The most important losses in an ideal solar cell is related to the mismatch between solar spectrum and the band gap of the device. Electrons can absorb photons with

energy above the bandgap, hence, photons with lower energy are not absorbed and are lost. On the other hand, when the energy of an incoming photon is higher than the bandgap, the electron absorbs the amount of energy which is required for the electronic transition from valence band to conduction band and the rest of energy will be converted to heat. This type of the loss is also called thermalization loss.

The abovementioned loss mechanisms depend on bandgap. The maximum possible efficiency versus semiconductor's bandgap is shown in Figure 1.23 which demonstrates that maximum possible efficiency is 33.7% at the bandgap of 1.34 eV.

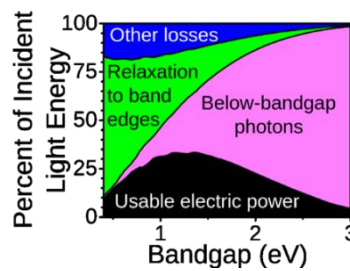


Figure 1.23. Usable part of incident light versus bandgap of absorbing the material

1.4.2. Different Types of Solar Cells

Many different types of solar cells are introduced which are made from different materials having different fabrication steps with specific properties and different efficiency ranges. The National Renewable Energy Laboratory (NREL) of U.S. Department of Energy publishes the Best Research-cell Efficiencies chart. The chart as of 17th August 2018 is shown in Figure 1.24 [8].

Four major groups of solar cells can be identified in this chart. First one is the multi-junction solar cells which gives the highest efficiency values under concentrated light. Because of very high production cost, in spite of very high efficiency (up to 46 %), they are used only in satellites for which the cost is not an important issue. The second class of solar cells consists of crystalline Si (c-Si) solar cells with an efficiency in the range of 17%-26%. c-Si solar cells have more than 95% market share in the commercial PV market today. Thin film solar cells are the third type of solar cells. This type of cells is made on glass or flexible substrate with relatively low cost. There

are commercially successful examples based on CdTe and CIGS. The fourth cell type includes all new solar cells with new materials and architecture. These technologies are either at the initial stage or not successful commercially so far. More explanation about these solar cell types are given in following section.

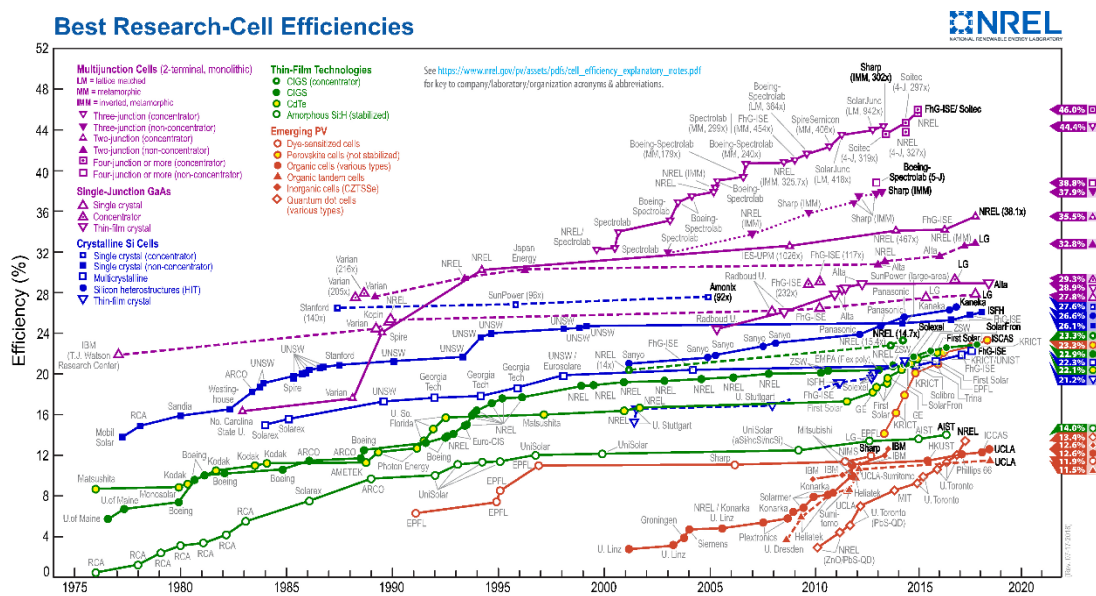


Figure 1.24. National Renewable Energy Laboratory (NREL) - Best Research-cell Efficiencies chart at 17.08.2018

1.4.2.1. Crystalline Si Solar Cells

The most widely used type solar cell is silicon-based solar cell because Silicon is very successful material for diode fabrication. It is cheap and abundant. In addition, fabrication steps are relatively simple and settled. The bandgap of silicon is 1.12 eV, so it can absorb photons with energy above 1.12 eV, which almost covers the whole visible spectrum. Si solar cells can be made on wafers with either mono-crystalline or multi-crystalline structure as it is shown in Figure 1.25. The multi-crystalline silicon contains many different grains with different crystallographic orientations. The disadvantages of grains boundaries of multi-crystalline silicon are low electrical and thermal conductivities, and relatively weak bonding. Solar cells made from mono-crystalline silicon have higher efficiency, however, multi-crystalline silicon solar cells have lower production cost.

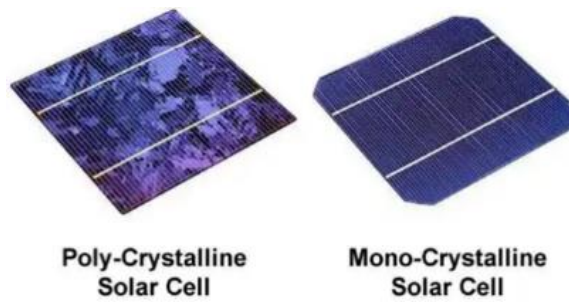


Figure 1.25. (right) Monocrystalline and (left) multi-crystalline silicon solar cell

1.4.2.2. Thin Film Solar Cells

Thin film solar cells which are fabricated using thin films of materials on either glass or flexible substrates. There are three commercially successful technology based on amorphous silicon, CdTe and Copper Indium Gallium Selenide (CIGS) which are shown in Figure 1.26. The amorphous Silicon bandgap is between 1.5 eV to 2.0 eV [13] so amorphous silicon solar cells can absorb photons with energy higher than 1.5eV. The amorphous silicon solar cell is one of the first fabricated solar cells [14] and widely used in early devices with built-in solar cells like calculators. However, tremendous increase in the performance/cost ratio of c-Si solar cells has pushed the a-Si technology out of market in recent years. In the CdTe solar cells, the absorber layer is made from CdTe. The CdTe is a direct bandgap material with a bandgap of 1.45eV. The CdTe is a stable material, however, Cd is toxic material and Te is rare material [15]. The CIGS can be deposited using various methods naming evaporation, printing, sputtering and electrodeposition. However, handling the composition of CIGS with four elements is hard [16].

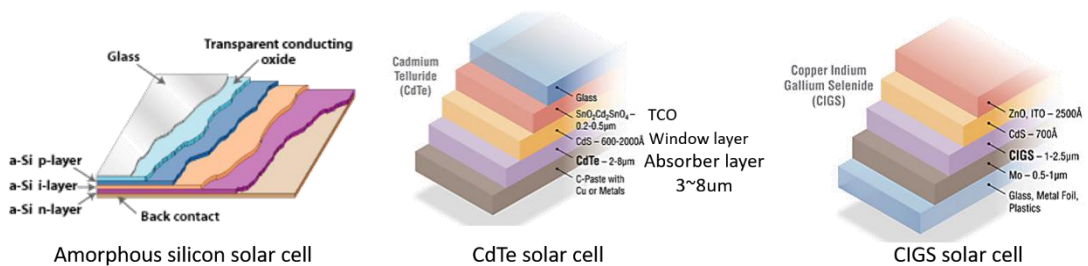


Figure 1.26. Schematic of (left) Amorphous silicon solar cell, (middle) CdTe solar cell, and (right) CIGS solar cell

1.4.2.3. Emerging Photovoltaics

Solar cells consisting of Dye-Sensitized Solar Cells (DSSC), Organic Solar Cells, and Perovskite Solar Cells and all new type of materials and devices are emerging technologies illustrated in Figure 1.27. The DSSC is easy to fabricate by conventional roll-printing techniques. It is semi-flexible and semi-transparent which offers various applications while the material is not expensive. Organic Solar Cell is made from polymers which its fabrication steps are solution-based processes, so the large volume fabrication is cheap. The bandgap of polymers is changeable by modifying the light-absorbing molecule. In addition, they are light, disposable, and flexible, however, they have low efficiency and low stability. The Perovskite Solar Cell is made from perovskite compounds as light absorbing material. They are cheap and have reached very high efficiency values in a short time. They also are flexible and light, however, their lifetime and toxicity are still under progress [17].

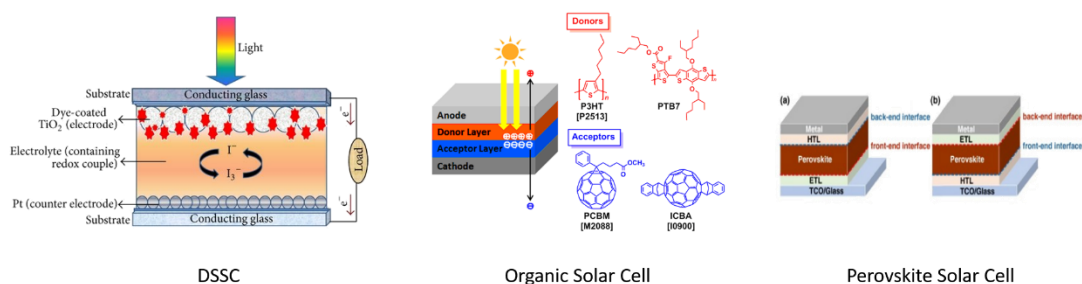


Figure 1.27. Schematic of (left) Dye-Sensitized Solar Cells (DSSC), (middle) Organic Solar Cells, and (right) Perovskite Solar Cells

Although many different types of solar cells have been investigated, the PV market is still dominated by crystalline Silicon solar cells. As it is seen in Figure 1.28, around 95% of installed solar cell modules are made of crystalline Silicon solar cells [12].

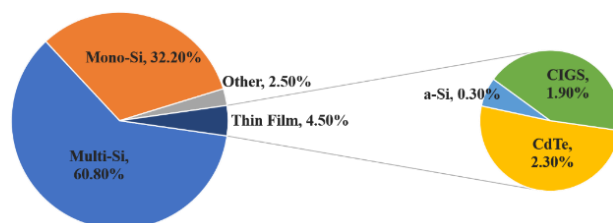


Figure 1.28. Market share of different types of solar cell in 2017

1.4.3. Solar Cell Fabrication Steps

In this section, fabrication steps of crystalline silicon solar cells are presented. These steps apply to both monocrystalline and multi-crystalline silicon solar cells. The general process flow is shown in Figure 1.29.

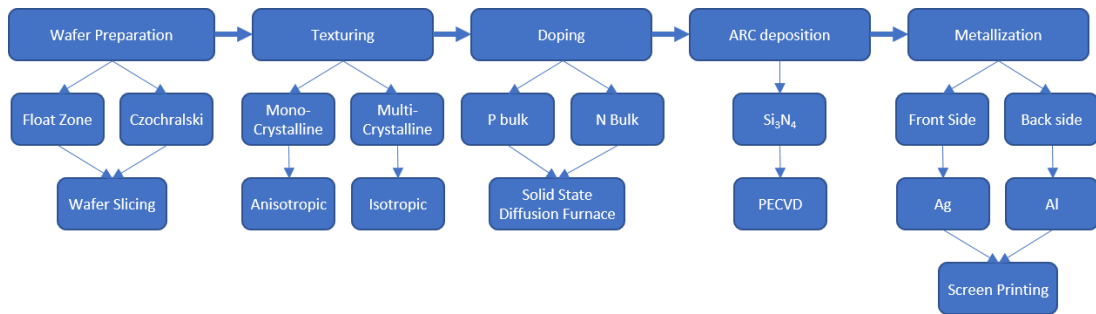


Figure 1.29. Schematic process flow of solar cell fabrication

1.4.3.1. Wafer Preparation

Fabrication steps start with preparing crystalline Silicon wafer. There are two main techniques to fabricate crystalline silicon wafers. In the Czochralski growth technique shown in Figure 1.30 (left), Silicon with the impurity less than 1 ppb is melted in quartz crucible. The single crystalline Silicon seed goes into the molten Silicon and is pulled out while rotating. The result is an ingot of single crystalline Silicon. In this method, the rate of pulling, melt temperature and rotation rate are controlling the size and quality of single crystalline Silicon ingot. In addition, it is possible to add dopants to the crucible for in-situ doping.

In the float zone technique shown in Figure 1.30 (right), the RF heating coil melts the Silicon locally and then, re-solidifies it. In the liquid phase, Silicon atoms can move and during the solidification, they tend to become single crystalline. In this technique, dopants and impurities prefer to stay in the liquid phase, so, the float zone technique can be used for refining when RF heating coil passes several times.

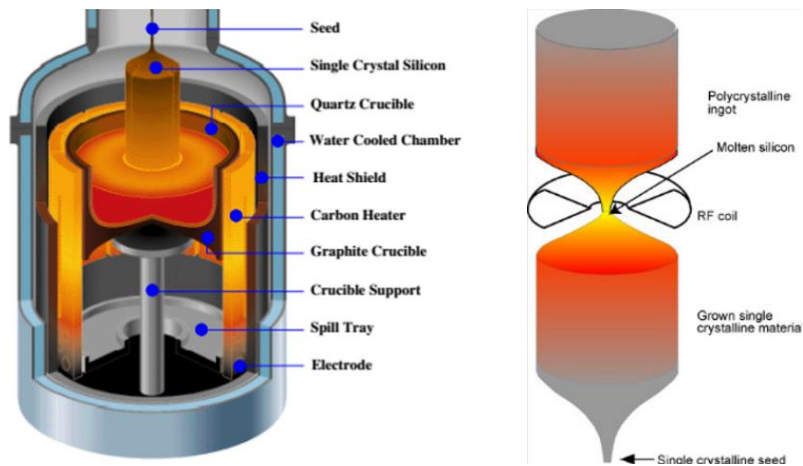


Figure 1.30. Schematic of (left) Czochralski growth system and (right) Float zone growth system

After the growth step, the ingot is cut into many wafers with specific thicknesses using different techniques like diamond coated wire (Figure 1.31). There are both wafers with saw damage and saw damage etched commercially available.

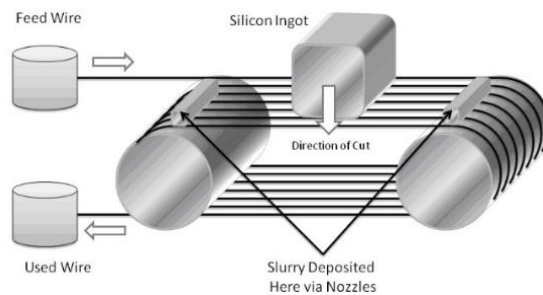


Figure 1.31. Diamond coated wire silicon slicing system

After cleaning step, the wafers are inspected for any possible damages. Then, they are being packed and ready to sell.

1.4.3.2. Texturing

Later, wafers must be textured to improve their light absorption. It is possible to quantify absorption by absorption coefficient which is the amount of light absorption for a given wavelength. The reciprocal of the absorption coefficient is the average distance for a photon to travel inside the material until it is being absorbed. As mentioned in section 1.3.1.2, materials can absorb photons with energy higher than their bandgap, however, the absorption is not constant for all wavelengths. The

dependency of absorption coefficient (α) to the wavelength and extinction coefficient (k) which is imaginary part of the complex refractive index is shown in Eq. 1.18.

$$\alpha = \frac{4\pi k}{\lambda} \quad (1.18)$$

According to Beer-Lambert law in Eq. 1.19, the intensity of absorbed light (I_a) depends on both α and the distance that light travels in the medium. Thus, photons with low wavelength can absorb near the surface while photons with high wavelength have higher absorption depth which is inverse of absorption coefficient (α^{-1}).

$$I_a = I_0(1 - e^{-\alpha d}) \quad (1.19)$$

The abovementioned absorption is corresponding to one surface as shown in Figure 1.32 (right). However, it is possible to increase absorption by increasing the number of bouncing of incident light on the surface as shown in Figure 1.32 (left).

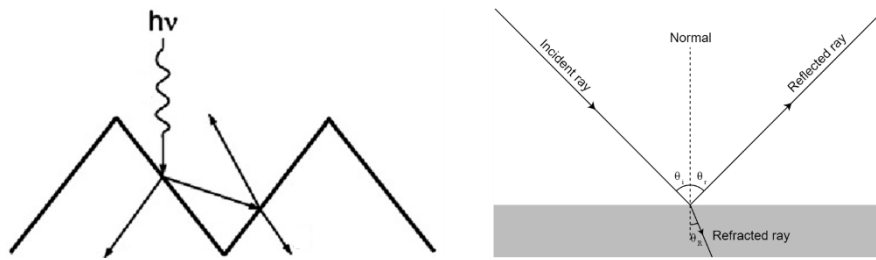


Figure 1.32. (right) Reflection of incident light from the flat surface (left) reflection of incident light from the textured surface which increases the absorption

In monocrystalline Silicon, the industrial texturing technique is well established using KOH [18]. The solution is anisotropic which etches (100) plane and stops at (111) plane which the angle between them is 54.7° . So, the textured surface will be randomly distributed pyramids with angle of 54.7° as shown in Figure 1.33.

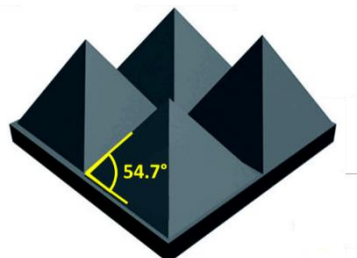


Figure 1.33. Pyramids with the angle of 54.7° as a result of chemical texturing using KOH solution

In contrast, it is not possible to use anisotropic solutions on multi-crystalline Silicon wafers because of the presence of different crystal orientation. So, several isotropic techniques are developed for texturing multi-crystalline Silicon. More information about texturing on multi-crystalline Silicon will be given in next chapters.

1.4.3.3. Doping

The doping is performed in a solid-state diffusion furnace. This process consists of two steps which are shown in Figure 1.34. In the pre-deposition step, an initial dosage of the dopant is introduced on the surface of the sample. The precursors of dopants are in gas phase and flown to the chamber which is shown in Figure 1.35. In the drive-in step, the sample is heated to the certain temperature, so that dopant atoms can penetrate inside sample from the surface and form the final doping profile.

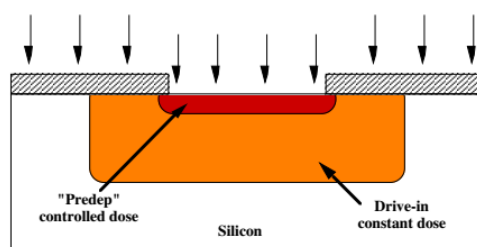


Figure 1.34. Penetration depth of doping for two steps of pre-deposition and drive-in

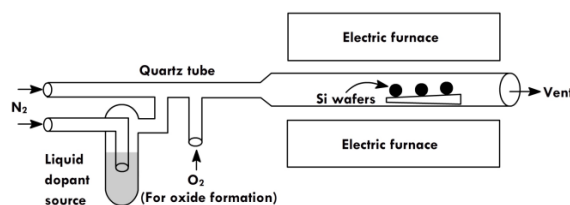


Figure 1.35. Chamber of the solid-state diffusion furnace

1.4.3.4. Anti -Reflection Coating

According to the optic law, the ratio of reflected light from the interface of two material depends on the refractive indexes of two surfaces. The refractive index of a material is the ratio of the speed of light in a vacuum (c) over the speed of light inside the material (v) and presented in Eq. 1.20. Equation 1.21 shows the relation between reflection and refractive indexes of two materials.

$$n = \frac{c}{v} \quad (1.20)$$

$$R = \left| \frac{\tilde{n}_2 - \tilde{n}_1}{\tilde{n}_2 + \tilde{n}_1} \right|^2 \quad (1.21)$$

Based on Eq. 1.23, the higher difference between refractive indexes of two materials leads to higher reflection from the interface. In order to decrease the reflection from the interface, it is possible to use an intermediate material between two main materials which is called the anti-reflection layer. The refractive index of the anti-reflection coating (ARC) must follow Eq. 1.22 to have an optimum reduction in the reflection. Since the refractive index depends on wavelength, the thickness of the anti-reflection coating can be optimized for specific wavelength as shown in Eq. 1.23.

$$n_{ARC} = \sqrt{n_2 \times n_1} \quad (1.22)$$

$$n_{ARC} d_{ARC} = \frac{\lambda}{4} \quad (1.23)$$

The refractive index of air is approximately one for all wavelengths. The refractive index of Silicon is shown in Figure 1.36 while the refractive index of the optimum material and the refractive index of Si₃N₄ are also shown in red and green respectively. Si₃N₄ is widely used as ARC layer on commercially fabricated solar cells.

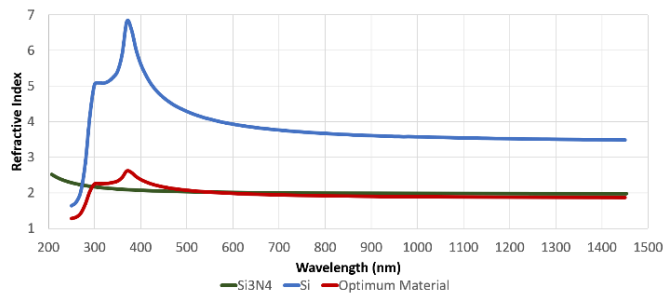


Figure 1.36. Refractive Index of Blue: Silicon, Red: Optimum Material, Green: Si₃N₄

In order to deposit Si₃N₄, Plasma Enhanced Chemical Vapor Deposition (PECVD) system is commonly used. In the CVD system, depositing materials precursors are silane (SiH₄) and either Nitrogen (N₂) or Ammonia (NH₄) which all are in the gas phase. Equation 1.24 and Eq. 1.25 give the reactions occurred in the chamber. In the PECVD system shown in Figure 1.37, the required energy for reactions to occur is provided by applying plasma in the moderate temperature around 250-400°C.

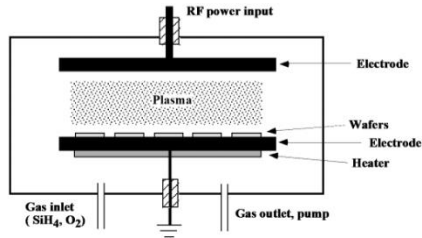
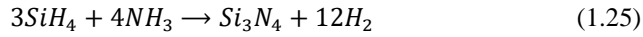
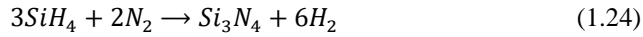


Figure 1.37. Schematic of PECVD Chamber

1.4.3.5. Metallization

The metallization consists of two part; the front-side and back-side metallization. Normally, both steps are done using the screen-printing technique. In the screen-printing technique, a metal paste is applied on the surface using mask and printing technique. The screen-printing technique is illustrated in Figure 1.38.

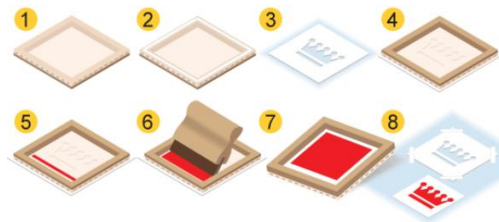


Figure 1.38. Steps of the screen-printing technique

The material used for front-side metallization is Silver (Ag) and for back-side metallization is Aluminum (Al). The front-side metallization mask for wafers with the size of 15.6 cm×15.6 cm has three or four busbars which are shown in Figure 1.39 (left, middle). The back-side Aluminum is printed at full screen (Figure 1.39 (right)).



Figure 1.39. Front Surface of the solar cell with (left) three busbars, (middle) four busbars; (right) back surface of a solar cell

After metallization steps, annealing is crucial to form electrical contacts on front and back side of the cell for electrical contacts. This annealing called firing and is also useful for the formation of the back surface field (BSF). When back-side Al is heated, the Al atoms become mobile and can penetrate inside p-type Silicon bulk from the rear side. The Al atoms act as an extra p-type doping in the Silicon semiconductor. The region between highly p-doped and lightly p-doped Silicon acts like a junction, so electrons are repelled from back side which decreases the chance of recombination at the back surface.

CHAPTER 2

A LITERATURE SURVEY ON SURFACE TEXTURING OF SI WAFER

2.1. Solar Cells

The photovoltaic effect has been discovered by Alexander-Edmond Becquerel in 1839 [19] [20]. According to his experiments, two Platinum electrodes with light sensitive coating like AgCl or AgBr in the solution, which is electrically conductive, can generate electricity under illumination like the sun light.

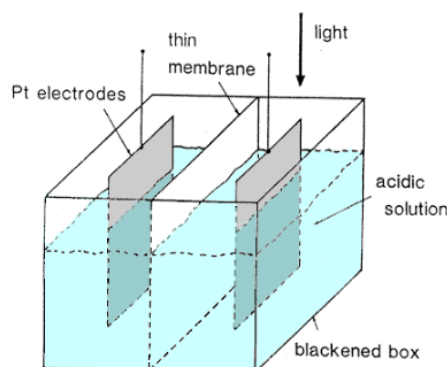


Figure 2.1. Becquerel's discovery of photovoltaic effect

Later, Adams and Day observed photovoltaic effects in solids between Selenium and Platinum in 1877 [21]. After years of research, the first Silicon based solar cell was fabricated in Bell Labs in 1954 with the efficiency of 6% by Chapin, Fuller, and Pearson [22].

Various investigations are going on to increase the efficiency of solar cells either by using new materials and new technologies or introducing new concepts like concentrated photovoltaic. As reported by M.A. Green [23], researchers are pushing the crystalline silicon based solar cells' efficiency to the physical limits [24] and they have reached more than 26% efficiency ($V_{oc}=726.6$ mV, $J_{sc}=42.62$ mA/cm², and F.F.=84.28 %) from monocrystalline silicon solar cell at ISFH [8].

2.2. Texturing

Texturing techniques are required to increase the absorption of incident light compared to the flat surfaces. The basics of texturing are given in Section 1.4.3.2. Due to fundamental crystallographic differences between monocrystalline and multi-crystalline silicon wafers, each type of wafers has different texturing techniques.

2.2.1. Mono Crystalline

Since monocrystalline wafers have surface with single crystallographic orientation, using anisotropic solutions is sufficient for texturing them. These anisotropic texturing solutions etch (100) Silicon surface faster than (111) surface which results in pyramid textured surface with angle 54.7° [25]. The mechanism is well explained by Seidel et al. [26]. From many different anisotropic chemical solutions, the most common of them are explained more in this section.

One solution is Tetramethyl Ammonium Hydroxide (TMAH) which is investigated in Toyota Central Research and Development Laboratories Inc. by O. Tabata et al [27]. Papet et al. reported that by using a solution containing 2% TMAH and 8% IPA at 80°C for 30 min, the weighted reflection of 13% without ARC and morphology of Figure 2.2 can be achieved.

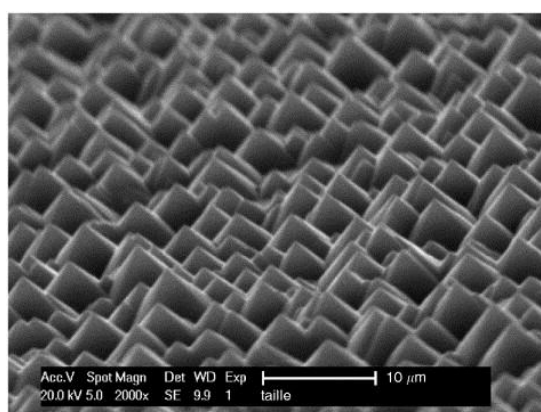


Figure 2.2. SEM of achieved morphology using TMAH reported by Papet et al.

Another solution is Ethylenediamine Pyrocatechol (EDP) which was investigated by R. M. Finn et al. in Bell Telephone Laboratories [28].

Among the anisotropic solutions, the general solution is the mixture of KOH and Isopropyl Alcohol (IPA) which was investigated by D. B. Lee at Semiconductor Laboratories at 1969 [18]. Another solution mixture of KOH consists of Polyvinyl Alcohol (PVA) [29]. Ximello Queibras investigated different mixtures of KOH solutions and optimized their parameters in his Ph.D. thesis. The results of his experiments are shown in Table 2.1. The morphologies achieved from KOH-PVA for 20min at 100°C (right) and KOH-IPA for 40min at 80°C (left) are shown below [29].

Table 2.1. Solar cell performance and optical results achieved by Ximello Queibras

| | <i>Weighted Reflection</i> | <i>Voc</i> | <i>Jsc</i> | <i>F.F.</i> | <i>η</i> |
|-----|----------------------------|------------|---------------|-------------|----------|
| | <i>%</i> | <i>mV</i> | <i>mA/cm2</i> | <i>%</i> | <i>%</i> |
| PVA | 12.6 | 625.7 | 37.0 | 76.8 | 17.8 |
| IPA | 11.5 | 625.4 | 36.6 | 77.1 | 17.7 |

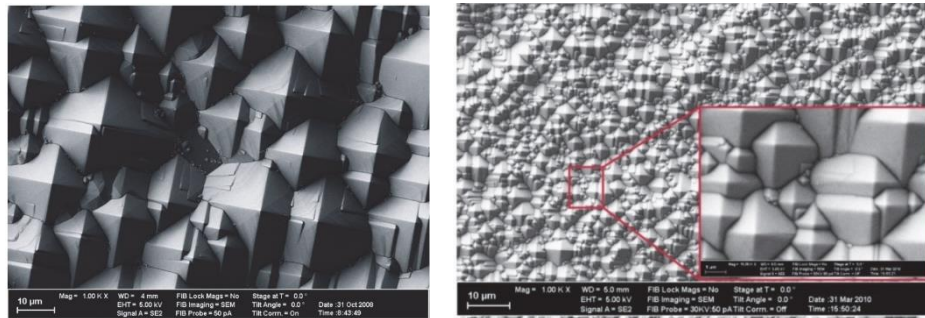


Figure 2.3. SEM images of KOH-IPA (left) and KOH -PVA (right) reported by Ximello Queibras

In addition to anisotropic solutions, isotropic solutions are also used for texturing monocrystalline wafers.

2.2.2. Multi Crystalline

Using anisotropic texturing methods are not efficient on the multi-crystalline Silicon wafers. However, there are some investigations using these texturing methods.

As reported by Es et al. from Middle East Technical University, using 3.7% KOH with 3.7% IPA at 70 °C for 45 min can lead to achieve weighted reflection around 23% and

solar cell's efficiency of 17.71% [30]. Figure 2.4 shows the SEM images of a textured sample.

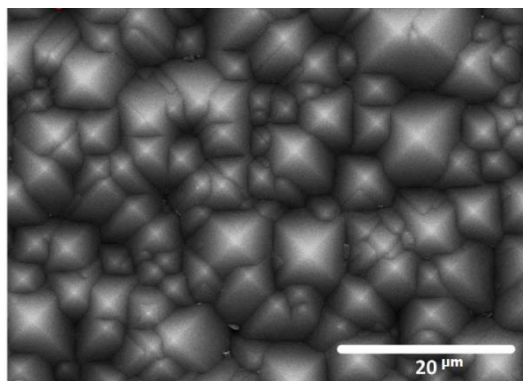


Figure 2.4. SEM image of a textured multi-crystalline Silicon sample reported by Es et al.

The effects of NaOH alkaline texturing method on the multi-crystalline wafers with different surface orientation is reported by Hylton et al. [31]. They have analyzed the reflection curves and SEM images of different facet orientations. The reflection curves of (left) high concentration NaOH as a saw damage etching and (right) low concentration NaOH as texturing techniques are presented in Figure 2.5. The SEM images of these techniques are illustrated in Appendix A.

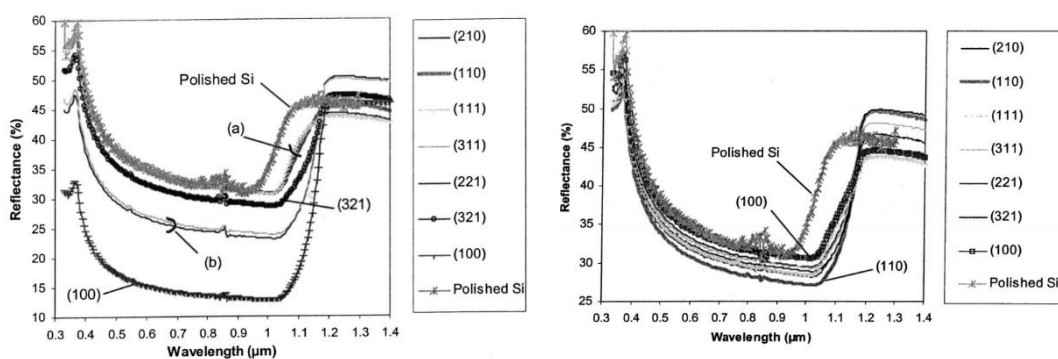


Figure 2.5. Reflection curves of (left) high concentration NaOH and (right) low concentration NaOH reported by Hylton et al.

The comparison between some isotropic and anisotropic texturing methods are reported by Macdonald et al. [32]. They have used the mixture of HF/HNO₃ as an isotropic texturing method, Reactive Ion Etching (RIE) as dry texturing method, masked RIE pyramids, and alkaline anisotropic etching. Unfortunately, no further

information about the processes is given. Figure 2.6 compares the reflection curves of fabricated samples (left) without ARC and (right) with ARC.

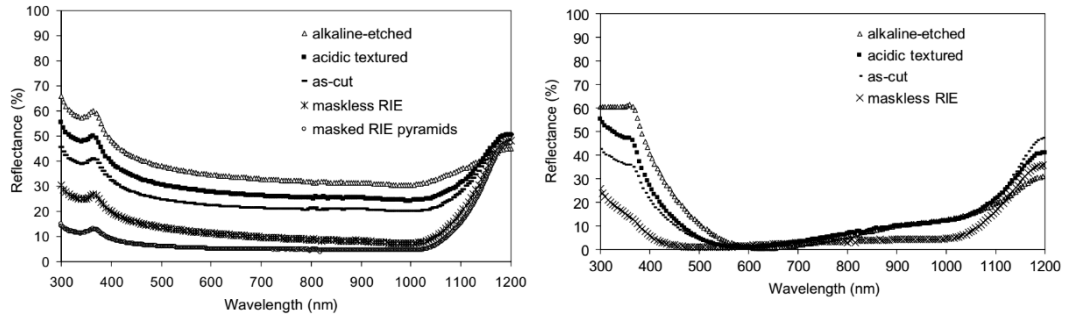


Figure 2.6. Reflection curves of samples (left) without ARC and (right) with ARC reported by Macdonald et al.

Figure 2.7 illustrates the SEM images from different morphologies achieved by Macdonald et al. (top right) acidic texturing (top left) alkaline texturing (bottom right) masked RIE (bottom left) mask-less RIE.

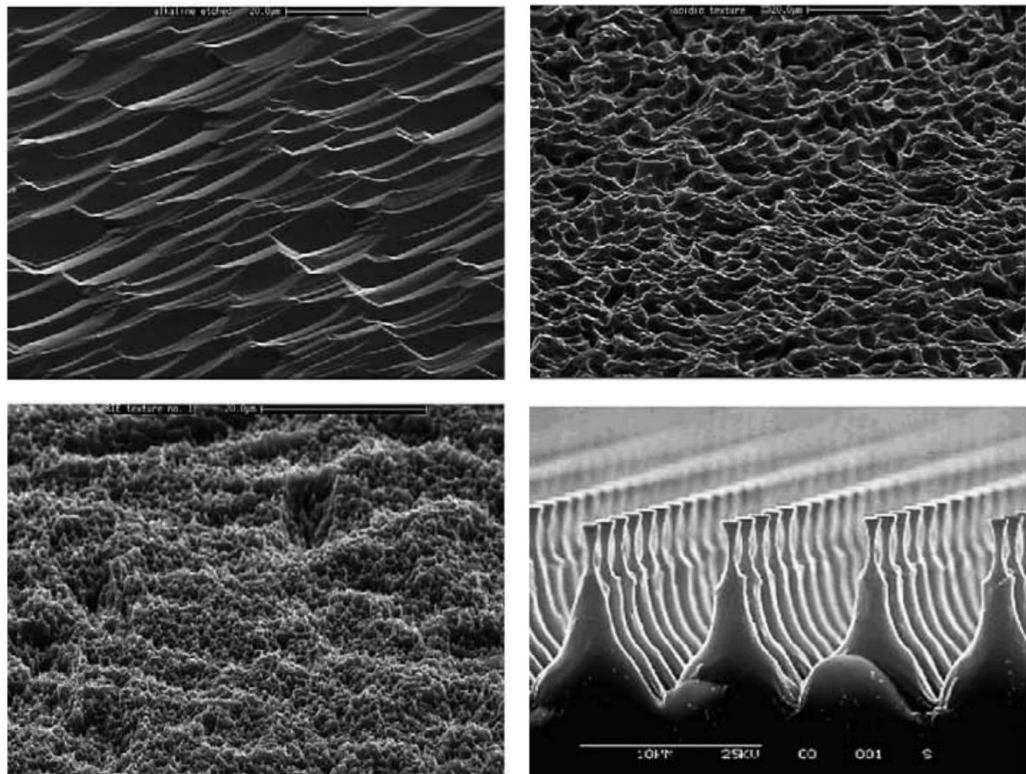


Figure 2.7. SEM images of (top right) acidic texturing (top left) alkaline texturing (bottom right) masked RIE (bottom left) mask-less RIE reported by Macdonald et al.

2.3. Laser Texturing with Post-Texture Cleaning

Since the anisotropic texturing methods are not functional for multi-crystalline Silicon wafers, the isotropic texturing methods are developed. One of the isotropic texturing methods employs the laser system.

The post-texture cleaning is required after laser texturing, many researchers use two step post-texture cleaning. As reported by Abbott and Cotter [33], the two step post-texture cleaning consists of one anisotropic cleaning using 25% NaOH for 3min at 40°C and one isotropic cleaning using mixture of HF, Nitric Acid and Acetic Acid (HNA) for 3 min. During the laser texturing process, they have used Q-Switched, Nd:YAG laser with wavelength of 1064nm and pulse width of 200ns. The SEM images shown in Figure 2.8 demonstrate the effects of each step excellently (left) as-textured, (middle) anisotropic cleaned, and (right) isotropic cleaned. In addition, the results of the fabricated double-sided buried contact solar cell are shown in Table 2.2.

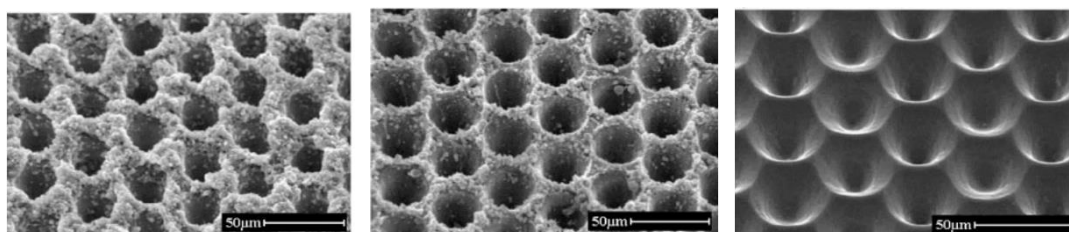


Figure 2.8. SEM images (left) as-textured, (middle) anisotropic post-texture cleaned, and (right) isotropic post-texture cleaned reported by Abbott and Cotter

Table 2.2. Result of fabricated double-sided buried contact solar cell reported by Abbott and Cotter

| | <i>Thickness</i> | <i>Area</i> | <i>V_{oc}</i> | <i>J_{sc}</i> | <i>F.F.</i> | <i>Efficiency</i> |
|------------------|------------------|-----------------------|-----------------------|--------------------------|-------------|-------------------|
| | <i>µm</i> | <i>cm²</i> | <i>mV</i> | <i>mA/cm²</i> | <i>%</i> | <i>%</i> |
| Laser Textured | 230 | 7.3 | 658 | 37.3 | 75.0 | 18.4 |
| Planar Reference | 260 | 8 | 650 | 31.3 | 73.0 | 14.6 |

Another laser texturing process using two step post-texture cleaning is reported by Nayak et al. [34]. They have used laser system with wavelength of 800nm, pulse energy of 0.6mj/pulse, pulse duration of 130fs, and laser pulse frequency of 1kHz. The samples were 2cm×2cm and post-texture cleanings were done using anisotropic NaOH solution and isotropic HNA solution. The SEM images of (left) as-textured, (middle) post-texture cleaned, and (right) after metallization are shown in Figure 2.9. In addition, the I-V curve of their best sample indicating the efficiency of 10.3% is presented in Figure 2.10.

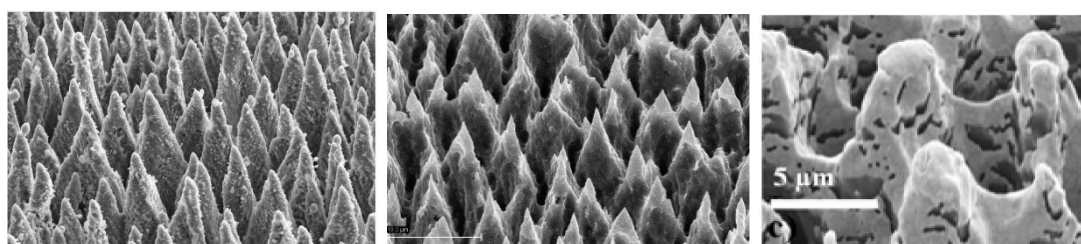


Figure 2.9. SEM images (left) as-textured, (middle) post-texture cleaned, and (right) after metallization reported by Nayak et al.

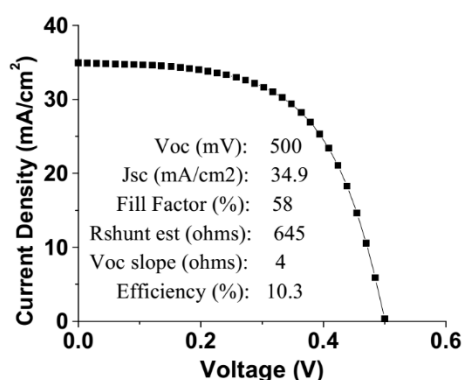


Figure 2.10. I-V curve of a sample reported by Nayak et al.

In another work from the same team, Iyengar et al. have reported better cell results which uses the same laser system but in SF₆ gas ambient [35]. With this development, they have reached V_{oc} of 507 mV, J_{sc} of 39.2 mA/cm², F.F. of 72%, and efficiency of 14.12%.

The morphology development through changing the post-texture cleaning duration using NaOH on the textured surface using laser system with wavelength of 800nm,

pulse energy of 0.6mj/pulse, pulse duration of 130fs, and laser pulse frequency of 1kHz is presented by Nayak et al. [36]. The SEM images of (top left) as-textured and post-texture cleaned using NaOH with durations of (top right) 5sec (bottom left) 10sec (bottom right) 20 sec are shown in Figure 2.11.

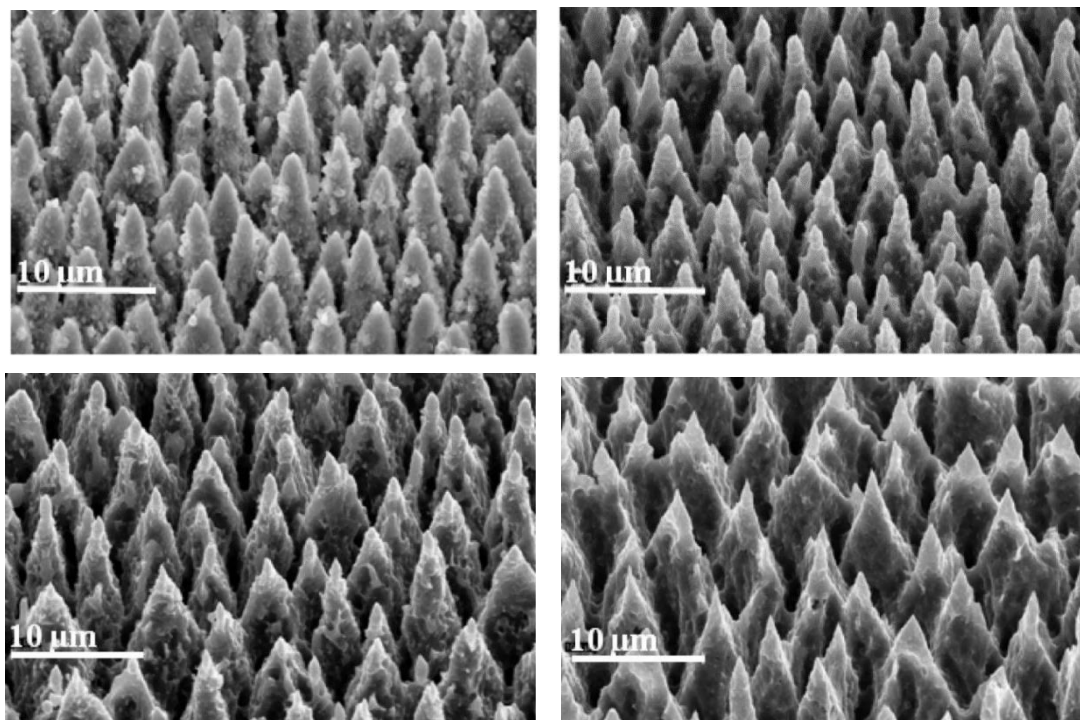


Figure 2.11. SEM images of (top left) as-textured and post-texture cleaned using NaOH with durations of (top right) 5sec (bottom left) 10sec (bottom right) 20 sec reported by Nayak et al.

The implementation of direct laser texturing (DiLaT) is reported by Zeilke et al. [37]. They have used Q-switched Nd:YVO₄ laser system with wavelength of 355 μm, laser pulse frequency of 50 kHz, pulse duration of 30 ns, and pulse energy of 6 μJ/shot. The samples in the study had dimensions of 2cm×2cm. After laser texturing, samples went through two step post-texture cleaning using 25% NaOH solution at 45°C for 3min and mixture of HF/HNO₃. The SEM image of the final structure is illustrated in Figure 2.12. In addition to SEM images, comparison between solar cell parameters and weighted reflection of final samples is presented in Table 2.3.

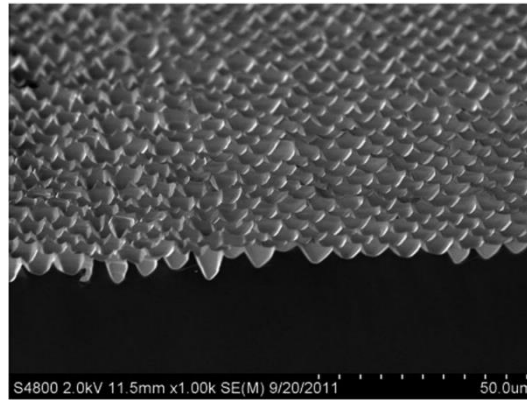


Figure 2.12. SEM image of the final structure reported by Zeilke et al.

Table 2.3. Comparison between solar cell parameter and weighted reflection reported by Zeilke et al.

| | <i>Weighted Reflection</i> | V_{oc} | J_{sc} | <i>F.F.</i> | <i>Efficiency</i> |
|---------------------------|----------------------------|----------|--------------------|-------------|-------------------|
| | % | mV | mA/cm ² | % | % |
| Planar | 15.3 | 626 | 35.5 | 75.3 | 16.7 |
| DiLaT / 3.2 μm | 7.3 | 618 | 39.3 | 73.6 | 17.9 |
| DiLaT / 3.8 μm | 7.6 | 618 | 38.2 | 74.2 | 17.5 |
| DiLaT / 5.8 μm | 14.4 | 620 | 35 | 71 | 15.4 |

In addition, usage of nanosecond laser texturing in different mediums is reported by Parmar and Shin from Perdue University [38]. They have used Ti:Sapphire femtosecond laser system with wavelength of 800nm, pulse energy of 1.0 mJ/pulse, and pulse width of 100 fs at laser pulse frequency of 1 kHz . They textured 3cm \times 1cm samples in two mediums of air and deionized water (DI water). Figure 2.8 shows the SEM images of textured samples in (left) air and (right) DI water. In addition, the reflection curves of resultant textured samples are shown in Figure 2.9.

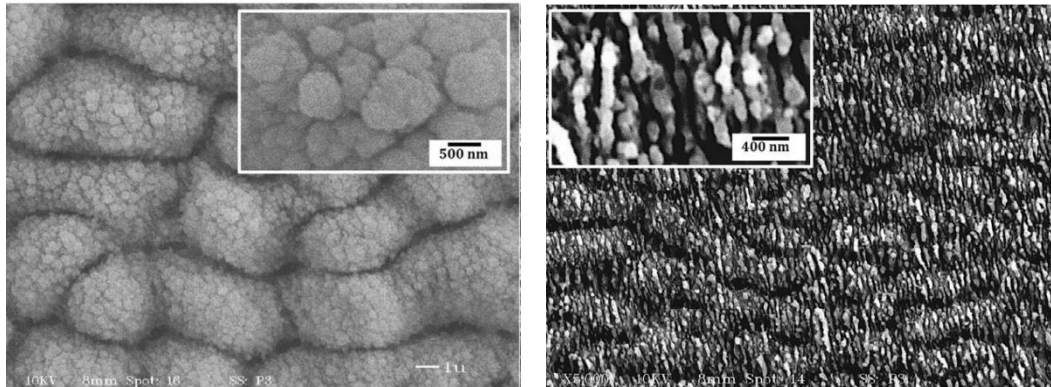


Figure 2.13. SEM images of textured samples with femtosecond laser in (left) air and (right) DI water mediums reported by Parmar and Shin

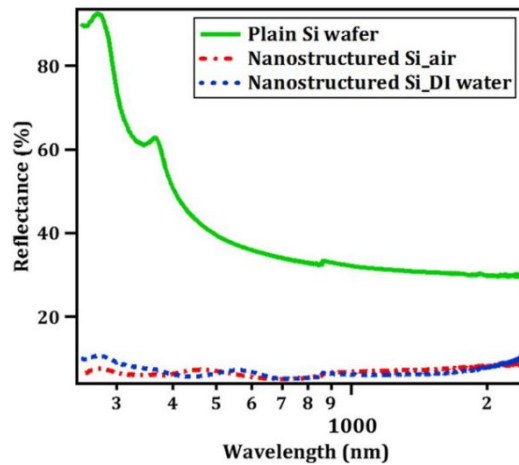


Figure 2.14. Reflection curves of samples textured with femtosecond laser in air and DI water mediums reported by Parmar and Shin

There are some studies which used one post-texture cleaning step like the experiment reported by Dobrzanski et al. [39]. In their study, they have used Q-switched Nd:YAG laser system with wavelength of 1064nm, power of 50W, laser pulse frequency of 15kHz, and spot size of 10 μ m. The samples in the study were 5cm \times 5cm. The post-texture cleaning process is done using 20% KOH solution at 80 $^{\circ}$ C for 10min and 20min. In addition, two different patterns have been investigated. The surface morphology developments are shown in Figure 2.15 for line groove pattern and Figure 2.16 for criss-cross pattern while in both figures, (left) as-textured and post-texture cleaned for (middle) 10min and (right) 20min are shown.

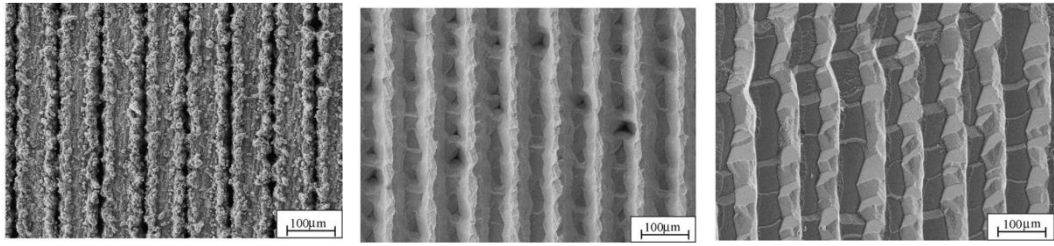


Figure 2.15. SEM images of (left) as-textured and post-texture cleaned for (middle) 10min and (right) 20min for line groove pattern reported by Dobrzanski et al.

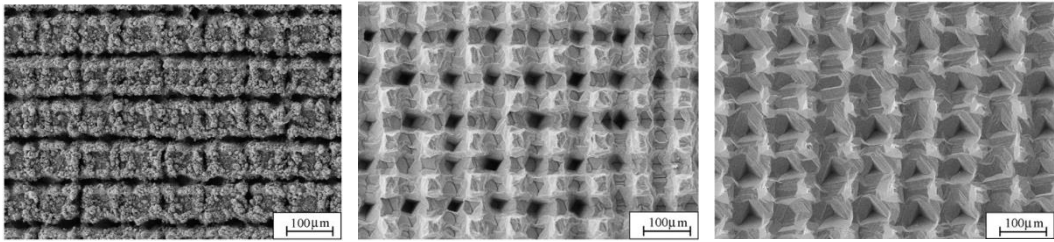


Figure 2.16. SEM images of (left) as-textured and post-texture cleaned for (middle) 10min and (right) 20min for criss-cross pattern reported by Dobrzanski et al.

The reflection curves of the experiment reported by Dobrzanski et al. are shown in Figure 2.17 for (left) line grooves and (right) criss-cross pattern. Finally, the solar cells' performance and weighted reflection comparison are mentioned in Table 2.4

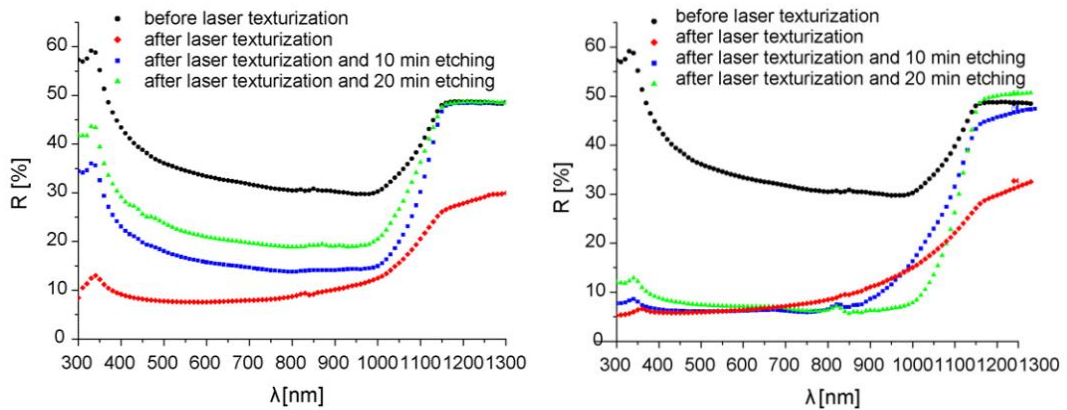


Figure 2.17. Reflection curves of (left) line grooves and (right) criss-cross pattern reported by Dobrzanski et al.

Table 2.4. Solar cell performance and weighted reflection comparison reported by Dobrzanski et al.

| Pattern | Post-Texture Cleaning Duration | Weighted Reflection | V_{oc} | J_{sc} | F.F. | Efficiency |
|------------------------|--------------------------------------|------------------------|----------|--------------------|------|------------|
| | | % | mV | mA/cm ² | % | % |
| Planar | -- | 34.1 | 551 | 630 | 0.74 | 10.2 |
| | -- | 11.6 | 259 | 190 | 0.48 | 0.9 |
| Line Groove | 10min | 18.2 | 537 | 507 | 0.62 | 6.7 |
| | 20min | 23.6 | 561 | 679 | 0.73 | 11.1 |
| Criss-Cross Pattern | -- | 9 | 214 | 120 | 0.39 | 0.4 |
| | 10min | 9.1 | 522 | 657 | 0.63 | 8.6 |
| | 20min | 8.3 | 575 | 724 | 0.72 | 11.9 |

In the next chapter, a developed isotropic texturing method is proposed. In the proposed method, laser texturing and post-texture cleaning are investigated and the improvements are presented.

CHAPTER 3

EXPERIMENTAL METHODS

3.1. Introduction

As mentioned in the solar cell's working principles (Section 1.4.1), one of the important factors which determines the efficiency of solar cells is their ability to absorb incident light. Based on solar cell's fabrication steps (Section 1.4.3.2), one of the fabrication steps is texturing. Moreover, the absorption coefficient (α) and its formula are explained in that section.

The aim of texturing is to enhance the absorption of incident light by increasing the number of bounces of incident light off the surface. Figure 3.1 shows the absorption of light with one and two incident light bounces. In general, more than two bounces can happen.

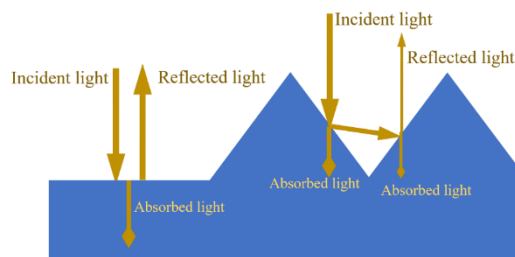


Figure 3.1. Effect of texturing on the surface

For instance, if the absorption of the incident light is $A\%$ at the flat surface, then the reflection is $\%R=100-A$. However, the absorption from the textured surface by considering only two incident light bounces is $A_{total}=A+RA$. Thus, the absorption is increased by $\%RA$. Therefore, higher absorption can be achieved by increasing the number of bounces. While increasing the surface's roughness improves light absorption, it also increases the recombination at the surface. Hence, a moderate surface texturing is required.

In this chapter, the isotropic texturing method using laser on the crystalline Silicon wafer is described. In addition, the post-texture cleaning method is investigated to clean laser damaged surface. Finally, solar cell fabrication steps based on proposed method are explained.

3.2. Laser Texturing

In section 2.2, different types of texturing and their effects on the surface have been described. In this section, we proposed an isotropic texturing technique using laser. In this study, EO Technics- Supermarker GF 311 nanosecond IR laser with a wavelength of 1064nm and maximum power of 30W is used. Figure 3.2 shows the setup and different parts of the equipment. The laser setup has galvo scanner motor so that the working distance from the laser to different regions of wafer is constant. The working distance of setup is 325.1 mm. We have prepared a new stage made from metal to increase heat transfer from the wafer to decrease the damage on the wafer. Since the intensity of the laser is high, there are many silicon ablated residues; therefore, we added Nitrogen gas flow to the setup to remove ablated residues from the surface.

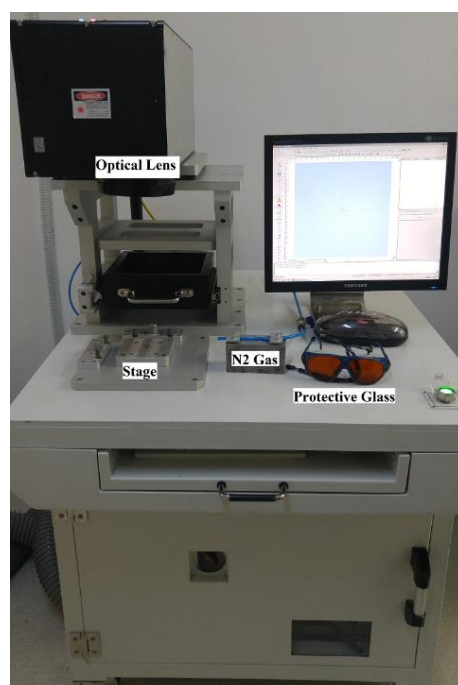


Figure 3.2. Laser equipment. Stage, N2 Gas, protective Glass, Optical Lens

The interface of software for using the setup is shown in Figure 3.3 (left). In this software, many different actions are possible to perform. It is possible to draw different shapes from lines to arcs and elliptic shapes and also, texts. It is also possible to hatch the closed shapes with different properties. In addition, it is possible to merge or align shapes.

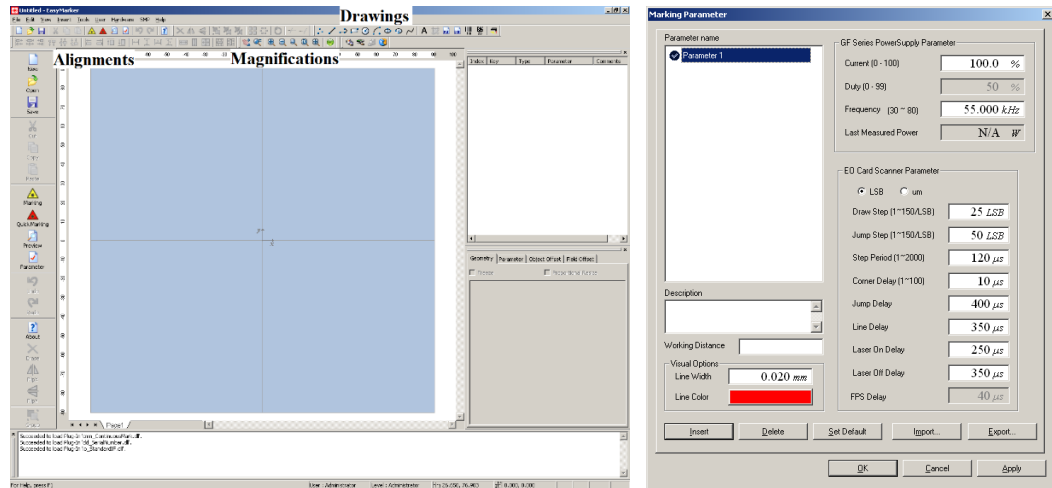


Figure 3.3. Interface of laser setup software showing Drawing, Magnification, and Alignment sections (left), Laser and scanner parameters (right)

The laser parameters configuration page is shown in Figure 3.3 (right). In this figure, laser parameters are Laser Pulse Frequency [kHz] which is between 30kHz and 80kHz, Power [%] which its maximum value is 30W, and Duty Cycle [%] which is fixed on 50%. In addition, it is possible to change the laser scanner motor parameters. These parameters are Draw Step [LSB] which is the distance while the laser is on and Step Period [μ s] which is the time unit of draw step. Smaller draw step results in more accurate shape, but longer time will be required.

After drawing the desired shape, it is also possible to change the geometry of the shape. The geometry section is customized for each type of shapes and is shown in Figure 3.4 (a) elliptic arc and (b) square.

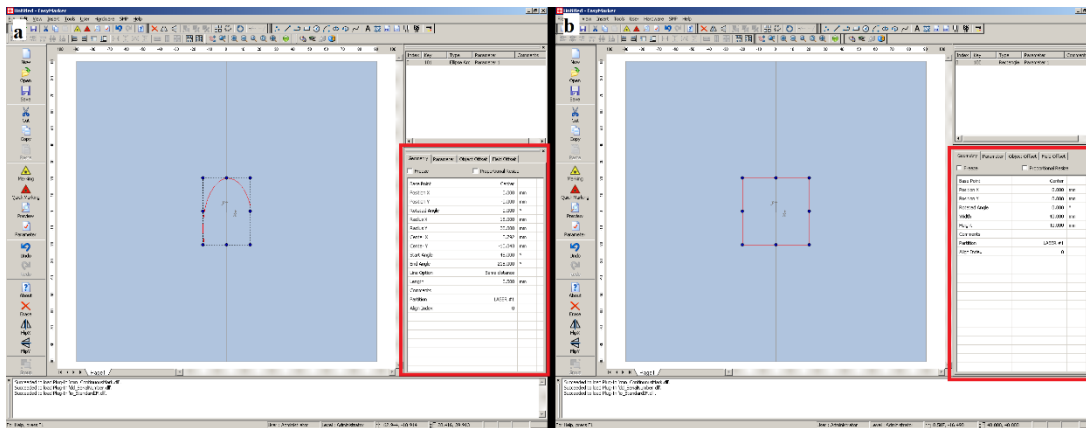


Figure 3.4. Geometry options of (left) elliptic arc (right) square

The morphologies that have been used for current study is either parallel lines or perpendicular lines. The parallel lines are drawn using line and the perpendicular lines are drawn using hatch feature in a way that the square is drawn first and then, its inside is hatched with different options.

In this study, the laser parameters, laser scanner motor parameters, and different morphologies are modified and adjusted to have the optimum surface structure in terms of weighted reflection and open circuit voltage. The results of this optimization are presented in section 4.1.

3.3. Post-Texture Cleaning

In general, laser texturing damages the surface. The surface roughness is good for light trapping purposes. However, it increases recombination due to sharp edges. To enhance surface structure after laser texturing, post-texture cleaning step is applied.

For the current study, high concentration and high temperature KOH solution has been used. Although KOH solution is considered as an anisotropic solution in section 2.2.1, with high temperature and high concentration it becomes isotropic solution. To perform post-texture cleaning, the required amount of KOH is weighted and solved in water. Then, the solution is heated up to the desired temperature using hot plate. Finally, the samples are dipped into the solution for intended durations. The results of

this process are expressed by measuring their weighted reflections and taking their SEM images in section 4.2.

3.4. Solar Cell Fabrication

The solar fabrication steps are shown in Figure 3.5. In this figure, blue blocks are fabrication steps and yellow blocks are characterization steps between fabrication steps. The solar cell fabrication steps including doping, ARC deposition, metallization, and firing are not optimized for the samples. Each step is explained further in the following section.

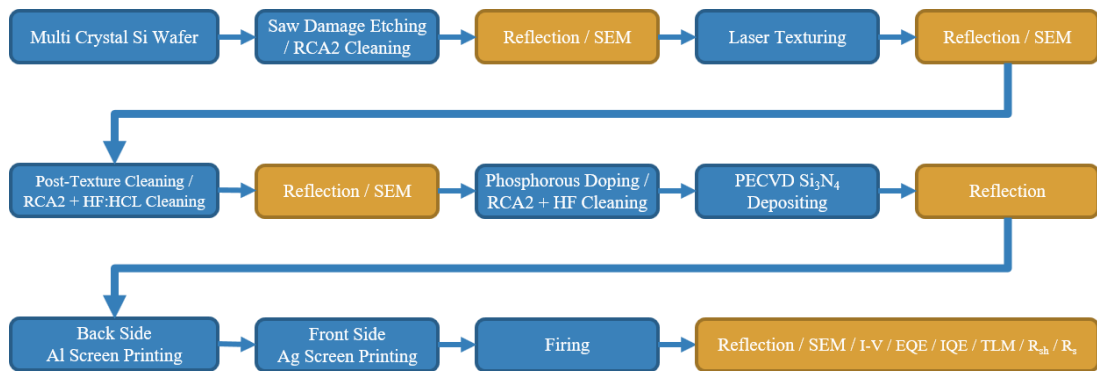


Figure 3.5. Schematic of solar cell fabrication process in which blue blocks are fabrication steps and yellow blocks are characterization steps

3.4.1. Wafer Preparation

For current study, both monocrystalline and multi-crystalline Silicon wafers are used to perform a comprehensive investigation. Monocrystalline Silicon wafers are bought from FerroTec company with specifications of Boron-doped, 1-3 Ω .cm, and thickness of 180 μ m with 15.6 \times 15.6 cm² area. The mono- and multi-crystalline Silicon wafers are bought from DC wafers company with parameters of Boron-doped, 1-3 Ω .cm, and thickness of 200 μ m with area of 15.6 \times 15.6 cm². Both types of wafers are saw damage removed via KOH solution with 20% concentration at 80°C for 4 min.

3.4.2. Texturing

Texturing step has been discussed in the section 3.2.

3.4.3. Doping

The phosphorous doping has been performed using Semco Qtherm solid state diffusion furnace. The doping precursors are POCl_3 and O_2 , the chamber pressure is 400mBar, and the furnace temperature is 838°C.

3.4.4. ARC Deposition

The Silicon Nitride (Si_3N_4) as an anti-reflection coating has been deposited using Semco Qtherm PECVD system shown in Figure 3.6. The ARC deposition has been done using SiH_4 and NH_3 gases at temperature of 380°C and pressure of 1000 mTorr.



Figure 3.6. Picture of Semco Qtherm PECVD / solid state diffusion system

3.4.5. Metallization

The front metallization using Silver (Ag) and the rear metallization using Aluminum (Al) are done by EKRA screen printing system which is shown in Figure 3.7.



Figure 3.7. Picture of EKRA screen printing system

After metallization step, the annealing is crucial. This annealing process called firing and has been done using BTU International firing system which is shown in Figure 3.8. The firing belt speed is 500 mm/min at 900°C.



Figure 3.8. Picture of BTU International firing system

3.4.6. Cleaning Step

Between fabrication steps, several cleaning steps are required to remove different types of contaminations. Three different cleaning procedures has been performed; i.e. RCA 1 which contains Ammonium Hydroxide (NH_4OH), Hydrogen Peroxide (H_2O_2), and deionized water (DI water) with ratio of 1:1:5 respectively at $70\pm 5^\circ\text{C}$ to remove organics and particles from sample; RCA 2 which contains Hydrogen Peroxide (H_2O_2), Hydrochloric Acid (HCl), and deionized water (DI water) with ratio of 1:1:5 respectively at $70\pm 5^\circ\text{C}$ to remove metal ionic contaminations, and mixture of HF and HCl and deionized water (DI water) at room temperature with ratio of 1:1:10 to stop the post-texture cleaning process of KOH and remove RCA induced SiO_2 .

3.5. Characterization Methods

The characterization steps are shown in yellow blocks in Figure 3.5. The characterizations are also performed after laser texturing step and post-texture cleaning step individually to determine the effects of these steps before fabricating the solar cell.

3.5.1. Scanning Electron Microscopy (SEM)

One of the most used characterization techniques is taking SEM images. The SEM images are taken from the surface which reveals the surface morphology. In this technique, electrons are generated at LaB₆ electron gun and accelerated toward samples by applying voltage (Electron High Tension-EHT). These electrons penetrate inside the sample and generate secondary electrons which leave the sample and are captured by the detector. The Zeiss Evo HD 15 is used for taking SEM images.

3.5.2. Reflection Measurement

During conducting the experiments, two different reflection setups have been used. The first setup is shown in Figure 3.10 in which the associated LabView software just records the intensity measured by the detector. In this case, other calculations must be done manually. In order to make the calculations easier, a MATLAB User Interface (UI) is written which is shown in Figure 3.9. The MATLAB codes for running in MATLAB's workspace (without UI) are presented in Appendix B.

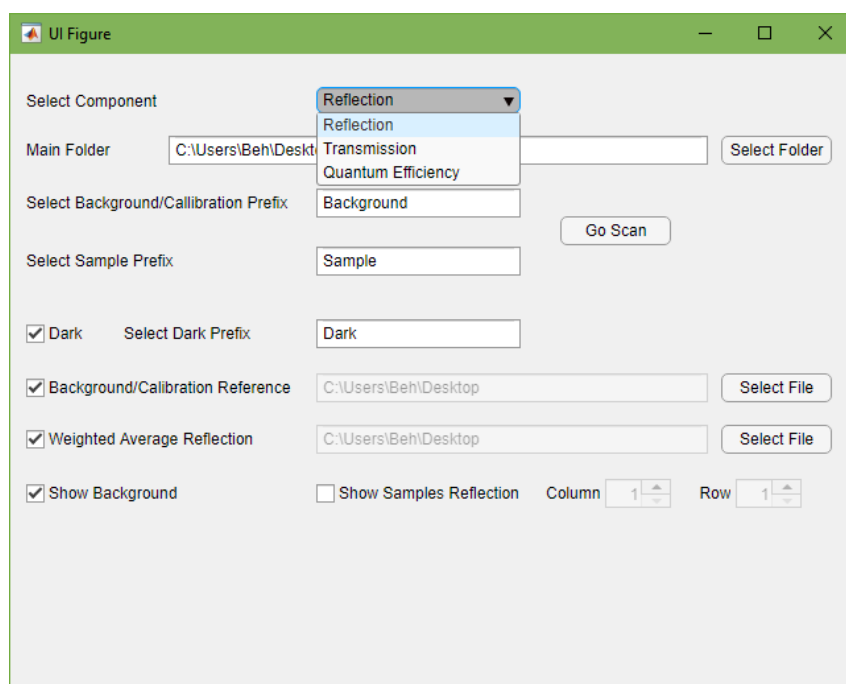


Figure 3.9. MATLAB GUI for reflection/transmission/EQE/IQE calculation

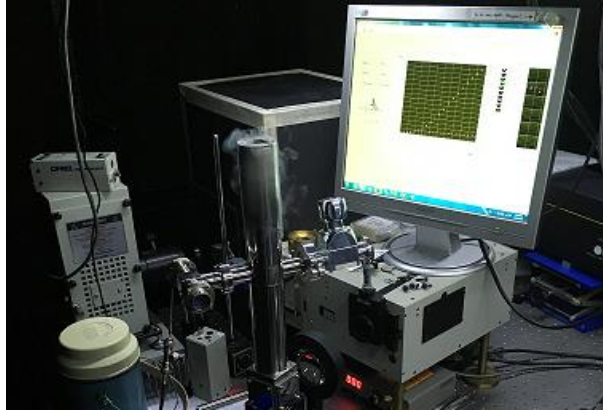


Figure 3.10. First reflection/transmission/EQE measurement setup

The other reflection is Bentham PVE300 Photovoltaic EQE (IPCE) and IQE solution. This setup is shown in Figure 3.11 and its software is capable to calculate reflection.

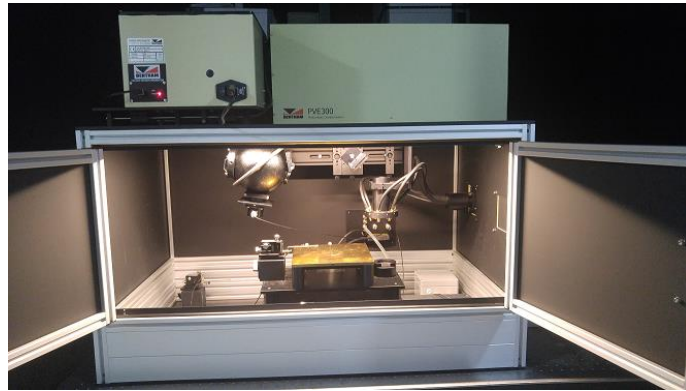


Figure 3.11. Bentham PVE300 Photovoltaic EQE (IPCE) and IQE

In both devices, BaSO₄ reference sample is measured first, then, the reflection of samples is calculated based on the reference sample which is calibrated by I_{calibration}. Equation 3.1 shows the formula for calculation sample's reflection from reference sample where I is the measured intensity.

$$R = \frac{I_{sample}}{I_{reference} / I_{calibration}} \times 100 \quad (3.1)$$

In other to have better comparison among reflection curves, the weighted reflection based on AM 1.5 can be calculated using Eq. 3.2.

$$WR = \frac{\int Reflection \times AM\ 1.5}{\int AM\ 1.5} \times 100 \quad (3.2)$$

3.5.3. Quantum Efficiency Measurement

To measure the external quantum efficiency, the same setup as the reflection setup is used. However, the measuring step is different. In this measurement, the detector is directly placed in front of light, so the detector measures the intensity of the incoming light and calculates photon count. Later, the sample is placed in front of light and the current generated from the sample is measured. Then, EQE can be calculated from Eq. 3.2 where I is the measured intensity, DR is the detector responsivity, h is the Planck's constant ($6.626 \times 10^{-34} \text{ J.s}$), c is the speed of light in the vacuum ($3 \times 10^8 \text{ m.s}^{-1}$), and q is the electronic charge constant ($1.6 \times 10^{-19} \text{ C}$).

$$EQE = \frac{I_{sample}}{I_{reference}} \times \frac{hc}{\lambda q} \times DR \quad (3.3)$$

To calculate the internal quantum efficiency, reflection and transmission and external quantum efficiency must be measured first. Then, IQE can be calculated using Eq. 1.19 which is explained in section 1.4.1.

3.5.4. Lifetime Measurement

For measuring the lifetime and implied V_{oc} (iV_{oc}), Sinton instrument WCT 120 is used. The sample is placed on the center of the stage and the setup performs the measurement. Depending on the lifetime, transient mode or Quasi-Steady-State Lifetime (QSS) mode is used. In the transient mode, life time is high; hence, the carriers can be generated by a short pulse of light and the decay in the carrier density is measured over time. In QSS mode, life time is low; hence, the steady light will generate carriers to measure carrier lifetime. To extract iV_{oc} value from the given figures, the minority carrier density is considered to be 10^{15} .

3.5.5. I-V Curve Measurement

The I-V setup is QuickSun 120CA-XL flash solar simulator at AM 1.5G conditions. The setup is shown in Figure 3.12 (left) and the corresponding software is shown in Figure 3.12 (right). The measurement gives I-V curve as well as R_s , R_{sh} , FF, V_{oc} , I_{sc} through the software report.



Figure 3.12. QuickSun 120CA-XL for measuring I-V curve (left) and corresponding software (right)

3.5.6. TLM Measurement

The TLM (Transmission Line Measurement) measures the contact resistance of metallization. For this measurement, samples are cut with the width of 1cm by laser. Then, the resistance between one finger and other figures is measured as function of length. The schematic of the measurement is shown in Figure 3.13.

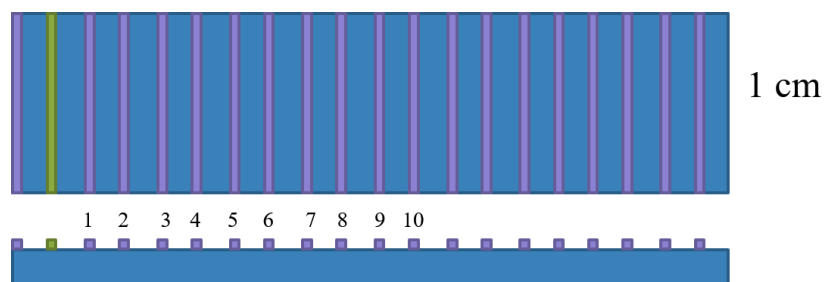


Figure 3.13. Schematic of TLM measurement resistance

To have accurate measurement, the resistance is calculated from the slope of I-V curve of contact. Then, these resistances are plotted together to calculate the contact resistance. It is also possible to calculate the semiconductor resistance. The general plot of TLM is shown in Figure 3.14 and the equations below indicate the calculations. In these equations, metal resistance (R_m) is neglected since it is much lower than metal-semiconductor resistance (R_{m-sc}) and semiconductor resistance (R_{sc}).

$$R_T = 2R_m + 2R_{m-sc} + R_{sc} \quad (3.4)$$

$$R_{sc} = R_s \frac{L}{w} \quad (3.5)$$

$$R_T = \frac{R_s}{w} L + 2R_{m-sc} \quad (3.6)$$

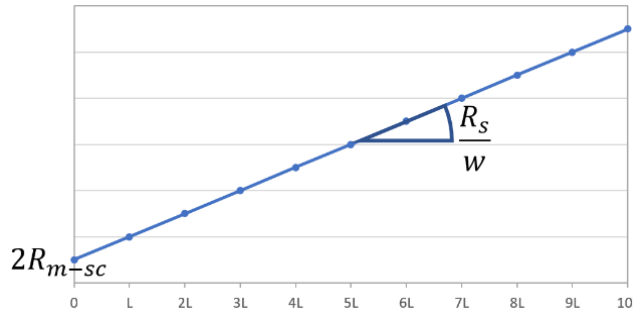


Figure 3.14. Resulting graph from TLM measurement

3.6. Quokka 2 Analysis

Quokka 2 is a simulation tool which can be used for the Free Energy Loss Analysis (FELA) [25]–[27]. The figure of software is shown in Figure 3.15. The generation file contains different sections; some parts are optional and some parts are essential for simulation. For current analysis, only essential parts are kept in the code which are: **Geometry** in which the geometry of solar cell’ unit cell will be described; **Bulk Properties** which indicates the parameters of bulk like doping type, resistivity, lifetime, and etc.; **Front and Rear boundaries** which determine the doping parameters of front and rear like sheet resistance, junction depth, reverse saturation current, and etc.; **Generation** which shows the generation profile in Z direction; **External Circuit** which is about parameters like R_s and R_{sh} . The complete generation file’s code for Quokka 2 analysis is declared in Appendix C.

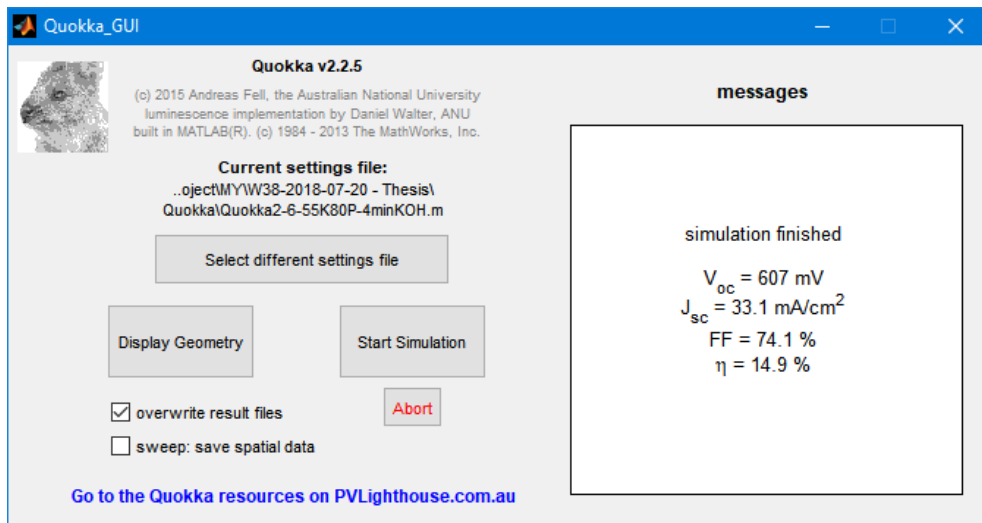


Figure 3.15. Figure of Quokka 2 simulation software

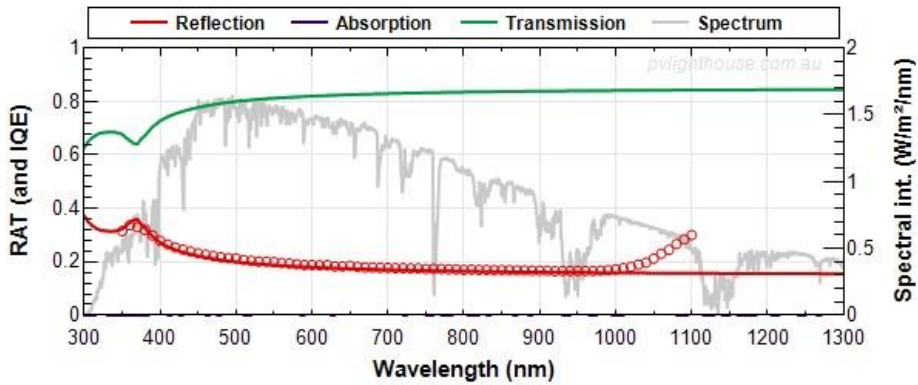
In order to extract the generation profile for Quokka 2 analysis, OPAL 2 simulation tool [28] is used. In this online simulation tool, the surface layers and morphology are defined. Later, the measured reflection and IQE of samples can be loaded. Then, the software generates the reflection, transmission, and absorption curves. It is also possible to find the thickness of layers by fitting the generated curves with experimental measurements. Figure 3.16 shows the input parameters of OPAL 2 and Figure 3.17 shows the generated optical curves. Finally, the generation profile of the fitted curves can be downloaded as spreadsheet file.



Figure 3.16. Input parameters of OPAL 2 simulation tool

Outputs

| Reflections | Unique paths | Fraction | Photon current | | mA/cm ² | Fraction |
|----------------|--------------|----------|-----------------------|-----------|--------------------|----------|
| 1 reflection | 1 | 25.0% | Incident | J_{Inc} | 43.85 | 100.0% |
| 2 reflections | 2 | 69.4% | Reflected | J_R | 7.91 | 18.0% |
| 3 reflections | 4 | 5.6% | Absorbed in films | J_A | 0.00 | 0.0% |
| 4+ reflections | 1 | 0.1% | Absorbed in substrate | J_G | 35.94 | 82.0% |
| Total | 8 | 100.0% | | | | |



Plot vs depth:

Simulated vs experimental reflection:
 Over λ range to nm
 RMSE of fit

Figure 3.17. Output of OPAL 2 simulation tool

In the next chapter results of proposed laser texturing process and post-texture cleaning process will be demonstrated.

CHAPTER 4

RESULTS AND DISCUSSIONS

4.1. Laser Texturing

In the laser texturing, the shape, depth, and spacing between laser-ablated spots are the critical parameters and must be optimized by adjusting the laser parameter. The speed of laser texturing (S) does not depend on the laser pulse's frequency and it only depends on the laser scanner motor parameters and is formulated as shown in Eq. 4.1.

$$S [\text{mm/s}] = \frac{\text{Draw Step [LSB]} \times (0.00000274662)}{\text{Step Period [us]} \times 10^{-6}} \times 1000 \quad (4.1)$$

The overlap between laser spots depends on laser pulse frequency, laser scanner motor parameters, and laser spot size. The schematic of the overlap is shown in Figure 4.1 and its calculation formula is given.

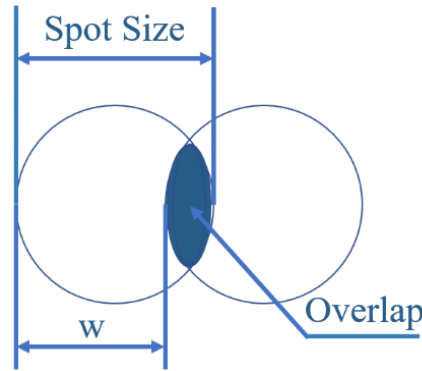


Figure 4.1. Overlap between laser spots

$$w = \frac{\text{Texturing Speed}}{\text{Laser Pulse Frequency}} \quad (4.2)$$

$$\text{Overlap} = \frac{\text{Spot size} - w}{\text{Spot Size}} \times 100 \quad (4.3)$$

Based on the overlap, different morphologies can be achieved (Figure 4.2): negative overlap which leads to separated spots and positive overlap which indicates line grooves.

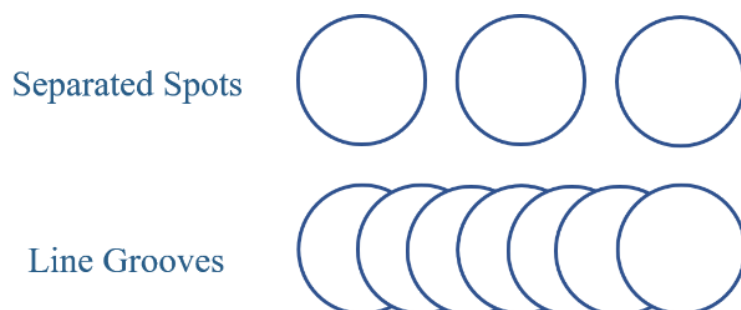


Figure 4.2. Different achievable morphologies depending on overlap

In this section, the effects of the laser parameters on the surface morphology and the optical characteristics of the surface are investigated.

4.1.1. Uniformity Across the Wafer

One of the important factors in determining the outcome of the proposed methods is the ability to use the method on full-scale wafers. In order to investigate this factor, two different sets are prepared. In Set 1, a full-size wafer is divided into 64 samples of $14\text{cm} \times 14\text{cm}$ and textured. In Set 2, a full-size wafer is textured at once. Laser parameters of these textured wafers are mentioned in Table 4.1. Figure 4.3 shows the optical and SEM images of selected samples from Set 1 and Figure 4.4 shows the optical and SEM image of the selected samples from Set 2.

Table 4.1. Laser parameters used for checking the uniformity across the wafer

| | <i>Frequency</i> | <i>Power</i> | <i>Pattern</i> | <i>Draw Step</i> | <i>Step Period</i> | <i>Line Spacing</i> | <i>Iteration</i> |
|-------|------------------|--------------|----------------|------------------|---------------------------------|---------------------------------|------------------|
| | <i>kHz</i> | <i>%</i> | | <i>LSB</i> | <i>μs</i> | <i>μm</i> | <i>#</i> |
| Set 1 | 55 | 80 | Criss-Cross | 25 | 120 | 100 | 1 |
| Set 2 | 55 | 80 | Line | 21 | 16 | 100 | 3 |

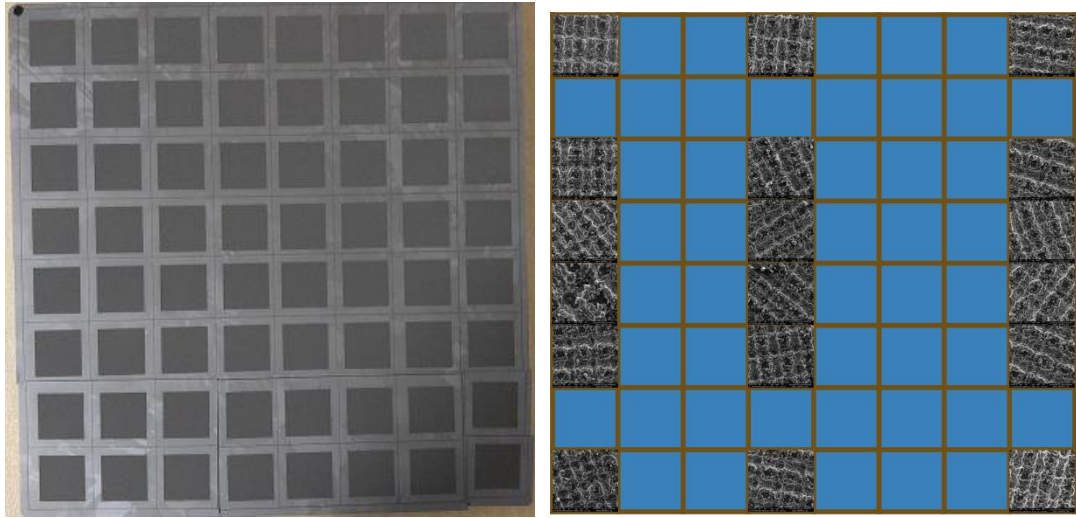


Figure 4.3. Optical and SEM images of a wafer divided into 64 samples and textured with laser parameters Set 1

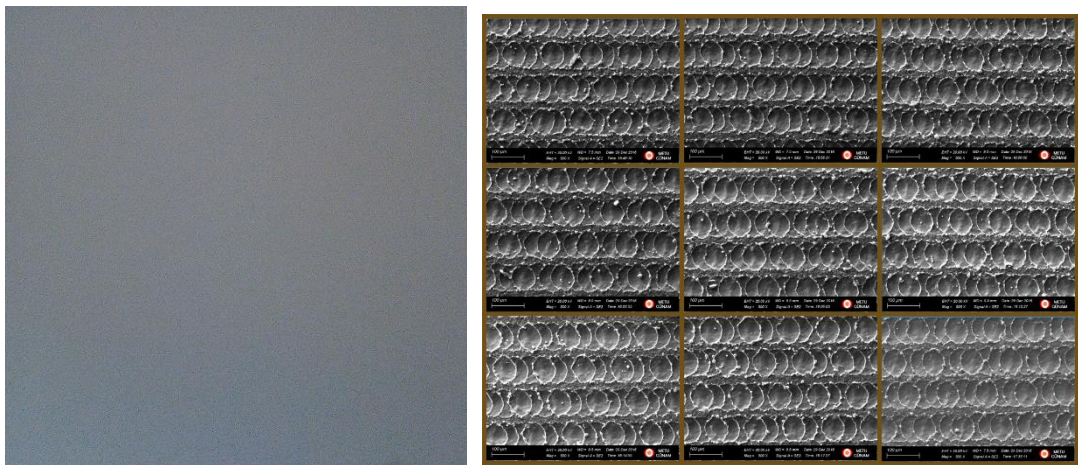


Figure 4.4. Optical and SEM images of the textured wafer with laser parameters of Set 2

The SEM images indicate that the texturing across the wafer is uniform; thus, it is possible to use this technique on the full-size wafer. However, we decided to work on smaller samples since its texturing is faster and more cost efficient at research scale. The SEM images of Set 1 with a bigger size are presented in Appendix D.

4.1.2. Effects of Draw Step and Step Period

Changing the laser scanner motor parameters, i.e. draw step and step period is the main factor which determines the final surface morphology. By changing the

mentioned parameters, separated pits or line groves structures can be achieved. The common laser parameters for this study are presented in Table 4.2 and the changing parameters and their resulting speed and overlap are presented in Table 4.3.

Table 4.2. Common parameters for investigating the effects of draw step and step period

| | | <i>Frequency</i> | <i>Power</i> | <i>Pattern</i> | <i>Line Spacing</i> | <i>Iteration</i> |
|--------------------|-----|------------------|--------------|----------------|---------------------|------------------|
| | | <i>kHz</i> | <i>%</i> | | <i>μm</i> | <i>#</i> |
| Common Parameter 1 | CP1 | 50 | 80 | Line | 100 | 1 |
| Common Parameter 2 | CP2 | 50 | 100 | Line | 100 | 1 |

Table 4.3. Changing parameters and their resulting speed and overlap

| | <i>Draw Step</i> | <i>Step Period</i> | <i>Common Parameters</i> | <i>Speed</i> | <i>Overlap</i> |
|-------|------------------|--------------------|--------------------------|--------------|----------------|
| | <i>LSB</i> | <i>μs</i> | | <i>mm/s</i> | <i>%</i> |
| Set 1 | 7 | 3 | CP1, CP2 | 6408 | -60 |
| Set 2 | 20 | 9 | CP1, CP2 | 6103 | -52 |
| Set 3 | 51 | 23 | CP1, CP2 | 6090 | -52 |
| Set 4 | 81 | 37 | CP1, CP2 | 6012 | -50 |
| Set 5 | 150 | 65 | CP1, CP2 | 6338 | -58 |

For the above-mentioned parameters, draw step and step period are selected in such a way that almost the same overlap and speed are achieved. Figure 4.5 shows the optical image of each set.

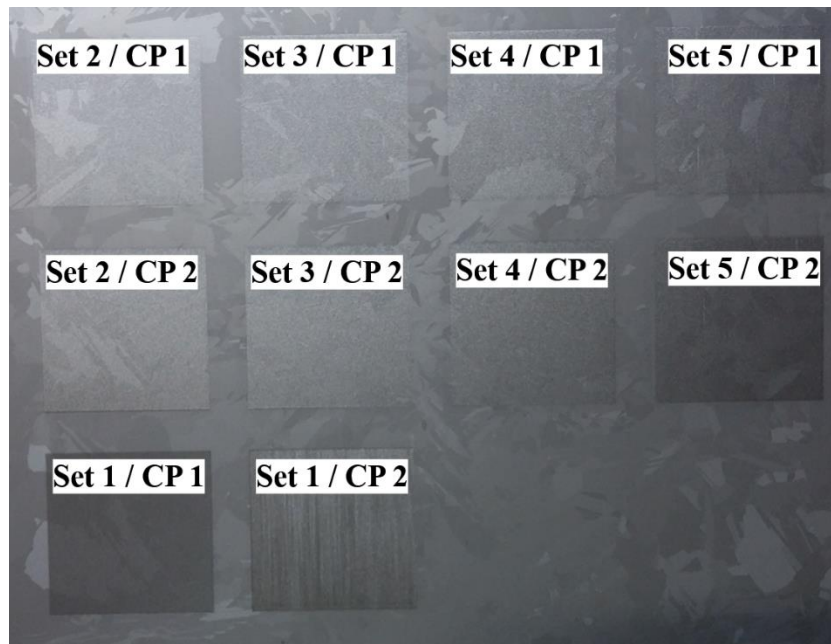


Figure 4.5. Optical image of textured wafer for investigating the effects of draw step and step period. Since the optical image above shows no favorable result in terms of reflection, other sets with common parameters of Table 4.4 and changing parameters of Table 4.5 are textured.

Table 4.4. Common parameters for investigating the effects of draw step and step period

| | | <i>Frequency</i> | <i>Power</i> | <i>Pattern</i> | <i>Line Spacing</i> | <i>Iteration</i> |
|--------------------|-----|------------------|--------------|----------------|---------------------|------------------|
| | | <i>kHz</i> | <i>%</i> | | <i>μm</i> | <i>#</i> |
| Common Parameter 1 | CP1 | 30 | 80 | Line | 100 | 1 |
| Common Parameter 2 | CP2 | 30 | 100 | Line | 100 | 1 |

Table 4.5. Changing parameters and their resulting speed and overlap

| | <i>Draw Step</i> | <i>Step Period</i> | <i>Common Parameter</i> | <i>Speed</i> | <i>Overlap</i> |
|-------|------------------|--------------------|-------------------------|--------------|----------------|
| | <i>LSB</i> | μs | | <i>mm/s</i> | <i>%</i> |
| Set 1 | 21 | 16 | CP1, CP2 | 3604 | -50 |
| Set 2 | 50 | 38 | CP1, CP2 | 3613 | -50 |
| Set 3 | 80 | 61 | CP1, CP2 | 3602 | -50 |
| Set 4 | 150 | 114 | CP1, CP2 | 3613 | -50 |

The optical image of this set is shown in Figure 4.6 which shows the more favorable effects on the samples. In order to investigate further, the SEM images of sets with CP2 are taken and shown in Figure 4.7. In addition, reflection curves of these sets are shown in Figure 4.8.

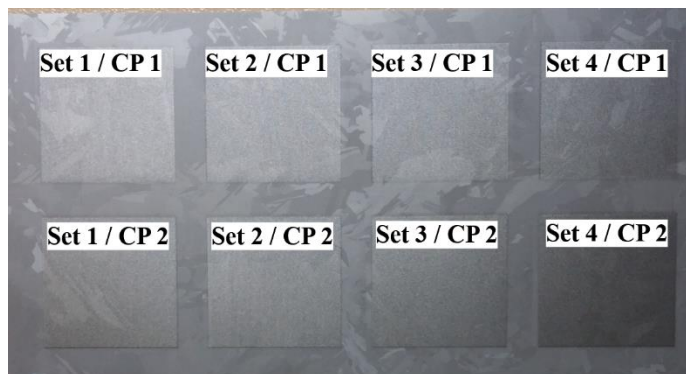


Figure 4.6. Optical image of textured sample for investigating the effects of draw step and step period

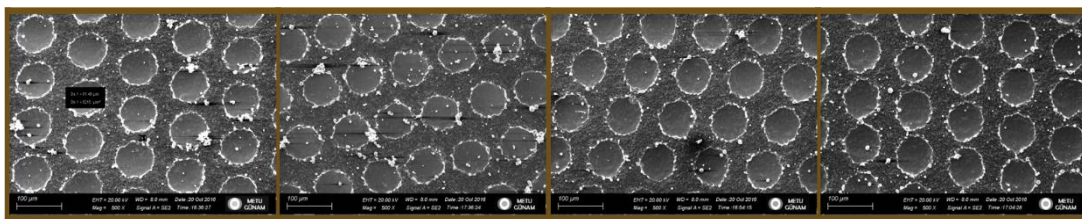


Figure 4.7. SEM images of textured wafer to investigate the effects of draw step and step period CP2

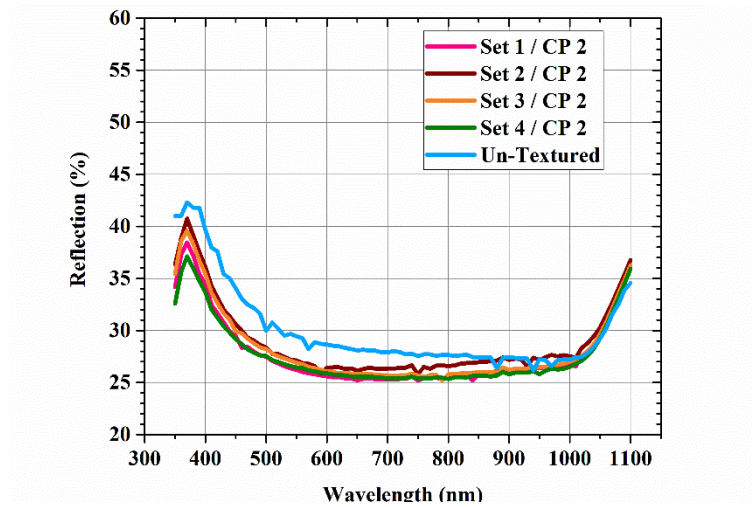


Figure 4.8. Reflection curves of all sets with CP2

These experiments are conducted to achieve separated laser spots. As it is seen in the figures, since these structures are really shallow and the reflection curves do not show notable improvements, either the number of the laser scans must be increased to obtain deeper structures, which will be discussed in the next section, or another morphology regarding the laser scanner motor parameter must be used.

To obtain different morphologies, draw step and step period are selected to have positive overlap. Table 4.6 shows the common parameters and Table 4.7 shows the changing parameters.

Table 4.6. Common parameters of effects of draw step and step period

| | <i>Frequency</i> | <i>Power</i> | <i>Pattern</i> | <i>Line Spacing</i> | <i>Iteration</i> |
|------------------|------------------|--------------|----------------|---------------------|------------------|
| | <i>kHz</i> | <i>%</i> | | <i>μm</i> | <i>#</i> |
| Common Parameter | 30 | 100 | Line | 100 | 1 |

Table 4.7. Changing parameters of effects of draw step and step period

| | <i>Draw Step</i> | <i>Step Period</i> | <i>Speed</i> | <i>Overlap</i> |
|-------|------------------|--------------------|--------------|----------------|
| | <i>LSB</i> | μs | <i>mm/s</i> | <i>%</i> |
| Set 1 | 21 | 16 | 3604 | -50 |
| Set 2 | 25 | 120 | 572 | +76 |

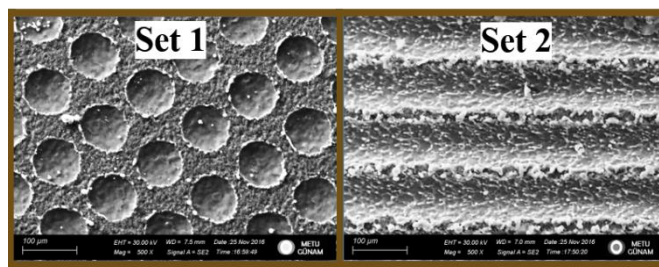


Figure 4.9. SEM images of Set 1 and Set 2

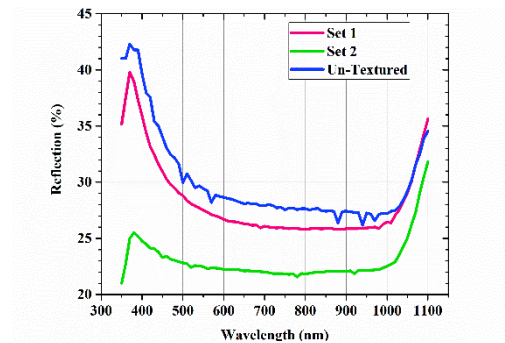


Figure 4.10. Reflection curves of Set 1 and Set 2

The figures above indicate that the laser scanner motor parameters have notable effects on the resulting surface morphologies. These parameters determine the final shape of the sample’s surface from the separated laser spots to the line grooves. In addition, these parameters have a huge impact on the overall speed of texturing.

4.1.3. Effects of Pattern and Laser Line Spacing

By changing the pattern and laser line spacing, different morphologies as shown in the figures below can be achieved. The texturing purpose is to increase the absorption by

introducing roughness at the surface; therefore, one criterion for texturing is reducing the flat surface (untextured) area which can be optimized by changing the laser frequency, the laser scanner motor parameters, the pattern, and the laser line spacing.

The common laser parameters for determining the effects of pattern and laser line spacing are shown in Table 4.8 and the specific parameters are shown in Table 4.9. Note that these experiments are done on unpolished wafers without the saw damage etching process.

Table 4.8. *Common laser parameters for determining the effect of pattern and laser line spacing*

| | | <i>Frequency</i> | <i>Power</i> | <i>Draw Step</i> | <i>Step Period</i> | <i>Iteration</i> |
|---------------------|-----|------------------|--------------|------------------|--------------------|------------------|
| | | <i>kHz</i> | <i>%</i> | <i>LSB</i> | <i>μs</i> | <i>#</i> |
| Common Parameters 1 | CP1 | 30 | 100 | 21 | 16 | 1 |
| Common Parameters 2 | CP2 | 55 | 100 | 25 | 120 | 1 |

Table 4.9. *Changing parameter of pattern and line spacing*

| | <i>Pattern</i> | <i>Line Spacing</i> | <i>Common Parameters</i> |
|-------|----------------|---------------------|--------------------------|
| | <i>μm</i> | | |
| Set 1 | Line | 100 | CP1 |
| Set 2 | Line | 150 | CP1 |
| Set 3 | Line | 200 | CP1 |
| Set 4 | Criss-Cross | 75 | CP2 |
| Set 5 | Criss-Cross | 100 | CP2 |
| Set 6 | Criss-Cross | 125 | CP2 |

The top view SEM images from CP1 are shown in Figure 4.11 and the top view and cross-section view SEM images from CP2 are shown in Figure 4.12.

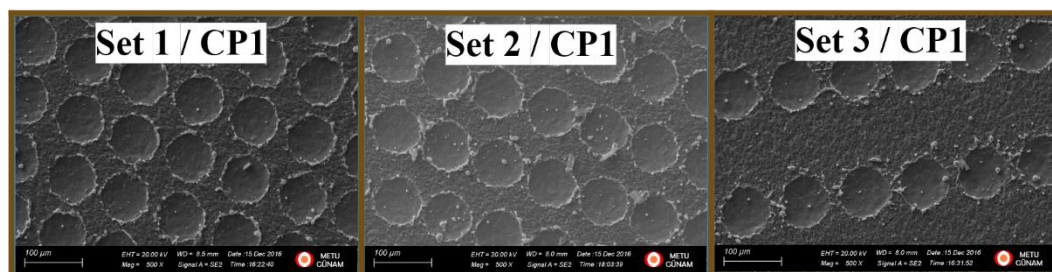


Figure 4.11. Top view SEM images from textured samples with line pattern and CP1

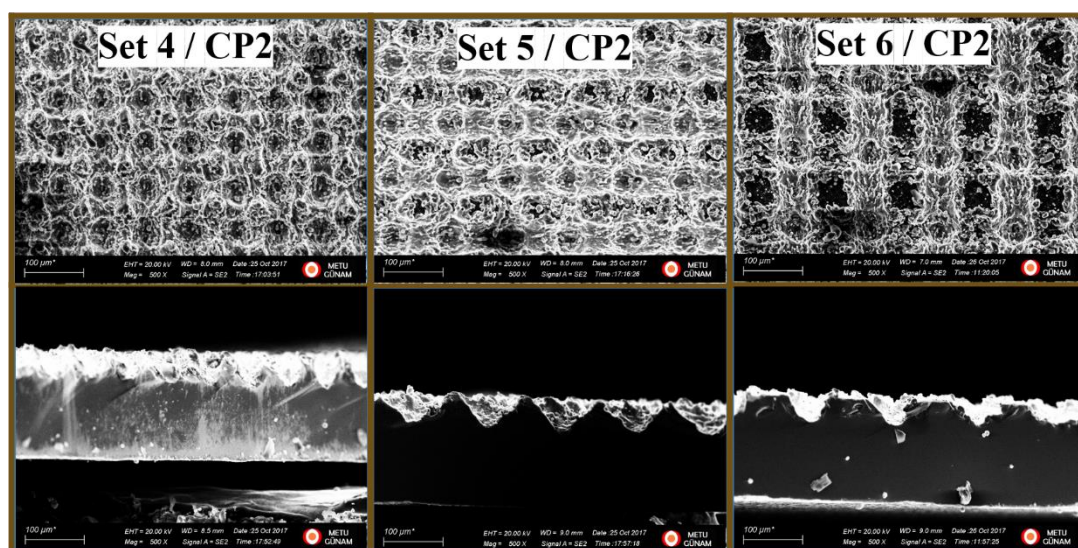


Figure 4.12. Top view and cross-section view SEM images from textured samples with criss-cross pattern and CP2

4.1.4. Effects of Laser Pulse Frequency

In this section, the effects of the laser pulse frequency on the surface morphology and reflection are investigated. To determine these effects, all parameters are kept constant and only the laser pulse frequency is changed. Table 4.10 shows the constant parameters of laser texturing and Table 4.11 shows the selected laser pulse frequency.

Table 4.10. Common laser parameters for determining the effects of laser pulse frequency on surface morphology and reflection

| | | <i>Power</i> | <i>Pattern</i> | <i>Draw Step</i> | <i>Step Period</i> | <i>Line Spacing</i> | <i>Iteration</i> |
|--------------------|-----|--------------|----------------|------------------|--------------------|---------------------|------------------|
| | | % | | LSB | μs | μm | # |
| Common Parameter 1 | CP1 | 100 | Line | 25 | 120 | 100 | 1 |
| Common Parameter 2 | CP2 | 100 | Criss Cross | 25 | 120 | 150 | 3 |

Table 4.11. Frequency changes in determining the effects of laser pulse frequency on surface morphology and reflection

| | <i>Frequency</i> |
|-------|------------------|
| | <i>kHz</i> |
| Set 1 | 30 |
| Set 2 | 55 |
| Set 3 | 80 |

Figure 4.13 shows the SEM image of the surface morphologies obtained from laser texturing with the parameters of Table 4.2 and Table 4.3. In addition, Figure 4.14 shows the reflection of the samples.

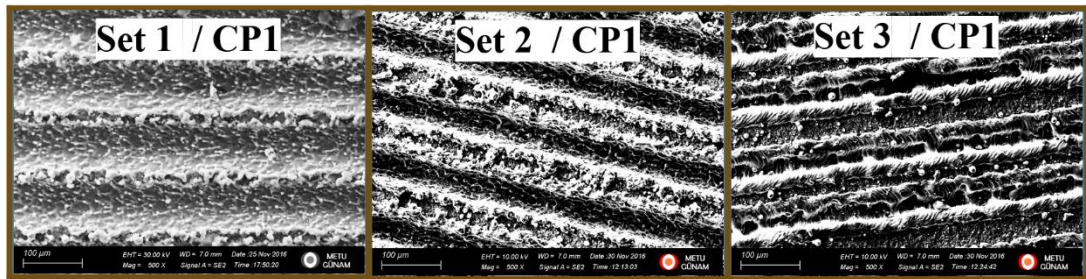


Figure 4.13. SEM images of effects of the laser pulse frequency of CP1

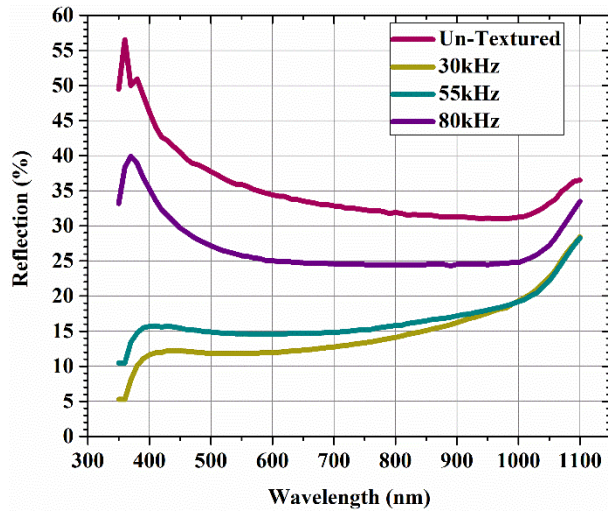


Figure 4.14. Reflection curves of effects of the laser pulse frequency of CP1

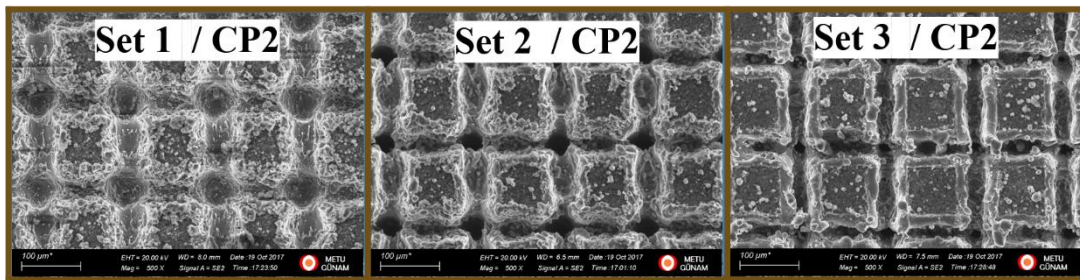


Figure 4.15. SEM images of effects of the laser pulse frequency of CP2

According to the figures above, increasing the frequency makes the texturing more intense and increases the spot size.

4.1.5. Effects of Laser Power

In order to find out the effects of changing the power on the samples, the samples are textured with the common laser parameters of Table 4.12 and the specific laser powers of Table 4.13.

Table 4.12. Common laser parameters for determining the effect of laser power

| | | <i>Frequency</i> | <i>Pattern</i> | <i>Draw Step</i> | <i>Step Period</i> | <i>Line Spacing</i> | <i>Iteration</i> |
|---------------------|-----|------------------|----------------|------------------|--------------------|---------------------|------------------|
| | | <i>kHz</i> | | <i>LSB</i> | <i>μs</i> | <i>μm</i> | <i>#</i> |
| Common Parameters 1 | CP1 | 55 | Criss-Cross | 25 | 120 | 75 | 1 |
| Common Parameters 2 | CP2 | 55 | Criss-Cross | 25 | 120 | 100 | 1 |
| Common Parameters 3 | CP3 | 55 | Criss-Cross | 25 | 120 | 150 | 3 |

Table 4.13. Changing laser parameters for determining the effect of laser power

| <i>Power</i> | |
|--------------|-----|
| <i>%</i> | |
| Set 1 | 80 |
| Set 2 | 100 |

The top view and cross-section view of SEM images for CP1, CP2, and CP3 are shown in Figure 4.16, Figure 4.17, and Figure 4.18 respectively.

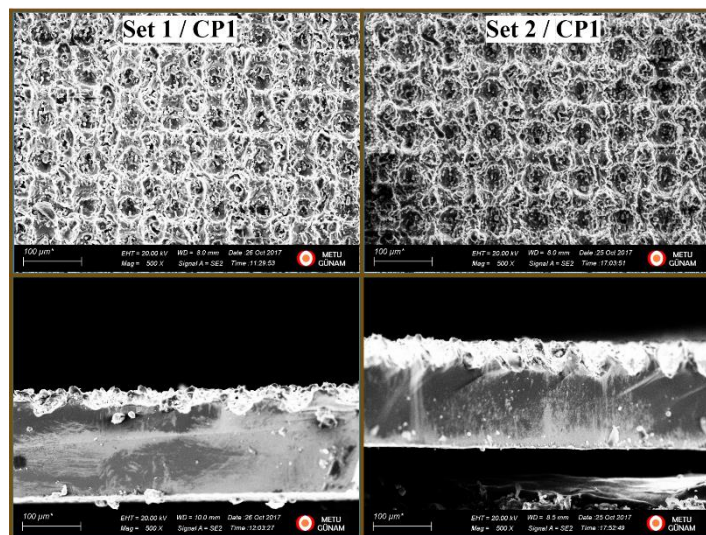


Figure 4.16. Top view and cross-section view SEM images from textured samples with CP1

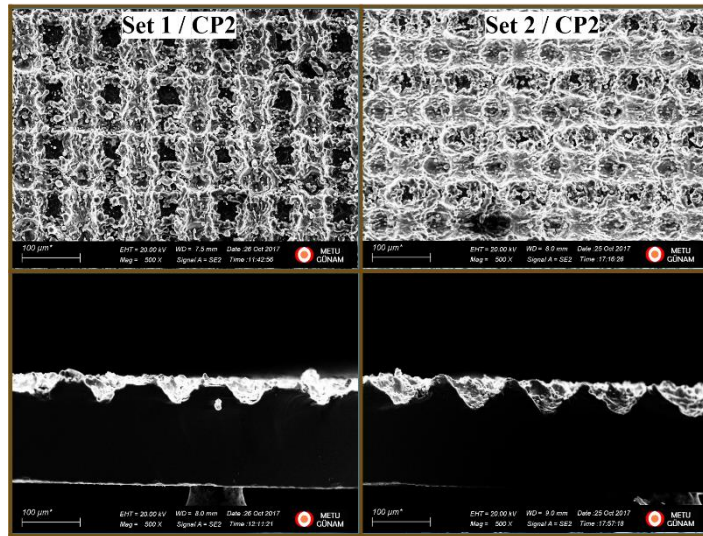


Figure 4.17. Top view and cross-section view SEM images from textured samples with CP2

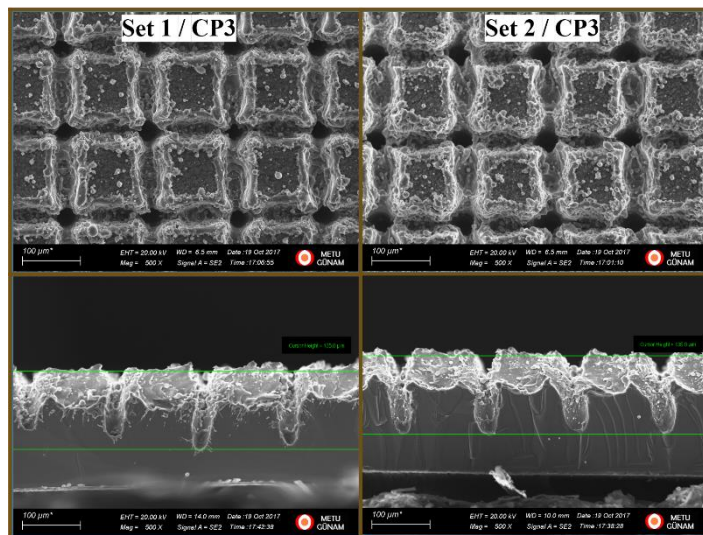


Figure 4.18. Top view and cross-section view SEM images from textured samples with CP3

The comparison between the morphologies obtained from different laser powers indicates that increasing the power leads to deeper morphologies.

4.1.6. Effects of Iteration

The iteration of texturing, which is the number of line scans, can affect the depth of the surface morphology. The effects of the iteration are investigated on two different

laser textured morphologies. The separated laser spots are obtained using the common parameters of Table 4.14 and the changing parameters of Table 4.15.

Table 4.14. *Common laser texturing parameters of effects of iteration*

| | | <i>Frequency</i> | <i>Power</i> | <i>Pattern</i> | <i>Draw Step</i> | <i>Step Period</i> | <i>Line Spacing</i> |
|--------------------|-----|------------------|--------------|----------------|------------------|--------------------|---------------------|
| | | <i>kHz</i> | <i>%</i> | | <i>LSB</i> | <i>μs</i> | <i>μm</i> |
| Common Parameter 1 | CP1 | 30 | 100 | Line | 21 | 16 | 100 |
| Common Parameter 2 | CP2 | 30 | 100 | Line | 25 | 120 | 100 |
| Common Parameter 3 | CP3 | 55 | 100 | Criss-Cross | 25 | 120 | 100 |

Table 4.15. *Changing laser texturing parameters of effects of iteration*

| | <i>Iteration</i> | <i>Common Parameters</i> |
|-------|------------------|--------------------------|
| | <i>#</i> | |
| Set 1 | 1 | CP1, CP2, CP3 |
| Set 2 | 2 | CP1, CP2, CP3 |
| Set 3 | 3 | CP1, CP2, CP3 |
| Set 4 | 5 | CP1, CP2 |

The optical images of the sets with CP1 and CP2 are shown in Figure 4.19. The SEM images of the top view from sets with CP1 and CP2 are shown in Figure 4.20 and Figure 4.21 respectively. In addition, the weighted reflections of these samples are shown in Figure 4.22.



Figure 4.19. Optical image of sets of CP1 and CP2

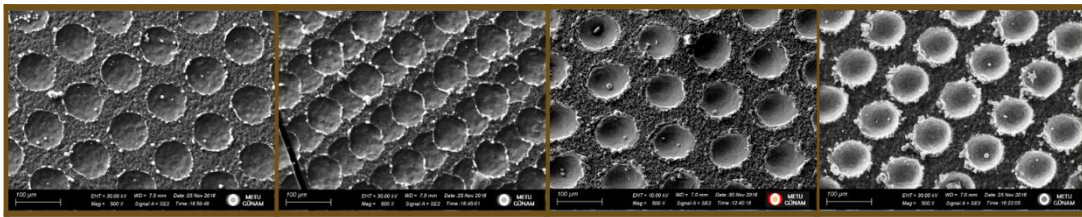


Figure 4.20. SEM images of sets of CP1

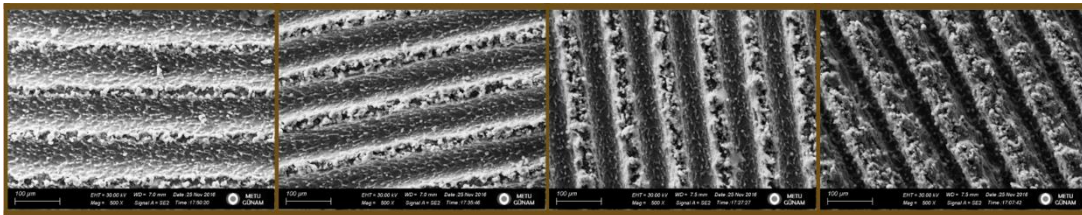


Figure 4.21. SEM images of sets of CP2

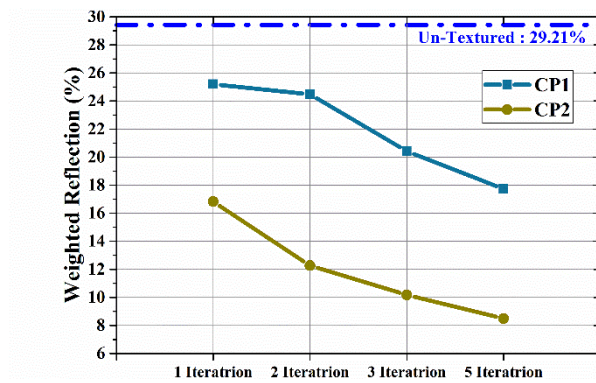


Figure 4.22. Weighted reflection of sets of CP1 and CP2

As it can be seen in the top view SEM images, the depth of the structure is increased. Another fact is that the laser setup does not necessarily start texturing at the same point; thus, there is a mismatch between the laser spots in every iteration at times. To check the depth of the structure, the SEM images from the top view and cross-section view from sets with CP3 are shown in Figure 4.23 and Figure 4.24 respectively.

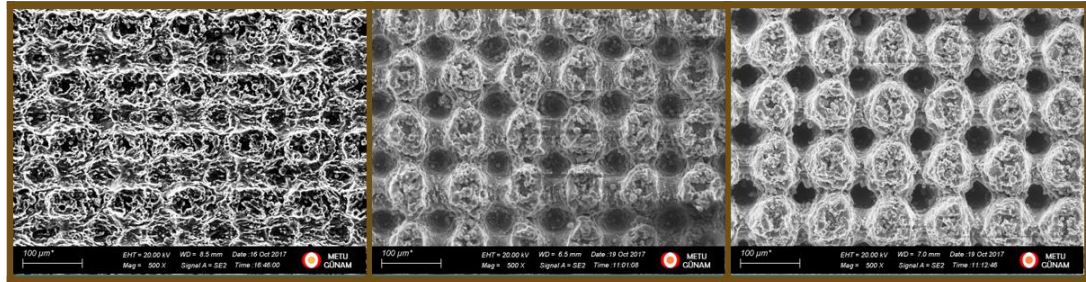


Figure 4.23. Top view SEM images of sets of CP3

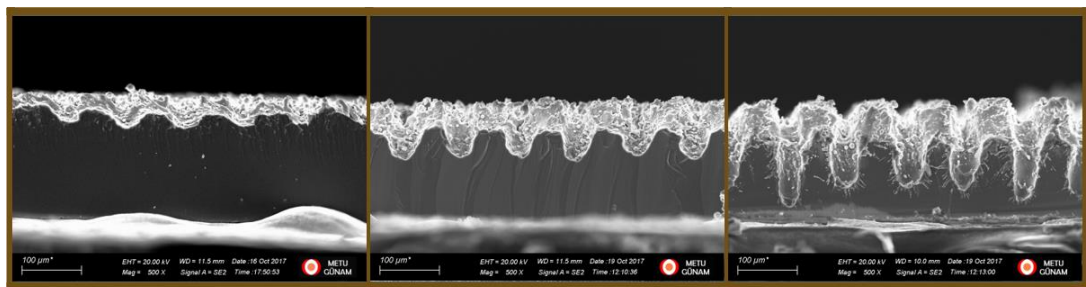


Figure 4.24. Cross section view SEM images of sets of CP3

4.2. Post-Texture Cleaning

To have comprehensive research on the effects of post-texture cleaning of the surface morphology and reflection, physical treatment without any chemical solution is used at first. This physical treatment is done in an ultrasonic bath for 5 minutes. Another chemical treatment using a KOH solution is done once using the room temperature and the dilute KOH solution (1% concentration) with different durations. The laser parameters of the selected samples are shown in Table 4.16. Figure 4.25 shows the top view (top) and the cross-section view (bottom) of the SEM images of as-textured, physically treated, and chemically treated with dilute KOH samples of CP1 with duration of 300 sec and Figure 4.26 shows the SEM images of CP2. In addition, Figure

4.37 compares the weighted reflection of all treated samples. The top view and cross-section view of the SEM images of all sets are presented in Appendix E.

Table 4.16. Common laser texturing parameters for investigating post-texture cleaning

| | | Frequency | Power | Pattern | Draw Step | Step Period | Line Spacing | Iteration |
|--------------------|-----|------------|----------|-------------|------------|-------------|--------------|-----------|
| | | <i>kHz</i> | <i>%</i> | | <i>LSB</i> | <i>μs</i> | <i>μm</i> | <i>#</i> |
| Common Parameter 1 | CP1 | 55 | 100 | Criss-Cross | 25 | 120 | 100 | 2 |
| Common Parameter 2 | CP2 | 55 | 100 | Criss-Cross | 25 | 120 | 100 | 3 |

Table 4.17. Changing laser texturing parameters for investigating post-texture cleaning

| | Cleaning Type | Concentration | Temperature | Duration |
|-------|---------------|---------------|------------------|------------|
| | | <i>%</i> | <i>°C</i> | <i>sec</i> |
| Set 1 | N/A | N/A | N/A | N/A |
| Set 2 | Physical | N/A | Room Temperature | 300 |
| Set 3 | Chemical | 1 | Room Temperature | 300 |

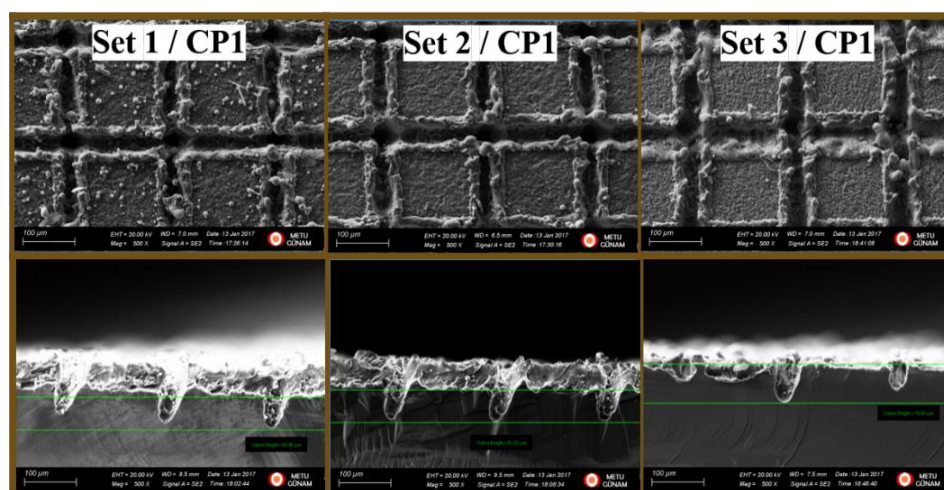


Figure 4.25. SEM images of CP1

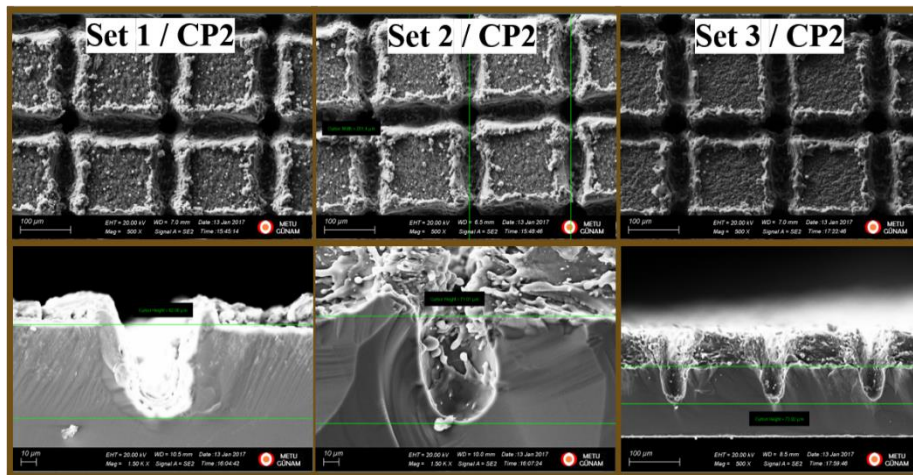


Figure 4.26. SEM images of CP2

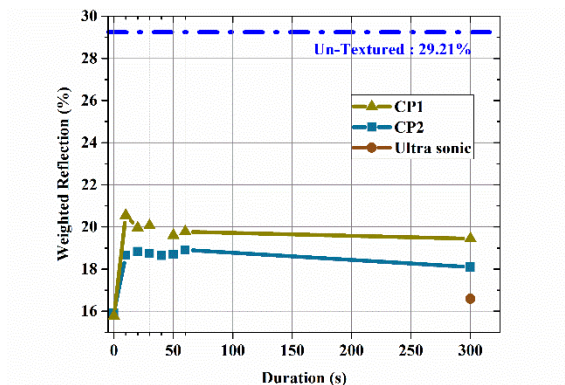


Figure 4.27. Weighted reflection of CP1 and CP2

Based on the SEM images of physical treatment and dilute KOH solution, these two post-texture cleaning processes are not efficient enough. The weighted reflection of these samples also confirms this conclusion. Thus, the KOH solution with high concentration and high temperature is used. It is important to note that KOH solution at high temperature and concentration is an isotropic etching solution. The laser texturing parameter for this experiment is shown in Table 4.18. The post-texture cleaning parameters are shown in Table 4.19.

Table 4.18. Laser parameters for determining effect of high concentration temperature KOH solution

| | <i>Frequency</i> | <i>Power</i> | <i>Pattern</i> | <i>Draw Step</i> | <i>Step Period</i> | <i>Line Spacing</i> | <i>Iteration</i> |
|------------------|------------------|--------------|----------------|------------------|--------------------|---------------------|------------------|
| | <i>kHz</i> | <i>%</i> | | <i>LSB</i> | <i>μs</i> | <i>μm</i> | <i>#</i> |
| Common Parameter | 30 | 100 | Criss-Cross | 25 | 120 | 75 | 1 |

Table 4.19. Post-texture cleaning parameter using KOH solution

| KOH Concentrations | Temperatures | Post-texture Cleaning Durations |
|--------------------|--------------|---------------------------------|
| 2% | 60°C | 30 sec |
| 4% | | 1 min |
| 8% | | 2 min |
| 16% | 80°C | 4 min |
| 24% | | 6 min |
| 32% | | 8 min |

The top view SEM images of selected samples are shown for the temperatures of 60°C and 80°C in Figure 4.28 and Figure 4.29 respectively.

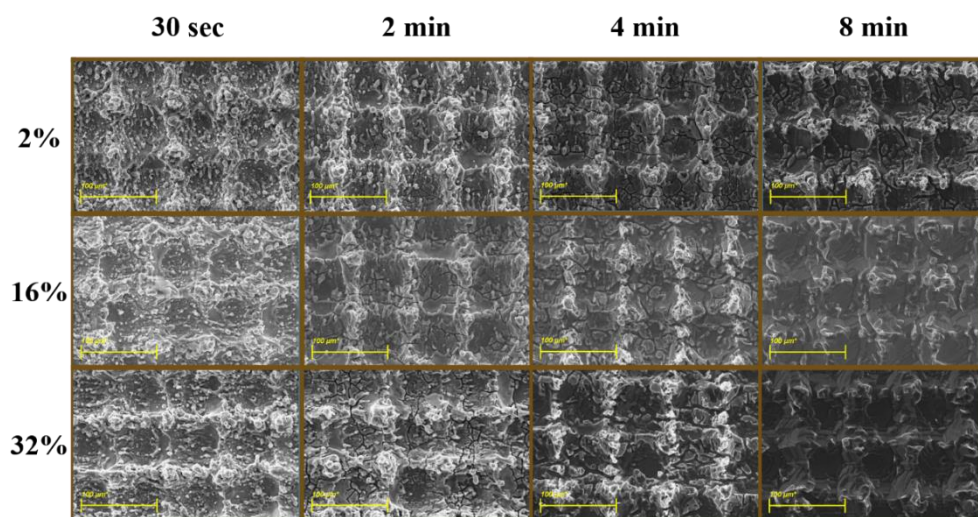


Figure 4.28. Top view SEM images of samples with different concentration and duration at 60°C

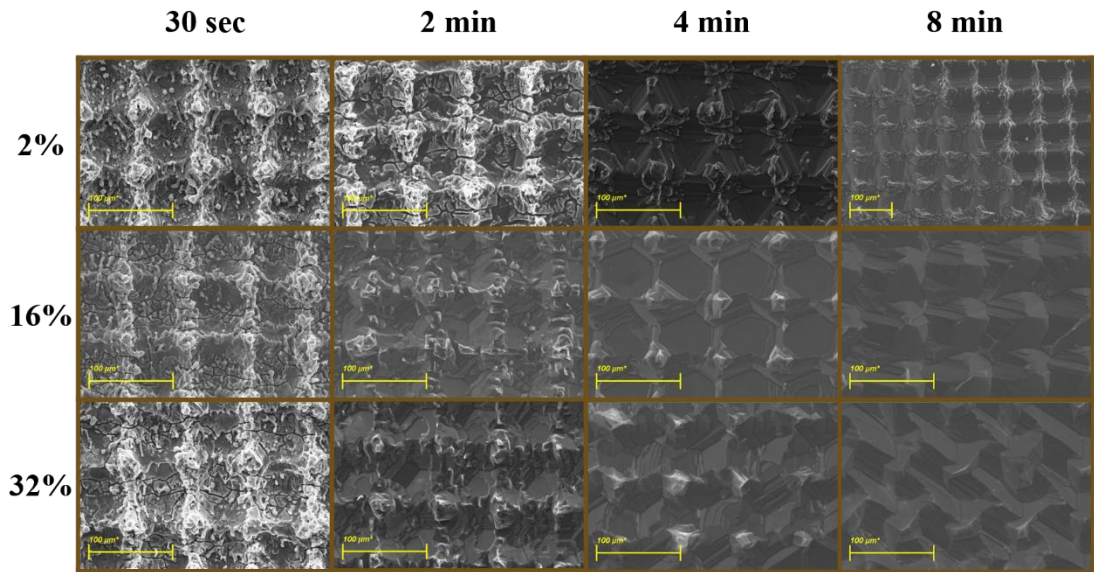


Figure 4.29. Top view SEM images of samples with different post-texture cleaning concentration and duration at 80°C

In addition to the top view of the SEM images, the SEM images with 45° tilt are also considered. The 45° tilted SEM images are shown for the temperatures of 60°C and 80°C in Figure 4.30 and Figure 4.31 respectively.

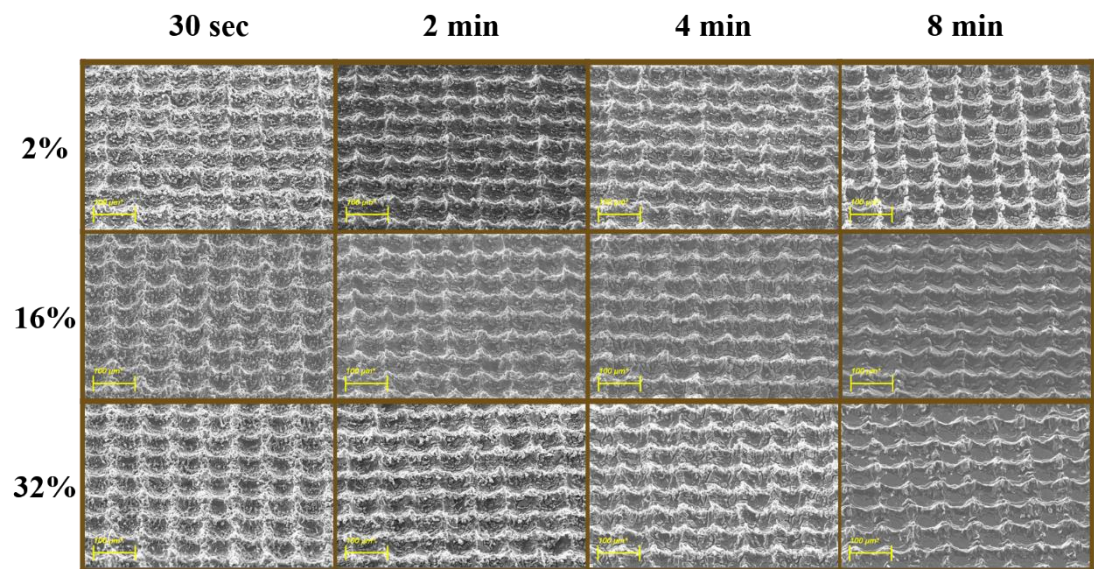


Figure 4.30. 45° tilted view SEM images of samples with different post-texture cleaning concentration and duration at 60°C

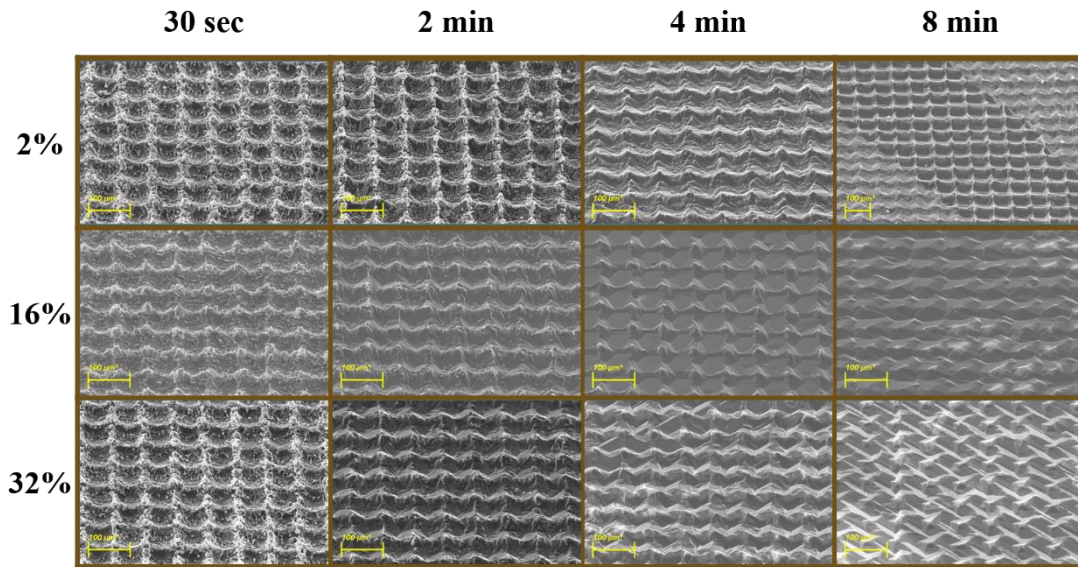


Figure 4.31. 45° tilted view SEM images of samples with different post-texture cleaning concentration and duration at 80°C

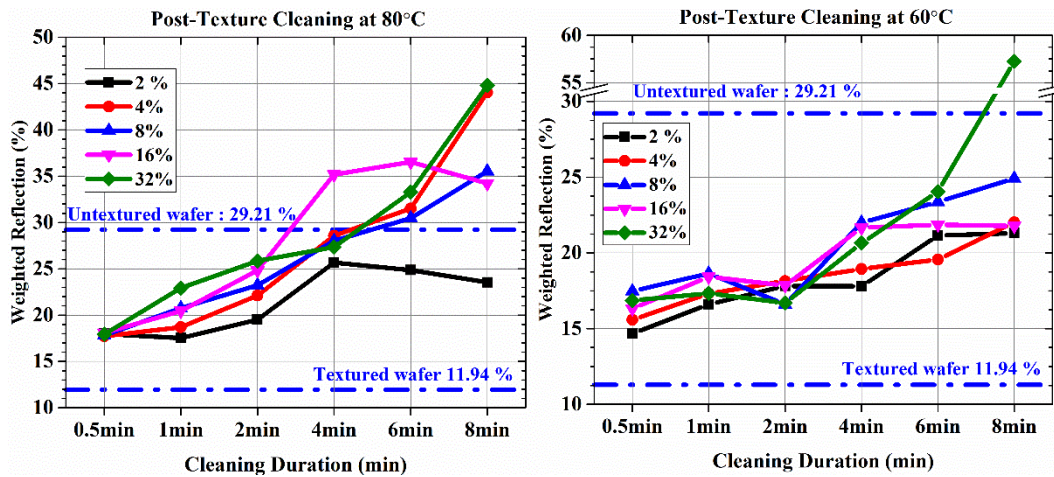


Figure 4.32. Weighted reflection of the sample with different post-texture cleaning concentrations and durations at (left) 80°C and (right) 60°C

To have a closer look at the reflection of the samples with the lowest weighted reflection, the reflection curves of samples that are post-texture cleaned using KOH solution with concentration of 2% and 4% with durations of 0.5 min, 1 min, and 2 min are illustrated in Figure 4.33 for both temperatures of 60°C (right) and 80°C (left).

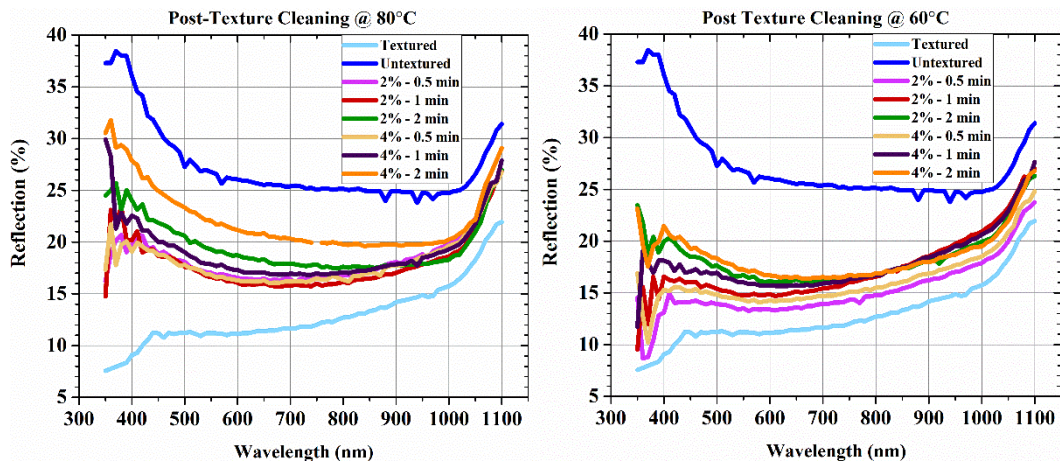


Figure 4.33. Reflection curves of the sample with relatively low weighted reflection at (left) 80°C and (right) 60°C

The SEM images and the weighted reflection of the samples show that the surface's structure extremely depends on the post-texture cleaning step. In general, using an intense post-texture cleaning step makes the surface smoother and thus, increases the weighted reflection. It is important to note that choosing the optimum parameters depends on the application.

4.3. Effects of Anti Reflection Coating and Passivation Layer on implied Open Circuit Voltage and Reflection

In other to determine the best possible scenario of the proposed technique without interfering with other effective parameters, the best case for optical properties and electrical properties of samples are determined by depositing the ARC layer and the passivation layer individually.

In this study, monocrystalline silicon wafers are used since the multi-crystalline silicon wafers have a low lifetime due to the effect of grain boundaries. The common laser parameters are shown in Table 4.20. In addition, three different specific laser parameters are selected for this study and samples with each laser parameter are post-texture cleaned with KOH solution with 20% concentration at 80°C with different durations. These specific parameters are shown in Table 4.21.

Table 4.20. Common parameters for investigating effects of the passivation layer

| | <i>Pattern</i> | <i>Draw Step</i> | <i>Step Period</i> | <i>Line Spacing</i> | <i>Iteration</i> |
|-------------------|----------------|------------------|--------------------|---------------------|------------------|
| | | <i>LSB</i> | μs | μm | <i>#</i> |
| Common Parameters | Criss-Cross | 25 | 120 | 75 | 1 |

Table 4.21. Changing parameters for investigating effects of the passivation layer

| | <i>Frequency</i> | <i>Power</i> | <i>Post-texture cleaning durations</i> |
|-------|------------------|--------------|--|
| | <i>kHz</i> | <i>%</i> | <i>min</i> |
| Set 1 | 30 | 100 | 0.5, 1, 2, 4 |
| Set 2 | 55 | 100 | 0.5, 1, 2, 4 |
| Set 3 | 55 | 80 | 0.5, 1, 2, 4 |

In order to enhance the electrical properties, thin alumina (Al_2O_3) as a passivation layer, is deposited on the samples using atomic layer deposition (ALD) system. The passivation layer is deposited on both sides since both sides' surfaces contribute to the recombination processes. After the deposition, the samples are annealed at $435^\circ C$ for 30min. To determine the thickness of the Al_2O_3 layer, an untextured sample is also placed in the ALD chamber and the thickness is measured using scanning ellipsometer by Cauchy with Urbach tail fitting at an incident angle of 60° from 1.23eV to 5eV. The Al_2O_3 is measured as 14.39nm.

The top view and the 45° tilted view of the SEM image for an as-texture and post-texture cleaned sample for 2min and 4min are shown for Set 1 and Set 2 in Figure 4.34 and Figure 4.35 respectively. In addition, Figure 4.36 shows the implied V_{oc} (left) and the weighted reflection (right) of all sets.

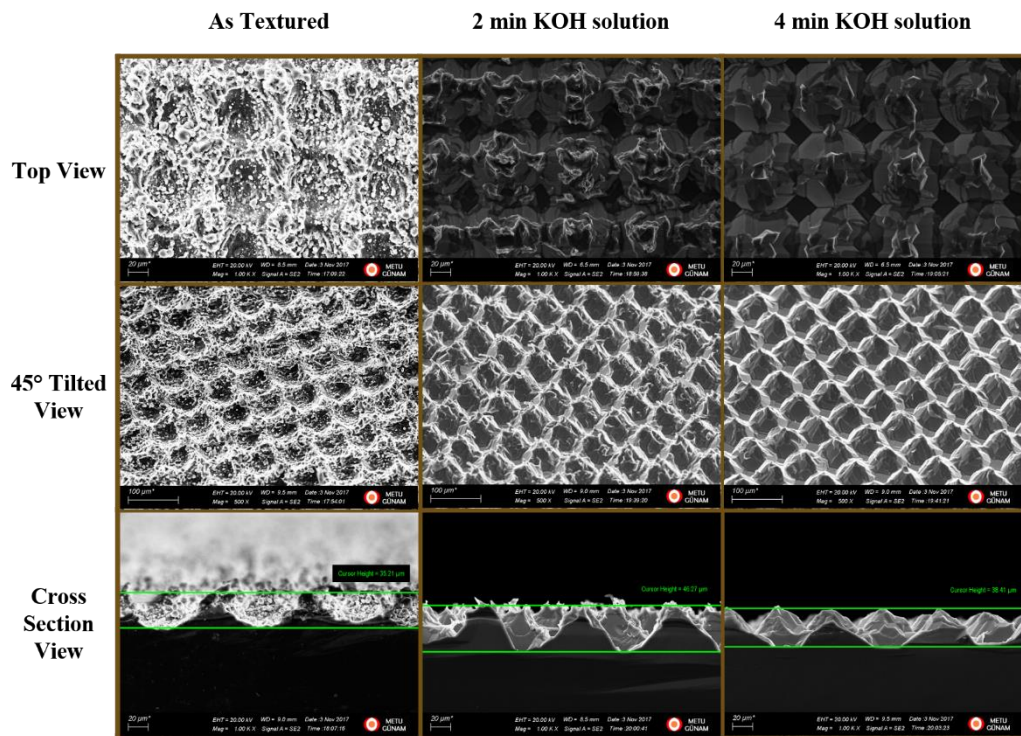


Figure 4.34. SEM images of Set 1, prepared for depositing the passivation layer

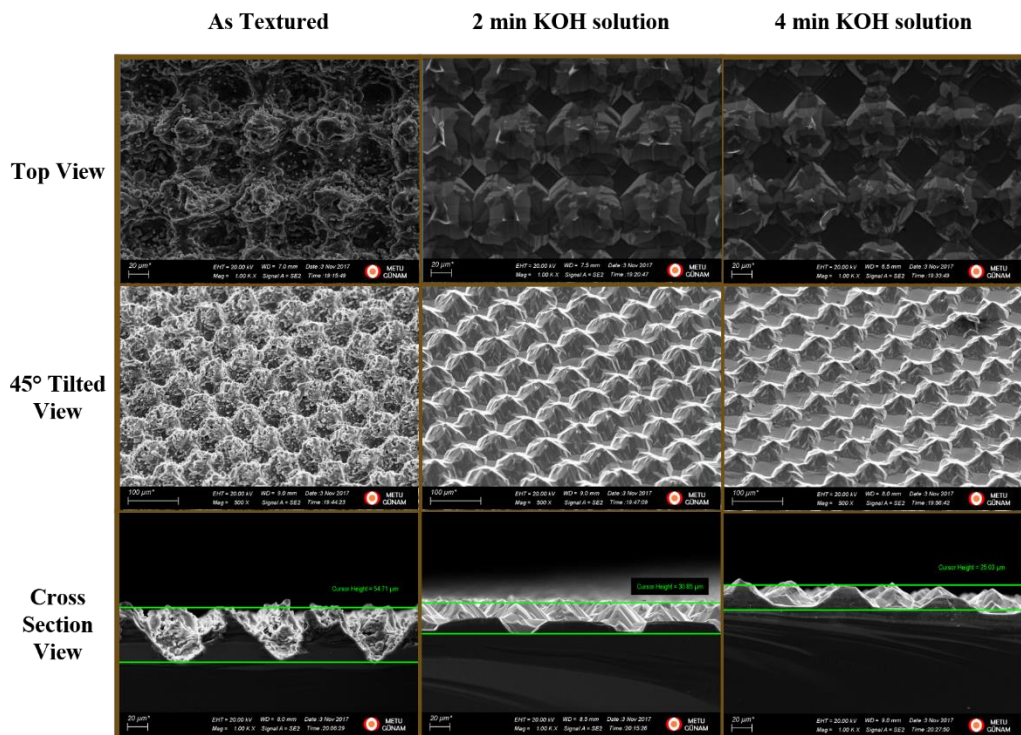


Figure 4.35. SEM images of Set 2, prepared for depositing the passivation layer

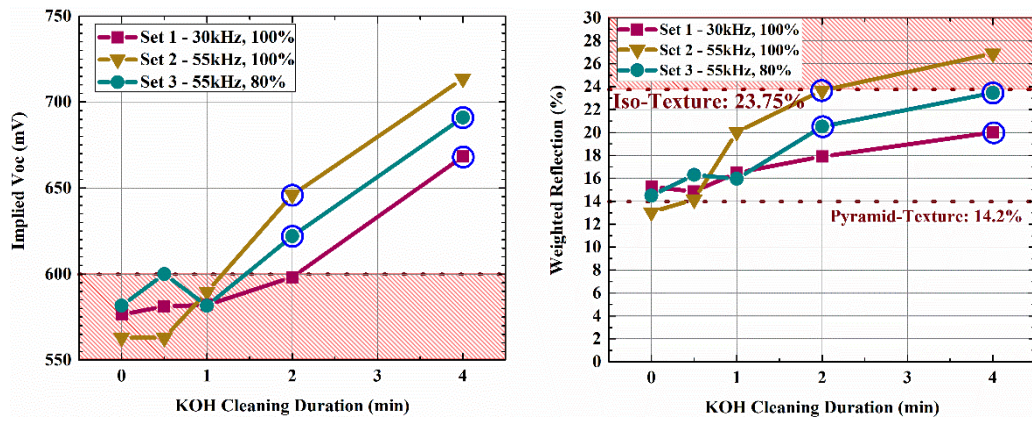


Figure 4.36. Implied Voc (left) and weighted reflection (right) of samples with the passivation layer. The SEM images of Set 3 and post-texture cleaned samples of Set 1 and Set 2 for 0.5min and 1min are presented in Appendix F.

Based on the weighted reflection and the implied V_{oc} results, 4 samples with high iV_{oc} and reasonable weighted reflection are selected and marked with red circle in Figure 4.36 for investigating the effects of the anti-reflection coating layer. The common laser parameters are the same as the previous part while the changing parameters are given in Table 4.22.

Table 4.22. Laser texturing and post-texture cleaning parameters for investigating effect of ARC layer

| | Frequency | Power | Post-texture cleaning duration | ARC Thickness |
|-------|-----------|-------|--------------------------------|---------------|
| | kHz | % | min | nm |
| Set 1 | 30 | 100 | 4 | 65, 75, 85 |
| Set 2 | 55 | 100 | 2 | 65, 75, 85 |
| Set 3 | 55 | 80 | 2 | 65, 75, 85 |
| Set 4 | 55 | 80 | 4 | 65, 75, 85 |

The optical image of the samples is shown in Figure 4.37. In this figure, the color difference between the samples is clear which indicates the difference in the Si_3N_4 thickness.

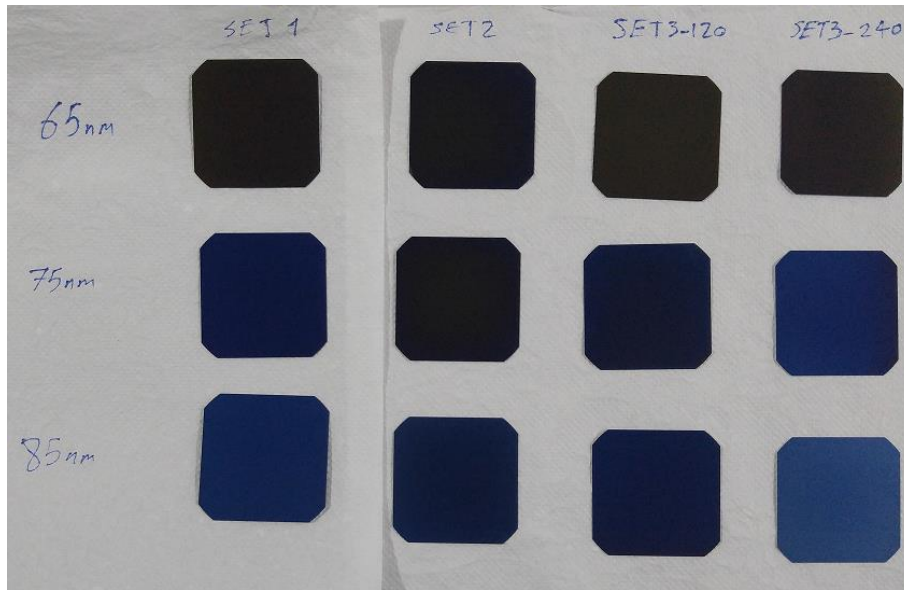


Figure 4.37. Optical image of samples with different ARC thicknesses

Figure 4.38 illustrates the weighted reflection of all samples (left) and the reflection curves of Set 2 with 2min KOH solution (right).

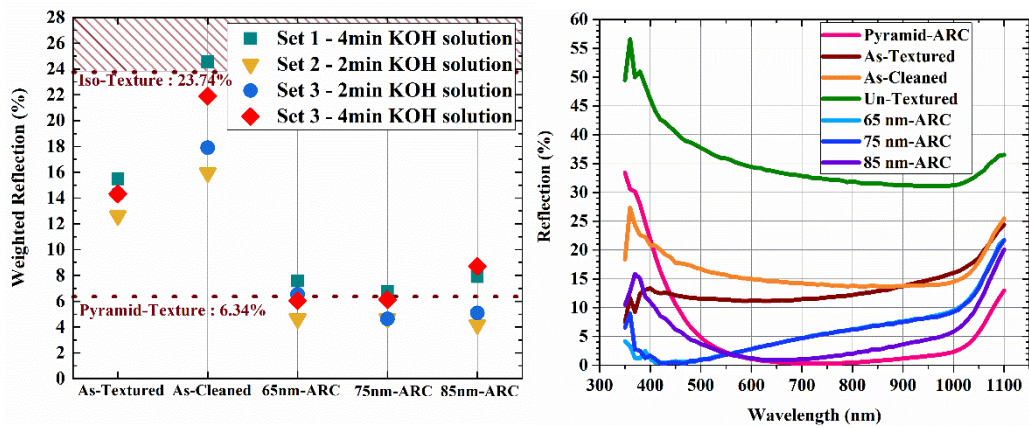


Figure 4.38. Weighted reflection of all samples (left) and reflection curve of Set 2 with 2min KOH solution

These results indicate that the weighted reflection as low as 4.18% and the iV_{oc} as high as 692 can be achieved. However, as we noted before, the acceptable laser and post-texture cleaning pair parameters are the ones that have a moderate weighted reflection and a moderate iV_{oc} since the roughness increases the absorption and decreases iV_{oc} due to the recombinations at the surface.

4.4. Solar Cell Performance

The goal of this study is to fabricate an efficient solar cell from multi-crystalline wafers by enhancing the surface's light absorption. For the solar cell fabrication, 3 samples with the size of 4cm × 4cm within the full-size wafer are textured with the laser setup since it is more favorable to process the full-size wafer through all solar cell fabrication steps. The optical image of the final solar cell is shown in Figure 4.39.

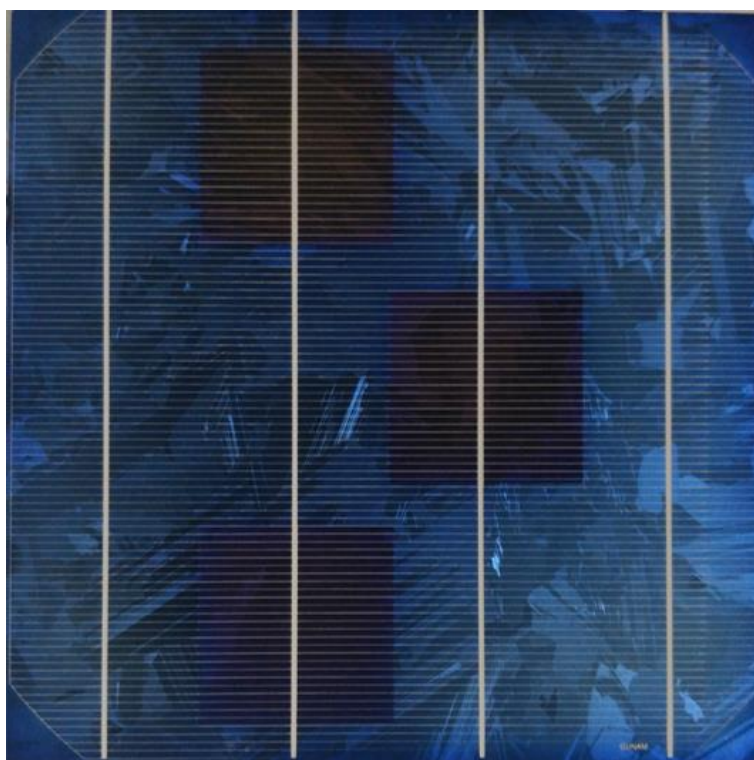


Figure 4.39. Optical image of the final solar cell indicating the size of samples and their placement regarding the wafer

For solar cell fabrication, saw damage etched wafers are used. The samples are textured using common laser parameters of Table 4.23 and three different laser power and frequency pair which are shown in Table 4.24. In addition, the samples are post-texture cleaned using 20% KOH solutions at 80°C for 2min and 4min. The optical images of as-textured and post-texture cleaned samples are shown in Figure 4.40.

Table 4.23. Common laser texturing parameters for solar cell fabrication

| | <i>Pattern</i> | <i>Draw Step</i> | <i>Step Period</i> | <i>Line Spacing</i> | <i>Iteration</i> |
|-------------------|----------------|------------------|--------------------|---------------------|------------------|
| | | <i>LSB</i> | μs | μm | <i>#</i> |
| Common Parameters | Criss-Cross | 25 | 120 | 75 | 1 |

Table 4.24. Changing laser texturing and post-texture cleaning parameters for solar cell fabrication

| | <i>Frequency</i> | <i>Power</i> | <i>Post-texture cleaning durations</i> |
|-------|------------------|--------------|--|
| | <i>kHz</i> | <i>%</i> | <i>min</i> |
| Set 1 | 30 | 100 | 2, 4 |
| Set 2 | 55 | 100 | 2, 4 |
| Set 3 | 55 | 80 | 2, 4 |

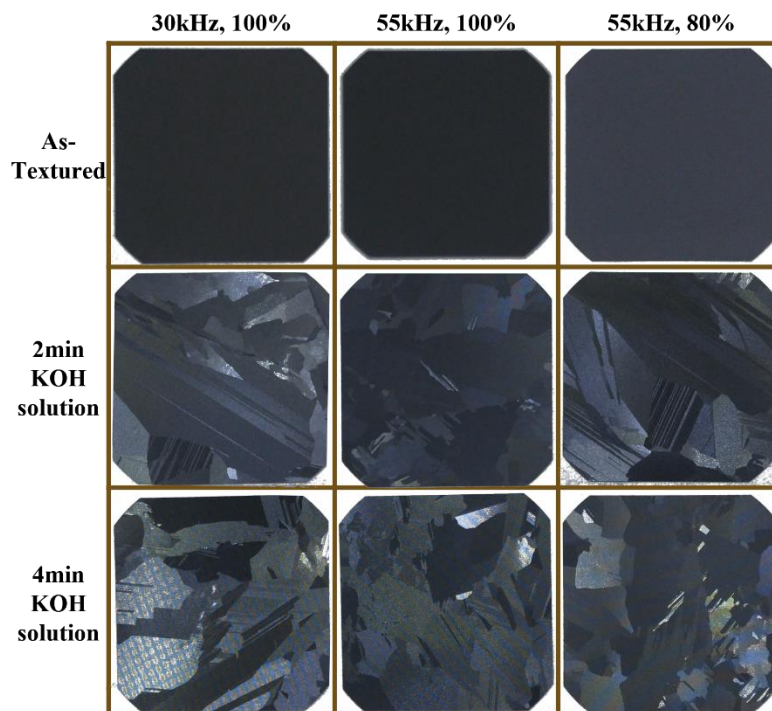


Figure 4.40. Optical image of all samples

In addition, the top view of the SEM images of the samples after each step is taken and illustrated in Figure 4.41. The effects of the laser texturing and post-texture cleaning steps are clearly seen in the figure. The 45° tilted view and the cross-section view of the SEM images are presented in Appendix G.

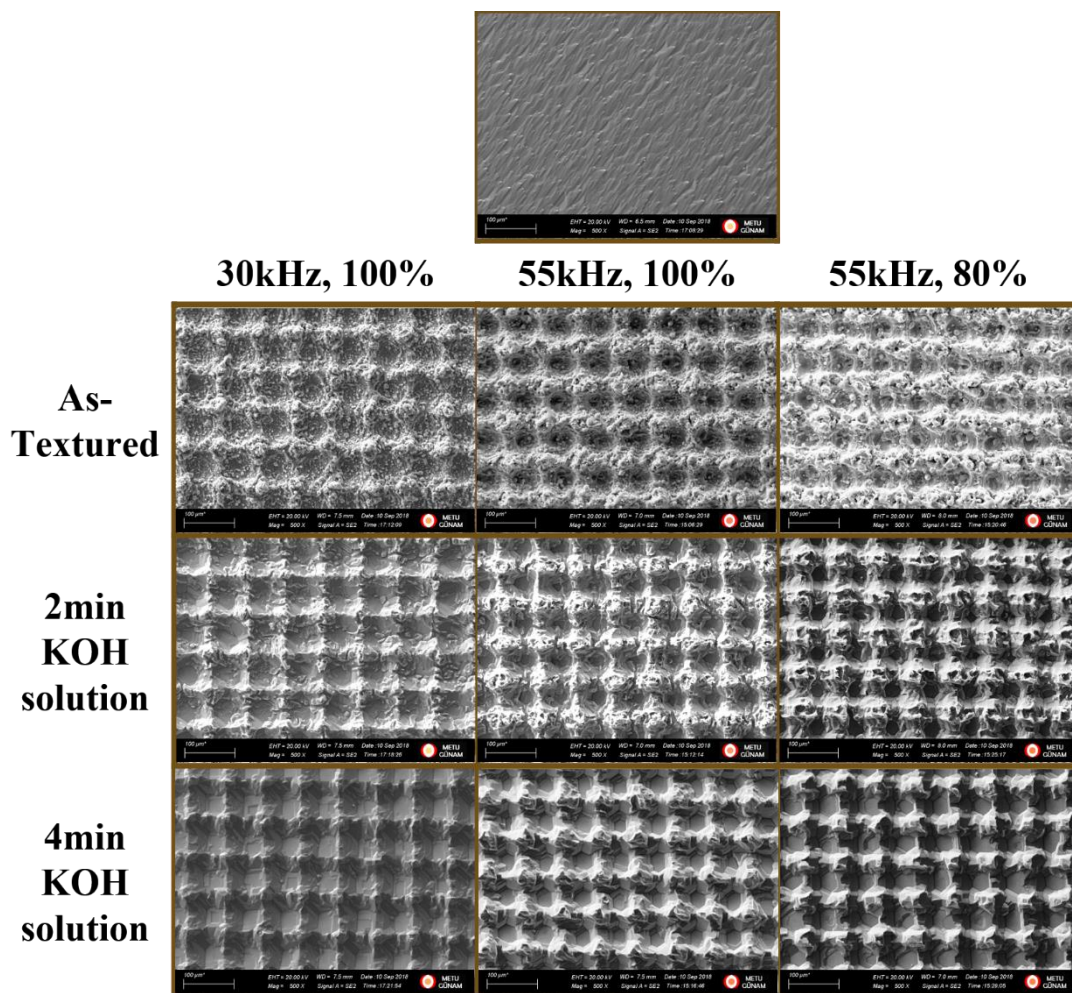


Figure 4.41. Top view SEM images of all samples

After laser texturing and post texture cleaning, general solar cell fabrication steps are followed, i.e. phosphorous doping, anti-reflection coating deposition, and frontside and backside metallization as mentioned in Section 3. The annealing after the metallization step is performed at three different speeds. Figure 4.42 shows the optical image of the saw damage etched sample (left), non-textured reference (middle), and one of the final fabricated solar cells (right).



Figure 4.42. Saw damage etched sample (left), Un-textured reference (middle), and laser textured sample (right)

The reflection curves of all samples are measured after each step. Figure 4.43 shows (left) the weighted reflection of samples after laser texturing and post-texture cleaning and (right) after ARC depositing. The reflection curves of the samples without ARC are presented in Appendix H.

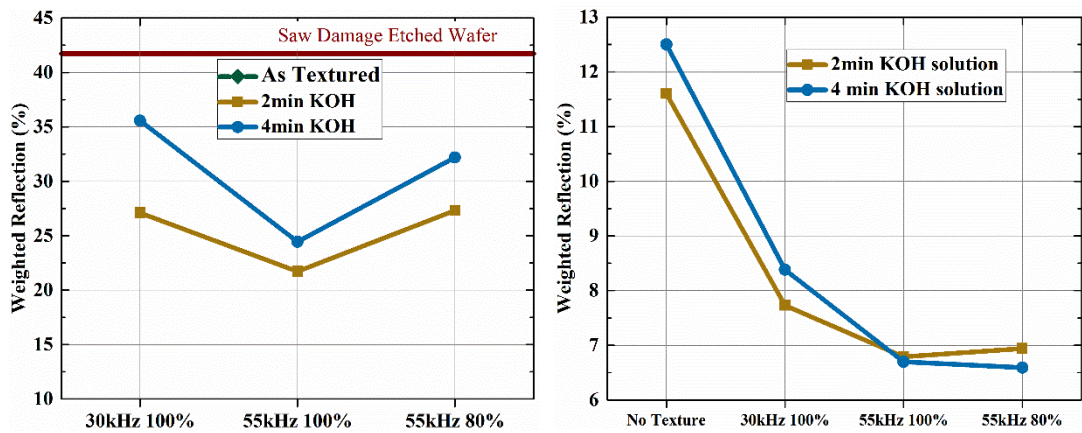


Figure 4.43. Weighted reflection of samples (left) without and (right) with ARC layer

After the metallization and annealing steps, the SEM images of fingers are taken and shown in Figure 4.44 as the top view, Figure 4.45 as the 45° tilted view, and Figure 4.46 as the cross-section view

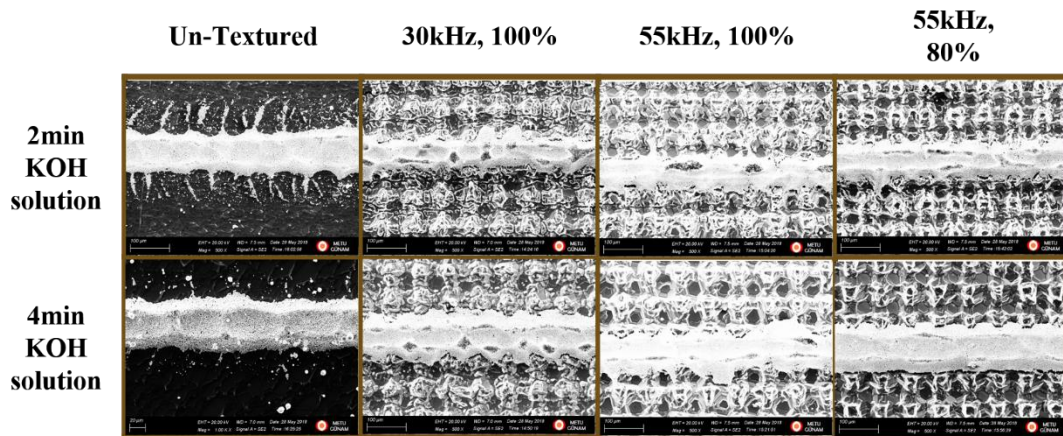


Figure 4.44. Top view SEM images of fingers on all samples

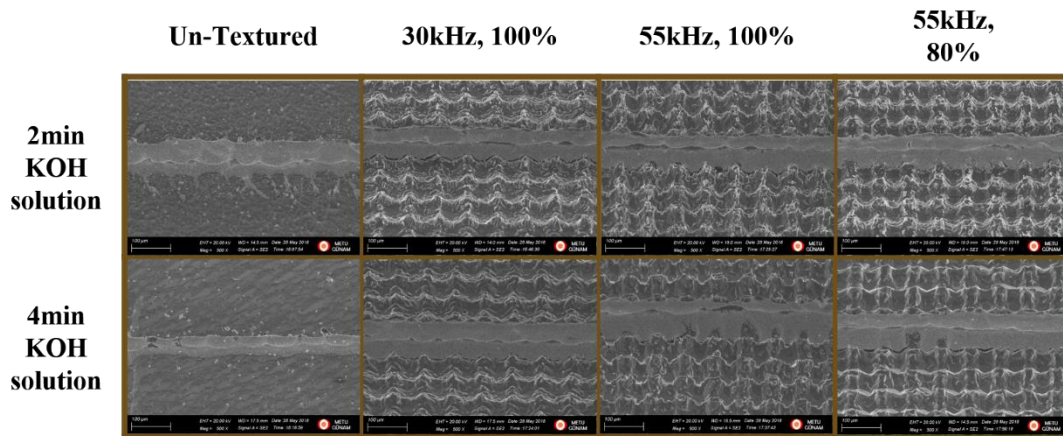


Figure 4.45. 45° tilted view SEM images of fingers on all samples

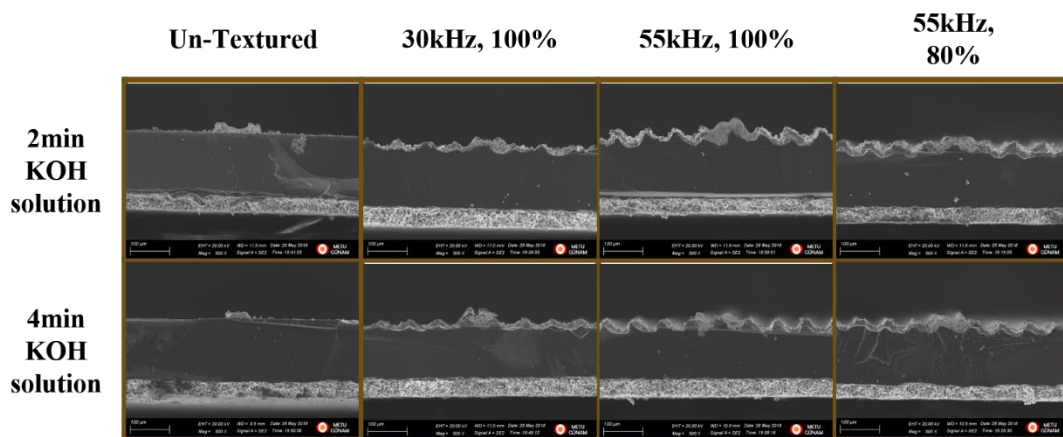


Figure 4.46. Cross section view SEM images of fingers on all samples

As it is seen in the figures above, the finger width varies from around 90 μm to 110 μm and the spacing between fingers is 1.55mm. In addition, the attachment of fingers to the textured surface is not perfect due to the surface roughness.

Then, the solar cells' performance is determined by measuring the I-V curves and extracting V_{oc} , J_{sc} , FF, and the efficiency of each sample. As shown in Figure 4.47 (left), the solar cell's efficiency increases with certain laser parameters up to 0.6% compared to the un-textured reference. The fill factor shown in Figure 4.47 (right) drops by laser texturing and regains by increasing the post-texture cleaning duration.

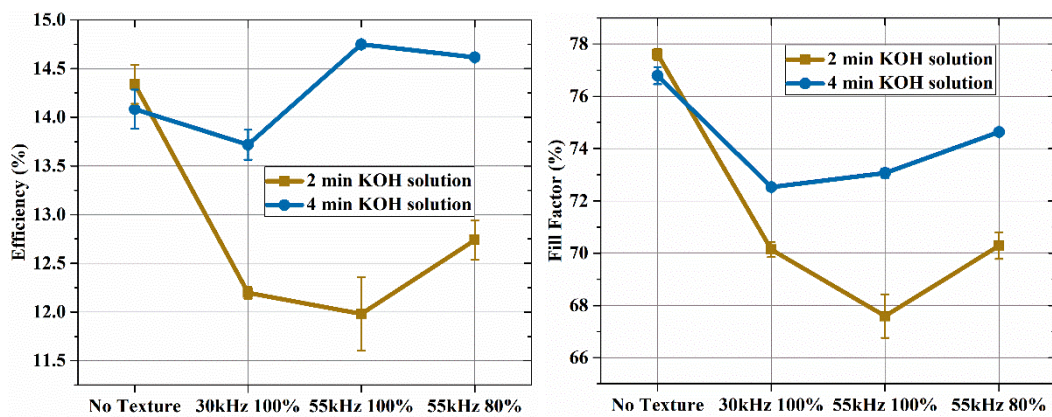


Figure 4.47. Efficiency (left) and fill factor (right) of fabricated solar cells

The V_{oc} decrease in Figure 4.48 (left) with laser texturing is due to an increase in the total surface area and roughness which increases the surface recombination of the generated minority carriers. However, increasing the post-texture cleaning duration increases V_{oc} as a result of a decrease in the surface roughness. The J_{sc} shown in Figure 4.48 (right) confirms the effectiveness of the process. As it is seen in the figure, texturing increases the J_{sc} as a result of increased absorption of the light in Si bulk. In addition, increasing post-texture cleaning duration improves J_{sc} , which is contrary to the behavior of the other parameters. This observation demonstrates that J_{sc} increases with proper surface texturing, and higher roughness does not necessarily mean more light absorption and thus, higher J_{sc} .

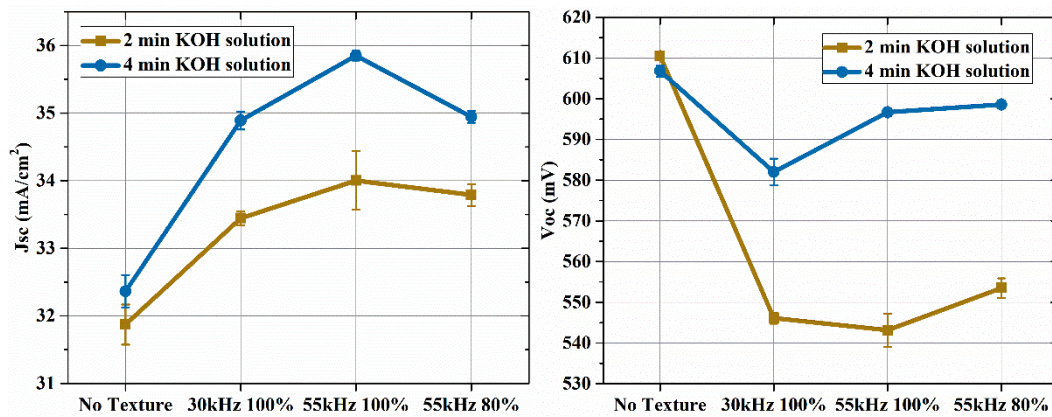


Figure 4.48. Jsc (left) and Voc (right) of fabricated solar cells

The result of the TLM is illustrated in Figure 4.49. In this figure, the contact resistance increases by texturing which is expected since the fingers' attachment to the textured surface is not formed perfectly and it can be seen in the SEM images. The error bars indicate the effect of different annealing on the samples.

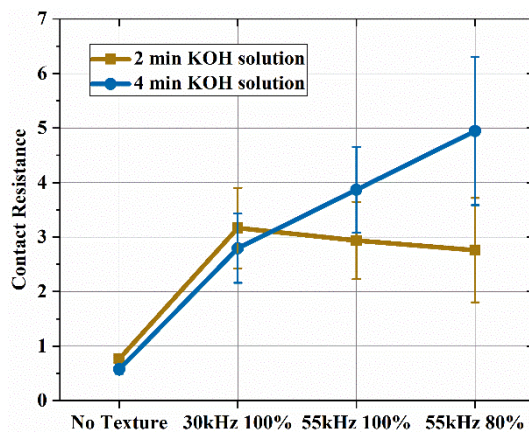


Figure 4.49. Contact resistance of fabricated solar cells

The EQE of the samples is measured as mentioned in Section 3.5.3. Figure 4.50 shows the EQE curves of the samples which are post-texture cleaned for (left) 2min and (right) 4min.

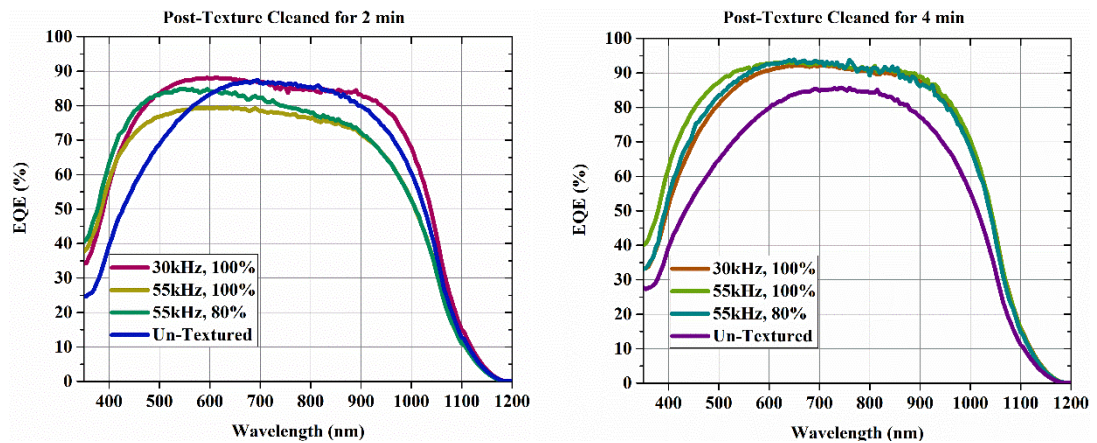


Figure 4.50. EQE of the fabricated solar cells post-textured for (left) 2min and (right) 4min

To calculate IQE, Eq. 1.17 is applied in which the EQE curves above and the reflection illustrated in Appendix H are utilized. The IQE curves are shown in Figure 4.51 from the samples which are post-texture cleaned for (left) 2min and (right) 4min.

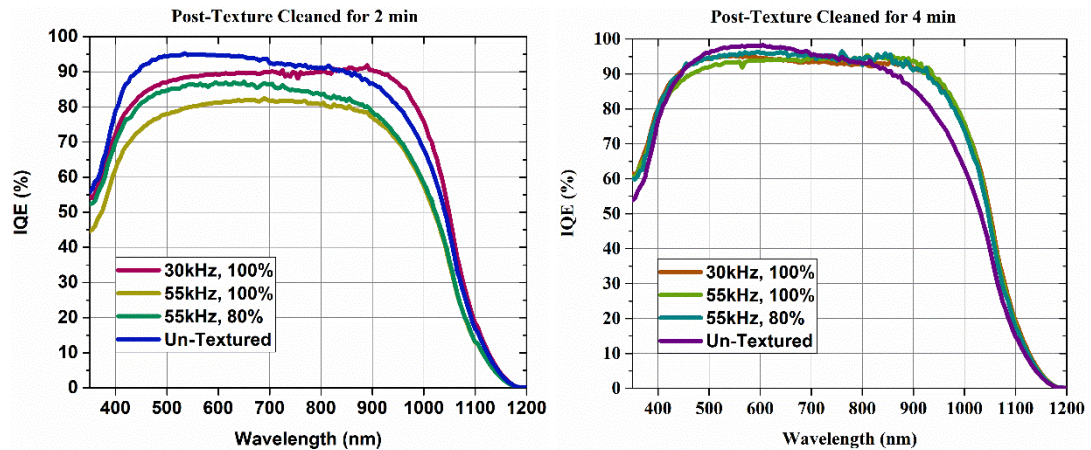


Figure 4.51. IQE of the fabricated solar cells post-textured for (left) 2min and (right) 4min

Finally, Figure 4.52 shows (left) I-V curves and (right) the reflection curves and IQE of the best fabricated solar cell and the best reference cell.

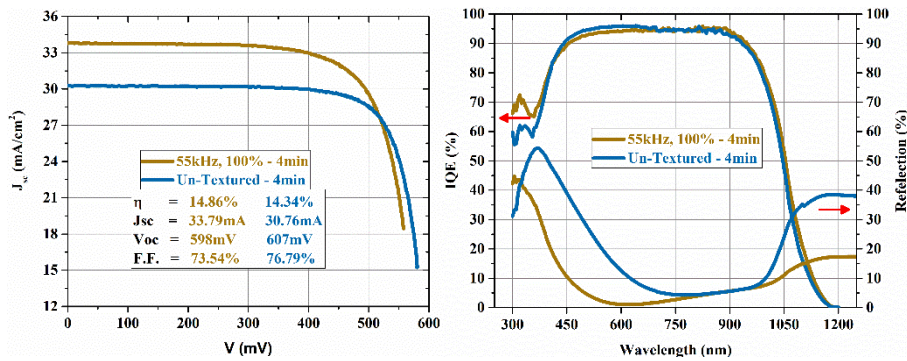


Figure 4.52. (left) I-V curves and (right) IQE and reflection curves of the best fabricated solar cell and reference solar cell

4.5. Quokka 2 Analysis

To confirm the experimental results with theoretical analysis, the results of different characterizations of the fabricated solar cells are also simulated using Quokka2 software.

Based on the sizes extracted from the SEM images of the solar cell, the unit cell geometry is $1.626\text{mm} \times 19.5\text{mm}$. It is possible to define the unit cell in two ways, by considering one finger (Figure 4.53 left) in which $W_{x.\text{front}}=W_{x.\text{rear}}=813\mu\text{m}$ or two fingers (Figure 4.53 right) in which $W_{x.\text{front}}=3*271\mu\text{m}$ and $W_{x.\text{rear}}=2*271\mu\text{m}$. Also, the analysis shows that the length of W_y is not effective. The thickness of the unit cell is $W_z=134\mu\text{m}$.

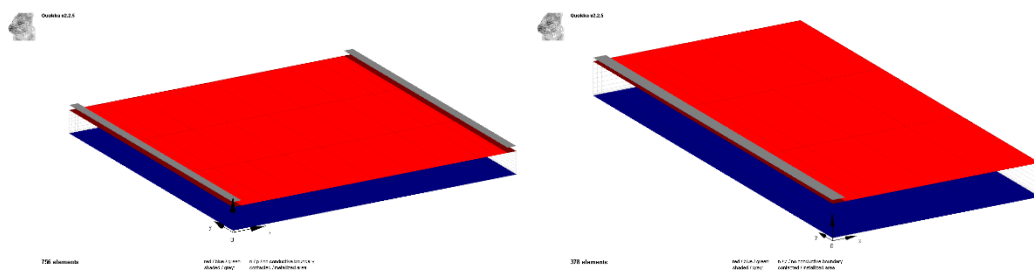


Figure 4.53. Defined geometry for Quokka 2 analysis with (left) two fingers and (right) one finger

To determine the generation profile, OPAL 2 simulation tool is used. The input parameters are shown in Figure 4.54 while the surface morphology is shown in Figure 4.55 (left) the planar fraction and (right) the characteristics angle.

Inputs

| | | |
|---|--|---|
| Surface morphology Regular ▾ Upright hillocks ▾ Charact. angle, ω 39 ° Planar fraction 27.5 % Distributed planar ▾ | Incident illumination Spectrum AM1.5g [Gue9 ▾] Zenith angle, θ 0 ° | Light trapping model $Z = 4 + \ln[n^2 + (1-n^2)e^{-4aW}]$ ▾ Substrate width, W 134 μm |
|---|--|---|

| | | | | | | | |
|---|--------------|---------------|-------------------------------------|-----------------|----------------------------|----------------------|---------------------------|
| | Layer | t (nm) | Optim. | Material | + Add Film 2 | ↓ Flip layers | → Visit RI library |
| | Superstrate | | | Air ▾ | [] | | |
| x | Film 1 | 88 | <input checked="" type="checkbox"/> | SiNx ▾ | PECVD [Bak11] | | |
| | Substrate | | | Si ▾ | Crystalline, 300 K [Gre08] | | |

Optimisation goal: Maximise ▾ Photon current absorbed in substrate ▾

Figure 4.54. Input parameters for OPAL 2 analysis

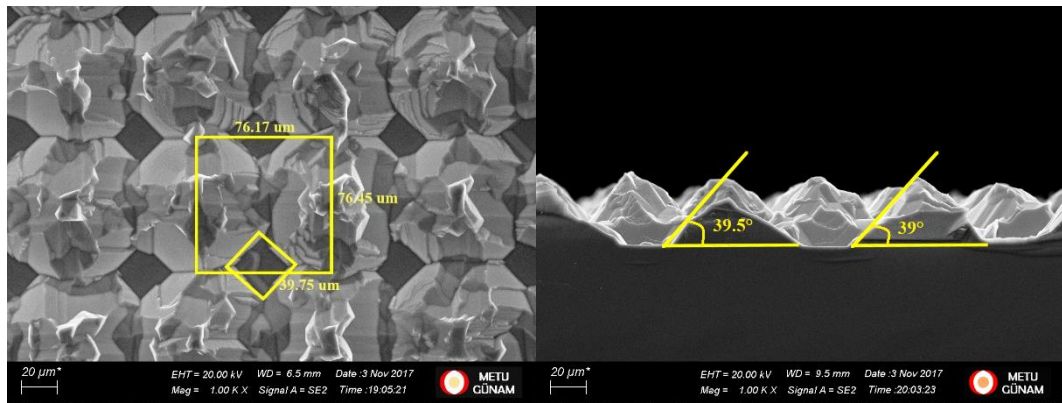


Figure 4.55. Surface morphology used for OPAL 2 analysis (left) the planar fraction and (right) the characteristics angle

Later, the reflection curve and IQE of the sample is loaded into the OPAL 2 and the thickness of the Si_3N_4 anti-reflection coating is fitted and determined as 88nm. Figure 4.56 shows the reflection curve and IQE of the sample in thick lines and reflection, transmission, and absorption of the fitted curve in thin lines. In addition, OPAL 2 gives the absorbed current based on the optical properties and short circuit current (J_{sc}).

Outputs

| Reflections | Unique paths | Fraction | Photon current | | mA/cm ² | Fraction |
|----------------|--------------|----------|-----------------------|-----------|--------------------|----------|
| 1 reflection | 2 | 75.7% | Incident | J_{Inc} | 43.75 | 100.0% |
| 2 reflections | 1 | 24.3% | Reflected | J_R | 3.68 | 8.4% |
| 3 reflections | 0 | 0.0% | Absorbed in films | J_A | 0.31 | 0.7% |
| 4+ reflections | 0 | 0.0% | Absorbed in substrate | J_G | 39.75 | 90.9% |
| Total | 3 | 100.0% | Short circuit current | J_{sc} | 34.85 | |

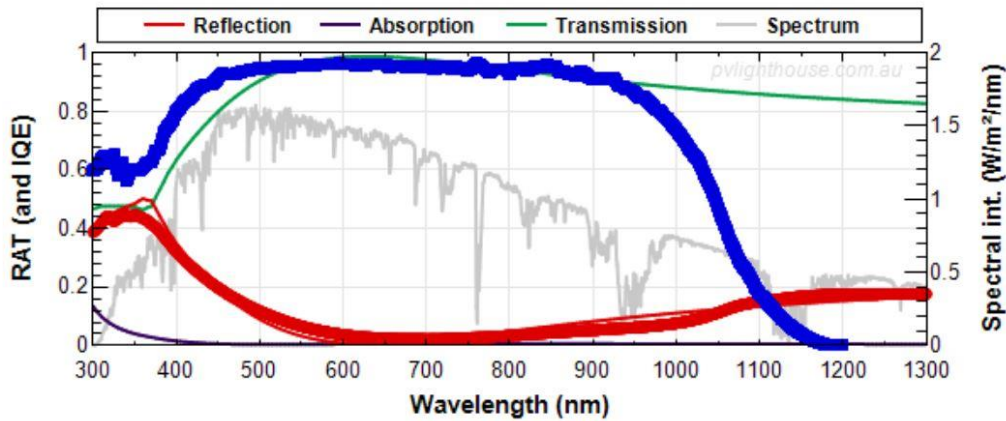


Figure 4.56. Reflection curve and IQE of the sample in thick lines and reflection, transmission, and absorption of the fitted curve in thin lines.

The RMSE error of the fitting for the wavelength range of 300nm to 1300nm is 2.51×10^{-2} which is shown in Figure 4.57.

| Simulated vs experimental reflection: | | |
|---------------------------------------|----------|------------|
| Over λ range | 300 | to 1300 nm |
| RMSE of fit | 2.518E-2 | |

Figure 4.57. RMSE error of fitting OPAL 2

The generation profile is extracted from the OPAL 2 and used in Quokka 2 as an external generation file. Other parameters are chosen based on the general solar cell parameters. As mentioned in section 3.6, the codes of the Quokka 2 analysis are presented in Appendix C.

Table 4.25 shows the laser texturing and post-texture cleaning parameters of the fabricated and the simulated solar cell. The simulated I-V curve and the solar cell's performance are shown in Figure 4.58 which fairly confirms the experimental results that are shown in Table 4.26.

Table 4.25. Parameters of sample simulated using Quokka 2

| | Frequency | Power | Pattern | Draw Step | Step Period | Line Spacing | Iteration | Post-texture cleaning duration |
|-------|------------|----------|-------------|------------|-------------|--------------|-----------|--------------------------------|
| | <i>kHz</i> | <i>%</i> | | <i>LSB</i> | <i>μs</i> | <i>μm</i> | <i>#</i> | <i>min</i> |
| Set 3 | 55 | 80 | Criss-Cross | 25 | 120 | 75 | 1 | 4 |

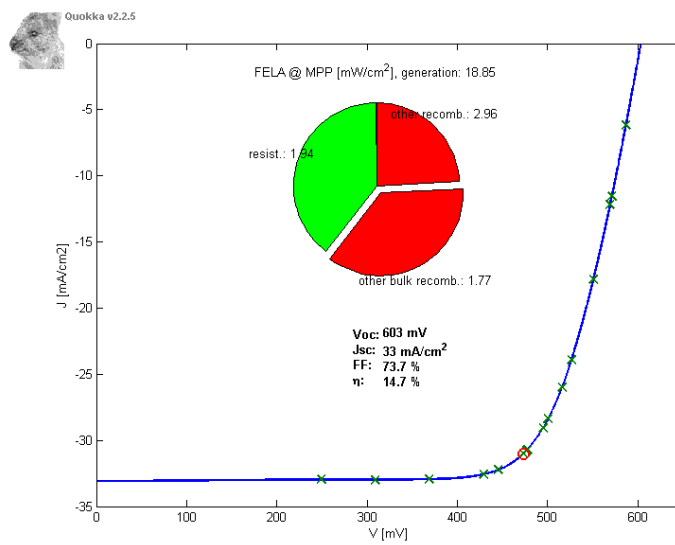


Figure 4.58. I-V curve of the simulated solar cell

Table 4.26. Comparison between experimental data and simulation results

| | <i>J_{sc}</i> | <i>V_{oc}</i> | <i>F.F</i> | <i>Efficiency</i> |
|------------|-----------------------|-----------------------|------------|-------------------|
| | <i>mA</i> | <i>mV</i> | <i>%</i> | <i>%</i> |
| Experiment | 32.95 | 596.14 | 74.74 | 14.682 |
| Simulation | 32.992 | 603.40 | 73.71 | 14.673 |

CHAPTER 5

CONCLUSION AND FUTURE STUDY

Texturing the surface of Si wafer is the first step in solar cell fabrication process. Simple and well established texturing processes are already available for texturing monocrystalline silicon wafers. These texturing processes are anisotropic and purely chemical which use a mixture of IPA and KOH, NaOH, or TMAH. These anisotropic texturing processes lead to pyramid shape surfaces of monocrystalline silicon with surface orientation of (100).

In contrast, it is not viable to use anisotropic texturing chemical solutions on the multi-crystalline silicon wafers because of their random crystallographic orientation at their surface. Thus, the isotropic texturing methods of multi-crystalline silicon are developed. However, acid based isotropic texturing methods are not sufficiently good for light management. For this reason, alternative techniques have been sought by many research groups.

In the current study, an isotropic texturing method is developed which utilizes the laser equipment. The laser processing leads to have line grooves or separated laser spots structures on the silicon wafer's surface regardless of the silicon wafer type. It is thus applicable to both multi-crystal and mono-crystal Si wafers. In this work, nanosecond IR laser with the wavelength of 1064nm has been used to optimize laser-based texturing process.

Before going through the laser texturing parameters, several wafers were textured using certain laser parameter to verify that the proposed laser texturing process is capable of processing the full-size wafers. The SEM images of resultant surface structures from different locations proved the capability of the laser texturing of full-size silicon wafers.

In the first phase, the laser texturing parameters including laser scanner motor parameter are justified by a series of experiments. The effect of laser parameters is summarized below:

-Laser Power

The laser power changes the depth and also the amount of the laser ablated residues. The low laser power cannot texture the silicon surface and is not effective. In this study, the maximum laser power is normally used to produce the laser textured structures and the residues are removed in the post-texture cleaning step.

-Laser Pulse Frequency

Laser pulse frequency, together with the laser scanner motor parameters, changes the overlap between the laser spots. In addition, the lower laser pulse frequency transfers more energy to the silicon surface.

-Laser Lines Spacing

The laser line spacing is important because the surface must be textured as much as possible and the flat (untextured) area must be minimized. The distance between the lines have been minimized.

-Laser Scanner Motor: Draw Step & Step Period

It is worth mentioning that the laser texturing speed depends only on the laser scanner motor parameters and the overlap between the laser spots depends on the laser scanner motor parameters and the laser pulse frequency. The positive overlap leads to line groove morphologies and the negative overlap leads to separated spot morphologies.

-Texturing Iteration

In the line grooves morphology, increasing the iteration increases the depth of the structures. In the separated spots morphologies, increasing the iteration results in deeper morphology or displaced morphology.

-Texturing Pattern

Two different patterns are used which are line and criss-cross patterns. The line pattern is used to fabricate separated spots structures while criss-cross is used to fabricate line groove morphologies and the cross sections act like separated spots for light absorption purposes.

Since the laser texturing leaves plenty of laser ablated residues, the surface is not suitable for fabricating solar cells. In addition to laser ablated residues, other residues and sharp edges must be removed from the surface since they make a suitable site for the recombination.

In the second phase, two post-texturing cleaning steps were investigated in the beginning. Both the physical post-texture cleaning using ultrasonic bath and chemical post-texture cleaning using 1% KOH solution at the room temperature are done with different durations.

The SEM images and the weighted reflection from the samples do not show a notable effect of these post-texture cleanings. Therefore, another chemical post-texture cleaning process using high concentration KOH solution at high temperature is used.

To enhance the surface morphology, the post-texture cleaning is done using KOH solution with different parameters. To have a comprehensive experiment, different KOH solutions with concentrations of 2%, 4%, 8%, 16%, 20%, and 32% at the temperatures of 60°C and 80°C with durations of 0.5min, 1min, 2min, 4min, and 8min are used.

The SEM images, the weighted reflection, and reflection curves of the samples indicate that the morphology and its optical properties are highly dependent on post-texture cleaning parameters in such a way that with high concentration, high temperature, and high duration, almost all surface features are removed since KOH solution is an isotropic etching solution at this conditions. In comparison, low concentration, low temperature, and low duration do not affect surface very much.

In the third phase, to have an outlook about the potentials of the proposed process, the laser textured and the post-texture cleaned samples were prepared for depositing the passivation layer and the antireflection coating. First, three laser texturing parameters and two post-texture cleaning durations using 20% KOH solution at 80°C were selected. Then, 14.39nm Al₂O₃ as a passivation layer was deposited on the samples using ALD system. The measured iV_{oc} and the weighted reflection of the samples indicate that high iV_{oc} around 692mV with a reasonable weighted reflection can be achieved for a sample with the laser power of 80%, the laser pulse frequency of 55kHz, and the post-texture cleaning duration of 4min. Second, four samples from previous experiments were selected for depositing Si₃N₄ with thicknesses of 65nm, 75nm, 85nm as an antireflection coating. The weighted reflection and the reflection curves of the samples proved that very low weighted reflection as 4.18% can be achieved with proper ARC thickness around 85nm.

In the final phase, the solar cells were fabricated using the proposed laser texturing and the post-texture cleaning method. The samples were first textured with three different laser parameters, second post-textured cleaned with two durations, third doped in solid state diffusion furnace with Phosphorous to form junction, fourth Si₃N₄ was deposited using PECVD system, fifth screen printed Ag at the front surface as fingers and Al at the rear surface, and sixth annealed in the firing belt. Note that the solar cell fabrication steps including doping, ARC deposition, metallization, and firing are not optimized for the samples.

The SEM images of the solar cells show that the attachment of the fingers to the front surface is not perfect. The TLM measurement indicated high contact resistance which confirms the imperfection of the contacts. The weighted reflection of the samples can be as low as 6.19% in the final structure. Finally, the I-V curves of the samples showed that the efficiency of 14.86% can be achieved without optimizing the solar cell fabrication steps. For the best fabricated solar cell, the V_{oc} of 598mV, J_{sc} of 33.79 mA/cm², and F.F. of 73.54% were achieved. The reference sample showed an efficiency of 14.34%, proving the potential of laser texturing process.

In conclusion, we have demonstrated that laser texturing is a powerful alternative to wet chemical etching processes in particular for the multi-crystal wafers. However, there is still a room for the further improvements. For future studies, different laser equipment in terms of laser wavelength (IR, Green, UV) and laser pulse frequency (nanosecond, picosecond, femtosecond) can be employed. In addition, it is possible to investigate other post-texture cleaning solutions rather than KOH solution like other anisotropic (NaOH) and isotropic solutions (HNA, HNO₃). Finally, it may be beneficial to use the proposed technique on different types of solar cell and not be only limited to the conventional type.

In the next chapter “PUBLISHED ARTICLES FROM THESIS WORK”, the published articles regarding each phase of this study are presented.

CHAPTER 6

PUBLISHED ARTICLES FROM THESIS WORK

- [1] B. Radfar, F. Es, R. Turan, “Investigation on Different Surface Modifications Using Laser Texturing”, in: 33rd Eur. Photovolt. Sol. Energy Conf. Exhib., WIP, Amsterdam, 2017: pp. 706–709. doi:10.4229/EUPVSEC20172017-2AV.2.48.
- [2] B. Radfar, F. Es, H. Nasser, O. Akdemir, A. Bek, R. Turan, “Effect of laser parameters and post-texturing treatments on the optical and electrical properties of laser textured c-Si wafers”, in: AIP Conf. Proc., Lausanne, 2018: p. 050008. doi:10.1063/1.5049298.
- [3] B. Radfar, F. Es, R. Turan, “Investigation on Post Cleanings on Modified Surface Using Laser Texturing”, in: 35th Eur. Photovolt. Sol. Energy Conf. Exhib., WIP, Brussels, 2018: pp. 614–616. doi:10.4229/35thEUPVSEC20182018-2AV.2.41.
- [4] B. Radfar, F. Es, R. Turan, “Effects of Different Laser Modified Surface Morphologies and Post-Texturing Cleanings on Si Wafer”, in: PVCON 2018, Ankara, 2018, Submitted to Elsevier’s Renewable Energy – Special Issue.

REFERENCES

- [1] The Nobel Prize organisation, The Nobel Prize in Chemistry 1997, <https://www.nobelprize.org/prizes/chemistry/1997/summary/>. (n.d.). <https://www.nobelprize.org/prizes/chemistry/1997/summary/> (accessed November 22, 2018).
- [2] P.J. Golas, J. Needham, Joseph Needham's Science and Civilisation in China, Volume 5. Chemistry and Chemical Technology Part XIII: Mining. By Peter J. Golas., 2000. http://www.journals.cambridge.org/abstract_S0305741000014818.
- [3] the free encyclopedia Wikipedia, History of coal mining, https://en.wikipedia.org/wiki/History_of_coal_mining. (n.d.). https://en.wikipedia.org/wiki/History_of_coal_mining (accessed November 22, 2018).
- [4] Y. Deng, Ancient Chinese Inventions (Introductions to Chinese Culture), Cambridge University Press, 2013.
- [5] the free encyclopedia Wikipedia, Peak Oil, https://en.wikipedia.org/wiki/Peak_oil. (n.d.). https://en.wikipedia.org/wiki/Peak_oil (accessed November 22, 2018).
- [6] the free encyclopedia Wikipedia, Peak Coal, https://en.wikipedia.org/wiki/Peak_coal. (n.d.). https://en.wikipedia.org/wiki/Peak_coal (accessed November 22, 2018).
- [7] BP p.l.c., Renewable energy - BP Statistical Review of World Energy 2018, <https://www.bp.com/content/dam/bp/en/corporate/pdf/energy-economics/statistical-review/bp-stats-review-2018-renewable-energy.pdf>. (n.d.). <https://www.bp.com/content/dam/bp/en/corporate/pdf/energy-economics/statistical-review/bp-stats-review-2018-renewable-energy.pdf> (accessed November 22, 2018).
- [8] Columbia University, Energy Consumption, <http://www.columbia.edu/~mhs119/EnergyConsump>. (n.d.). <http://www.columbia.edu/~mhs119/EnergyConsump> (accessed November 22, 2018).
- [9] Fraunhofer Institute for Solar Energy Systems ISE, Photovoltaics Report, <https://www.ise.fraunhofer.de/content/dam/ise/de/documents/publications/studies/Photovoltaics-Report.pdf>. (n.d.). <https://www.ise.fraunhofer.de/content/dam/ise/de/documents/publications/studies/Photovoltaics-Report.pdf> (accessed November 22, 2018).

- [10] W. Shockley, H.J. Queisser, Detailed Balance Limit of Efficiency of p-n Junction Solar Cells, *J. Appl. Phys.* 32 (1961) 510–519. doi:10.1063/1.1736034.
- [11] NREL, NNREL's "Best Research-Cell Efficiencies" Chart o Title, <https://www.nrel.gov/pv/assets/pdfs/pv-efficiencies-07-17-2018.pdf>. (n.d.). <https://www.nrel.gov/pv/assets/pdfs/pv-efficiencies-07-17-2018.pdf> (accessed November 22, 2018).
- [12] W. Futako, T. Kamiya, C.M. Fortmann, I. Shimizu, The structure of 1.5–2.0 eV band gap amorphous silicon films prepared by chemical annealing, *J. Non-Cryst. Solids.* 266–269 (2000) 630–634. doi:10.1016/S0022-3093(99)00756-5.
- [13] D.E. Carlson, C.R. Wronski, Amorphous silicon solar cell, *Appl. Phys. Lett.* 28 (1976) 671–673. doi:10.1063/1.88617.
- [14] NREL, Cadmium Telluride Solar Cells | Photovoltaic Research | NREL, <https://www.nrel.gov/pv/cadmium-telluride-solar-cells.html>. (n.d.). <https://www.nrel.gov/pv/cadmium-telluride-solar-cells.html%0A> (accessed November 22, 2018).
- [15] NREL, Copper Indium Gallium Diselenide Solar Cells | Photovoltaic Research | NREL, <https://www.nrel.gov/pv/copper-indium-gallium-diselenide-solar-cells.html>. (n.d.). <https://www.nrel.gov/pv/copper-indium-gallium-diselenide-solar-cells.html%0A> (accessed November 22, 2018).
- [16] M. Liu, M.B. Johnston, H.J. Snaith, Efficient planar heterojunction perovskite solar cells by vapour deposition, *Nature.* 501 (2013) 395–398. doi:10.1038/nature12509.
- [17] D.B. Lee, Anisotropic Etching of Silicon, *J. Appl. Phys.* 40 (1969) 4569–4574. doi:10.1063/1.1657233.
- [18] A.-E. Becquerel, Recherches sur les effets de la radiation chimique de la lumiere solaire au moyen des courants electriques, *Comptes Rendus L'Academie Des Sci.* 9 (1839) 145–149.
- [19] A.-E. Becquerel, Mémoire sur les effets électriques produits sous l'influence des rayons solaires, *C. R. Hebd. Seances Acad. Sci.* 9 (1839) 561–567.
- [20] W.G. Adams, R.E. Day, V. The action of light on selenium, in: *Proc. R. Soc. London*, 1877: pp. 113–117.
- [21] D.M. Chapin, C.S. Fuller, G.L. Pearson, A New Silicon p-n Junction Photocell for Converting Solar Radiation into Electrical Power, *J. Appl. Phys.* 25 (1954) 676–677. doi:10.1063/1.1721711.
- [22] M.A. Green, High-Efficiency Silicon Solar Cell Concepts, in: *McEvoy's Handb. Photovoltaics*, Elsevier, 2018: pp. 95–128. doi:10.1016/B978-0-12-

809921-6.00005-7.

- [23] A. Richter, M. Hermle, S.W. Glunz, Reassessment of the Limiting Efficiency for Crystalline Silicon Solar Cells, *IEEE J. Photovoltaics*. 3 (2013) 1184–1191. doi:10.1109/JPHOTOV.2013.2270351.
- [24] James D. Plummer, M.D. Deal, P.B. Griffin, *Silicon VLSI Technology Fundamentals, Practice and Modeling*, 2000.
- [25] H. Seidel, L. Csepregi, A. Heuberger, H. Baumgartel, Anisotropic Etching of Crystalline Silicon in Alkaline Solutions, *J. Electrochem. Soc.* 137 (1990) 3626. doi:10.1149/1.2086278.
- [26] O. Tabata, R. Asahi, H. Funabashi, K. Shimaoka, S. Sugiyama, Anisotropic etching of silicon in TMAH solutions, *Sensors Actuators A Phys.* 34 (1992) 51–57. doi:10.1016/0924-4247(92)80139-T.
- [27] R.M. Finne, D.L. Klein, A Water-Amine-Complexing Agent System for Etching Silicon, *J. Electrochem. Soc.* 114 (1967) 965. doi:10.1149/1.2426793.
- [28] X. N, Quiebras, *Wet chemical textures for crystalline silicon solar cells*, 2013.
- [29] F. Es, G. Baytemir, M. Kulakci, R. Turan, Metal-assisted nano-textured solar cells with SiO₂/Si₃N₄ passivation, *Sol. Energy Mater. Sol. Cells*. 160 (2017) 269–274. doi:10.1016/j.solmat.2016.10.032.
- [30] J.D. Hylton, A.R. Burgers, W.C. Sinke, Alkaline Etching for Reflectance Reduction in Multicrystalline Silicon Solar Cells, *J. Electrochem. Soc.* 151 (2004) G408. doi:10.1149/1.1738137.
- [31] D.H. Macdonald, A. Cuevas, M.J. Kerr, C. Samundsett, D. Ruby, S. Winderbaum, A. Leo, Texturing industrial multicrystalline silicon solar cells, *Sol. Energy*. 76 (2004) 277–283. doi:10.1016/j.solener.2003.08.019.
- [32] M. Abbott, J. Cotter, Optical and electrical properties of laser texturing for high-efficiency solar cells, *Prog. Photovoltaics Res. Appl.* 14 (2006) 225–235. doi:10.1002/pip.667.
- [33] B.K. Nayak, V. Iyengar, M.C. Gupta, Ultrafast Laser Textured Silicon Solar Cells, *MRS Proc.* 1123 (2008) 1123-P07-09. doi:10.1557/PROC-1123-1123-P07-09.
- [34] V. V. Iyengar, B.K. Nayak, M.C. Gupta, Optical properties of silicon light trapping structures for photovoltaics, *Sol. Energy Mater. Sol. Cells*. 94 (2010) 2251–2257. doi:10.1016/j.solmat.2010.07.020.
- [35] B.K. Nayak, V. V. Iyengar, M.C. Gupta, Efficient light trapping in silicon solar cells by ultrafast-laser-induced self-assembled micro/nano structures, *Prog. Photovoltaics Res. Appl.* 19 (2011) 631–639. doi:10.1002/pip.1067.

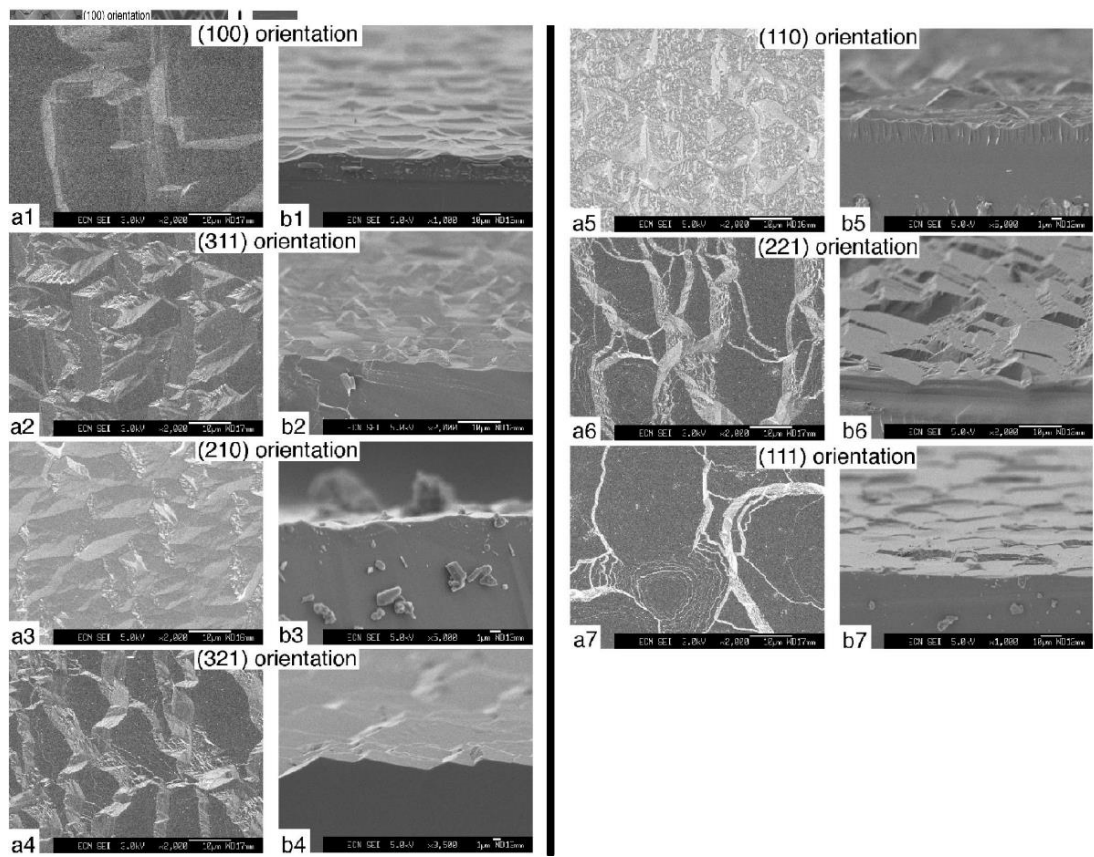
- [36] D. Zielke, D. Sylla, T. Neubert, R. Brendel, J. Schmidt, Direct laser texturing for high-efficiency silicon solar cells, *IEEE J. Photovoltaics*. 3 (2013) 656–661. doi:10.1109/JPHOTOV.2012.2228302.
- [37] V. Parmar, Y.C. Shin, Wideband anti-reflective silicon surface structures fabricated by femtosecond laser texturing, *Appl. Surf. Sci.* 459 (2018) 86–91. doi:10.1016/j.apsusc.2018.07.189.
- [38] L.A. Dobrzański, A. Drygała, K. Gołombek, P. Panek, E. Bielańska, P. Zięba, Laser surface treatment of multicrystalline silicon for enhancing optical properties, *J. Mater. Process. Technol.* 201 (2008) 291–296. doi:10.1016/j.jmatprotec.2007.11.278.
- [39] A. Fell, K.R. McIntosh, M. Abbott, D. Walter, Quokka version 2: selective surface doping, luminescence modeling and data fitting Andreas, in: 23rd Photovolt. Sci. Eng. Conf., Taipei, 2013.
- [40] A. Fell, K.C. Fong, K.R. McIntosh, E. Franklin, A.W. Blakers, 3-D Simulation of Interdigitated-Back-Contact Silicon Solar Cells With Quokka Including Perimeter Losses, *IEEE J. Photovoltaics*. 4 (2014) 1040–1045. doi:10.1109/JPHOTOV.2014.2320302.
- [41] A. Fell, A Free and Fast Three-Dimensional/Two-Dimensional Solar Cell Simulator Featuring Conductive Boundary and Quasi-Neutrality Approximations, *IEEE Trans. Electron Devices*. 60 (2013) 733–738. doi:10.1109/TED.2012.2231415.
- [42] K.R. McIntosh, S.C. Baker-Finch, OPAL 2: Rapid optical simulation of silicon solar cells, in: 2012 38th IEEE Photovolt. Spec. Conf., IEEE, 2012: pp. 000265–000271. doi:10.1109/PVSC.2012.6317616.

APPENDICES

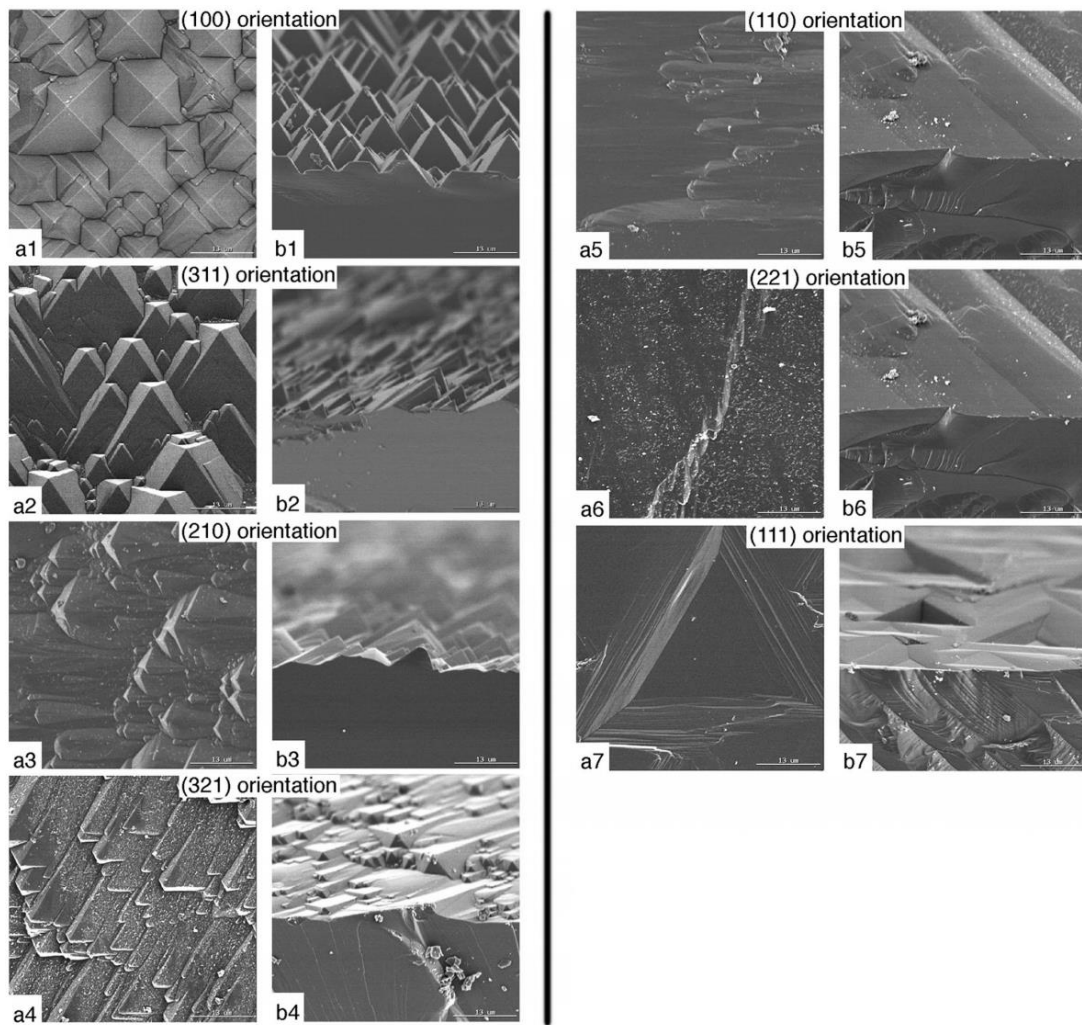
A. SEM Images of Texturing Using NaOH Solution

Related to Section 2.2.2.

1. SEM images of high concentration NaOH as a saw damage etching technique reported by Hylton et al. [31].



2. SEM images of low concentration NaOH as a texturing technique reported by Hylton et al. [31].



B. MATLAB Code for Reflection and Weighted Reflection Calculation

Related to Section 3.5.2. MATLAB code calculating reflection curves and weighted reflection by measuring BaSO₄ reference cell and samples' reflected intensity.

```
clear
clc
format long;
digits(20);
str='go';
flag=1;
while (~strcmp(str,'exit') && flag)
    flag=0;
    %input folder & files
    %prompt='Input directory of measurments:\n';
    %str = input(prompt,'s');
    str='D:\Google Drive\Project\MY\W35-2018-03-09\Reflections\Textured-KOH cleaned- Temp
(80)\Concentration 2%';
    cd(str);
    %Input files
    Dark_files=dir(fullfile(str,'dark*.txt'));
    Background_files=dir(fullfile(str,'BaSO4*.txt'));
    Sample_files=dir(fullfile(str,'S*.txt'));
    if (isempty(Background_files) && ~strcmp(str,'exit'))
        prompt='There are no Background here!! Try agian,,,';
        disp(prompt);
        flag=1;
    end
    if (isempty(Sample_files) && ~strcmp(str,'exit'))
        prompt='There are no samples here!! Try agian,,,';
        disp(prompt);
    end
end
```

```

        flag=1;
    end
end
%end program if exit
if strcmp(str,'exit')
    return ;
end
%Settings
dark_OK_str='no';
if ~isempty(Dark_files)
    prompt='Consider dark??\n';
    dark_OK_str = input(prompt,'s');
end
if strcmp(dark_OK_str,'yes')
    dark_OK=1;
else
    dark_OK=0;
end
%Preallocation Variables
%Dark Measurment : Read Files
for i=1:length(Dark_files)
    DarkID(i) = fopen(Dark_files(i).name);
    Temp = fscanf(DarkID(i), '%f %f',[2 inf]);
    Dark_files(i).value=Temp(2,:);
    Dark_files(i).value=Dark_files(i).value';
    fclose(DarkID(i));
end
%Background Measurment : Read files
for i=1:length(Background_files)
    BackgroundID(i) = fopen(Background_files(i).name);
    Background_files(i).value = fscanf(BackgroundID(i), '%g %g',[2 inf]);
    Background_files(i).value=Background_files(i).value';

```

```

fclose(BackgroundID(i));
end
%Background Measurment : Find Max
for i=1:length(Background_files(1).value)
    Background(i)=0;
    for j=1:length(Background_files)
        Background(i)=max(Background(i), Background_files(j).value(i,2));
    end
end
Background=Background';
%Sample Measurment : Read Files
for i=1:length(Sample_files)
    SampleID(i) = fopen(Sample_files(i).name);
    Temp = fscanf(SampleID(i), '%f %f',[2 inf]);
    Sample_files(i).value=Temp(2,:);
    Sample_files(i).value=Sample_files(i).value';
    fclose(SampleID(i));
end
Wavelength=Background_files(1).value(:,1);
prompt='Show Background?? \n';
%Show_Background = input(prompt,'s');
Show_Background='no';
if strcmp(Show_Background,'yes')
    plot (Wavelength,Background);
end
prompt='Do you want to save in file?? \n';
%Save_file = input(prompt,'s');
Save_file='yes';
if ~strcmp(Save_file,'no')
    prompt='Give save directory:\n';
    directory = input(prompt,'s');
    %prompt='Give file name:\n';

```

```

%file_name = input(prompt,'s');
file_name='Reflections';
File_directory_name=strcat(directory,file_name,'.txt');
flag2=1;
else
flag2=0;
end
prompt='Do you want to show Figures?? \n';
%Show_figures = input(prompt,'s');
Show_figures = 'no';
if ~strcmp(Show_figures,'no')
prompt='Number of samples per figure?? in this format [X Y] \n';
sample_per_figure = input(prompt);
flag=1;
figure
else
flag=0;
end
BaSO4_R_file=dir(fullfile(str,'BaSO4*.xlsx'));
BaSO4_R_read = xlsread(BaSO4_R_file.name);
BaSO4_R = BaSO4_R_read(:,2);
j=1;
%Reflection
for i=1:length(Sample_files)
if dark_OK
Sample_files(i).value=(Sample_files(i).value-Dark_files(1).value)/((Background./BaSO4_R)-
Dark_files(1).value);
else
Sample_files(i).value=Sample_files(i).value./((Background./BaSO4_R));
end
if flag
if j>(sample_per_figure(1) * sample_per_figure(2))

```

```

        figure
        j=1;
    end
    subplot(sample_per_figure(1) , sample_per_figure(2),j)
    plot (Wavelength,Sample_files(i).value);
    title(Sample_files(i).name);
    xlabel('Wavelength');
    ylabel('Reflection');
    j=j+1;
end
end
if flag2
    save_file = fopen(File_directory_name,'wt');
    fprintf(save_file,'%s \t','Wavelength');
    for j=1:length(Sample_files)
        fprintf(save_file,'%s\t',Sample_files(j).name);
    end
    fprintf(save_file,'\n');
    for i=1:length(Wavelength)
        fprintf(save_file,'%d\t',Wavelength(i));
        for j=1:length(Sample_files)
            fprintf(save_file,'%d\t',Sample_files(j).value(i));
        end
        fprintf(save_file,'\n');
    end
    fclose(save_file);
end
prompt='Do you want to calculate Weighted Reflection?? \n';
>Show_Weighted_Reflection = input(prompt,'s');
>Show_Weighted_Reflection = 'yes';
if ~strcmp>Show_Weighted_Reflection,'no')

```

```

file_name='Weighted_Reflections';
File_directory_name=strcat(directory,file_name,'.txt');
save_file = fopen(File_directory_name,'wt');

AM_file=dir(fullfile(str,'am*.xls'));
AM_1_5 = xlsread(AM_file.name);
j=1;
for i=1:length(AM_1_5)
    if ~mod(AM_1_5(i,1),10) && AM_1_5(i,1)> Wavelength(1)-1 && AM_1_5(i,1)
<Wavelength(length(Wavelength))+1;
        AM_1_5G(j)=AM_1_5(i,3);
        j=j+1;
    end
end
AM_1_5G=AM_1_5G';
for i=1:length(Sample_files)
    num=0;
    den=0;
    for j=1:length(Wavelength)
        num=num+Sample_files(i).value(j)*AM_1_5G(j);
        den=den+AM_1_5G(j);
    end
    Weighted_Reflection(i)=(num/den).*100;
    fprintf(save_file,'%s\t %s\n',Sample_files(i).name ,Weighted_Reflection(i));
end
figure
plot(Weighted_Reflection,'gs','MarkerSize',10,'MarkerEdgeColor','b','MarkerFaceColor','b');
fclose(save_file);
end

```

C. Quokka 2 Analysis Code

Related to Section 3.6. Quokka 2 analysis setting code

```
% Quokka by Andreas Fell, the Australian National University
% MATLAB(R). (c) 1984 - 2012 The MathWorks, Inc.
version.design='FRC';
```

```
%%% Unit Cell Geometry
```

```
geom.dimensions=3; % set to 1, 2 or 3
geom.Wz=134;
geom.Wxfront=3*271;
geom.Wxrear=2*271;
geom.Wy=1626;
geom.frontcont.shape='line';
geom.frontcont.wx=50;
geom.rearcont.shape='full';
geom.meshquality=1;
```

```
%%% Bulk Material Properties
```

```
bulk.type='p-type';
bulk.rho=3;
bulk.taubfixed=1e20; % 1e20 to disable
bulk.SRH.midgap.taup0=1e20;
bulk.SRH.midgap.taun0=1e20;
bulk.T=300;
bulk.nk='Green08_300K';
bulk.Auger='Richter2012';
bulk.mobility='Klaassen'; % 'fixed'
bulk.nieff='default';
bulk.Brad=4.73E-15;
bulk.SRH.BO.Nt=0;
bulk.SRH.BO.m=2;
bulk.taubfixed=1e6; % Background lifetime us
```

%%% Front and Rear Boundries

```
bound.conduct{2}.location='front';
bound.conduct{2}.shape='full';
bound.conduct{2}.Rsheet=100;
bound.conduct{2}.jctdepth=1;
bound.conduct{2}.colleff=1;
bound.conduct{2}.cont.rec='J0';
bound.conduct{2}.cont.J0=1E-16;
bound.conduct{2}.cont.J02=0;
bound.conduct{2}.cont.rc=1e-12; % NOT effective
bound.conduct{2}.noncont.rec='J0';
bound.conduct{2}.noncont.J0=1E-16;
bound.conduct{2}.noncont.J02=0;
```

```
bound.conduct{1}.location='rear';
bound.conduct{1}.shape='full';
bound.conduct{1}.Rsheet=30;
bound.conduct{1}.jctdepth=10;
bound.conduct{1}.colleff=1;
bound.conduct{1}.cont.rec='J0';
bound.conduct{1}.cont.J0=1E-16;
bound.conduct{1}.cont.J02=0;
bound.conduct{1}.cont.rc=1e-12; %near zero % EFFECTIVE
```

%%% Generation Settings

```
generation.type='ext_file'% 'Jgen_surface';% 'customdata';%
generation.intensity=100;
%generation.Jgen=32.7;
generation.suns=1;
generation.ext_file='OPAL2\PVL_QuokkaGenFile.txt';          %%external file
generation.illum_side='front';
generation.shading_width=50;
%generation.customdata=[0.000586064, 0.001273005, 0.001492124, 0.00174896, 0.002050004,
0.002402866, 0.002816466, 0.003301257, 0.003869494, 0.00453554, 0.005316231, 0.006231301,
0.007303879, 0.008561078, 0.010034675, 0.011761918, 0.013786468, 0.016159498, 0.018940992,
0.022201258, 0.026022705, 0.030501928, 0.035752149, 0.041906077, 0.049119266, 0.057574042,
```

0.067484118, 0.079099991, 0.092715275, 0.108674123, 0.127379929, 0.149305518, 0.175005104,
0.205128295, 0.240436516, 0.281822253, 0.330331614, 0.387190769, 0.453836949, 0.53195477,
0.623518815, 0.730843552, 0.856641827, 0.962262663, 1.13509476, 1.379506795, 1.616957854,
1.89528077, 2.221510715, 2.603893805, 3.052095542, 3.577445124, 4.193221817, 4.914990615,
5.760995672, 6.752621468, 7.914933334, 9.277311038, 10.87419141, 12.74593882, 14.93986543,
17.51142715, 20.52562537, 24.05864999, 28.19980532, 33.05376737, 38.74322979, 45.41200516,
53.22866017, 62.39077649, 73.12994501, 85.71761978, 100.4719796, 117.7659704, 138.0367328,
154.4876397; 4.62E+21, 4.42E+21, 4.36E+21, 4.29E+21, 4.21E+21, 4.12E+21, 4.01E+21, 3.9E+21,
3.77E+21, 3.63E+21, 3.48E+21, 3.31E+21, 3.14E+21, 2.95E+21, 2.76E+21, 2.57E+21, 2.38E+21,
2.2E+21, 2.03E+21, 1.88E+21, 1.74E+21, 1.62E+21, 1.52E+21, 1.44E+21, 1.36E+21, 1.3E+21,
1.24E+21, 1.18E+21, 1.12E+21, 1.07E+21, 1.01E+21, 9.56E+20, 9.01E+20, 8.47E+20, 7.92E+20,
7.39E+20, 6.86E+20, 6.35E+20, 5.85E+20, 5.37E+20, 4.91E+20, 4.46E+20, 4.04E+20, 3.74E+20,
3.35E+20, 2.9E+20, 2.57E+20, 2.27E+20, 1.99E+20, 1.73E+20, 1.5E+20, 1.29E+20, 1.1E+20,
9.36E+19, 7.88E+19, 6.59E+19, 5.48E+19, 4.52E+19, 3.72E+19, 3.04E+19, 2.49E+19, 2.03E+19,
1.66E+19, 1.36E+19, 1.12E+19, 9.26E+18, 7.71E+18, 6.47E+18, 5.5E+18, 4.74E+18, 4.14E+18,
3.67E+18, 3.31E+18, 3.03E+18, 2.81E+18, 2.68E+18];

%%% External Circuit Settings

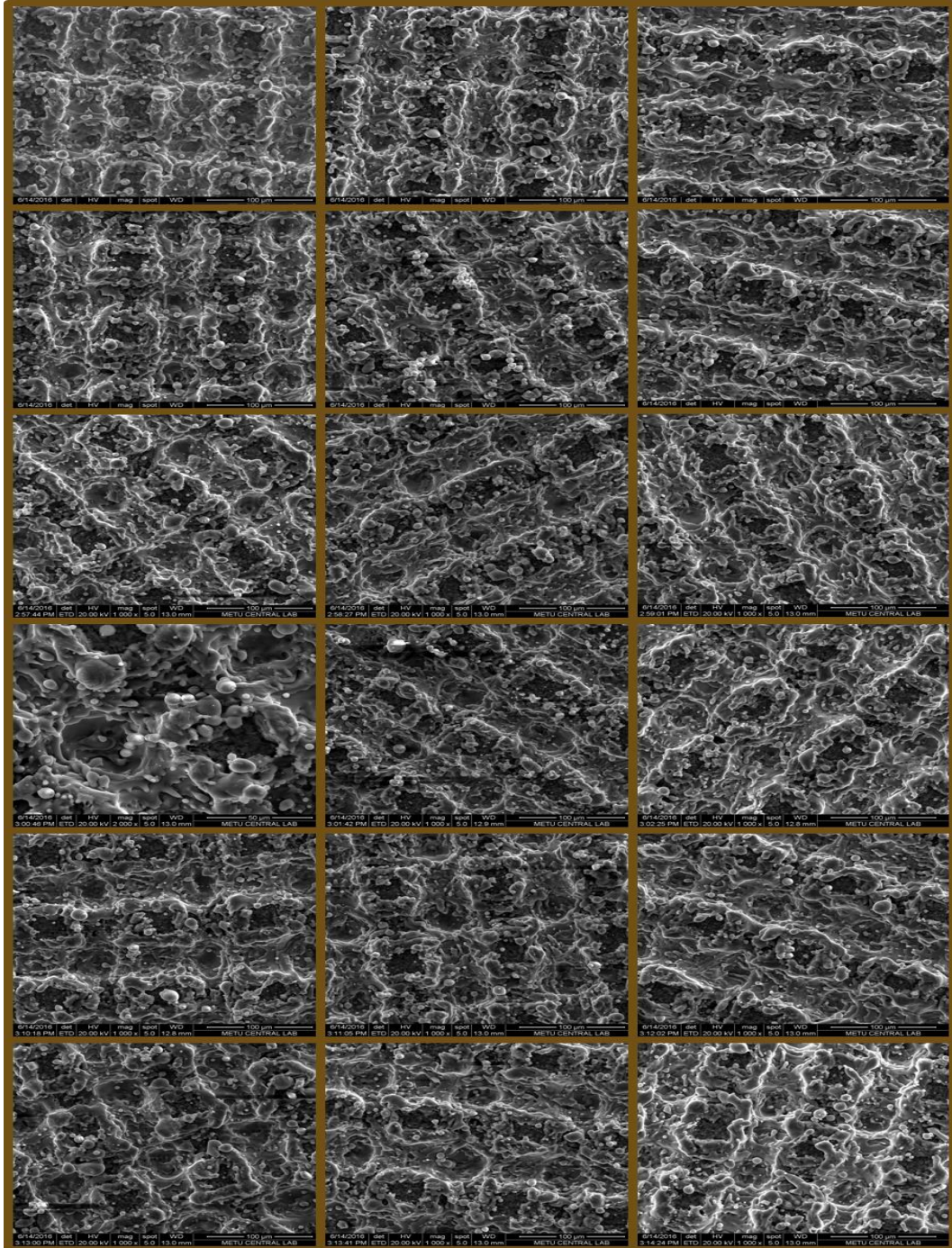
```

circuit.Rseries=0.1;
circuit.Rshunt=16000;
circuit.terminal='MPP';% 'IV_curve';
%circuit.Vuc.value=0.5;
%circuit.Vterm.value=0.5;
%circuit.Jterm.value=-30;
%circuit.IV.V_values=[0.4:0.05:0.6];
%circuit.sunsVoc.suns_values=[0.1:0.05:0.8];
%circuit.QE.wavelength_values=[300:25:1125];
%circuit.IV.mode='Vterm';
%circuit.IV.init_previous=0;
circuit.DJ0=0; % optional
circuit.Dn=2; % optional
circuit.Voc_guess=0.5;
circuit.IV_accuracy=5;

```


D. Uniformity Across Wafer

Related to Section 4.1.1. SEM Images to check uniformity across the wafer.



E. Post-Texture Cleaning

Related to Section 4.2. Top and cross section SEM Images to see the effects of post-texture cleaning.

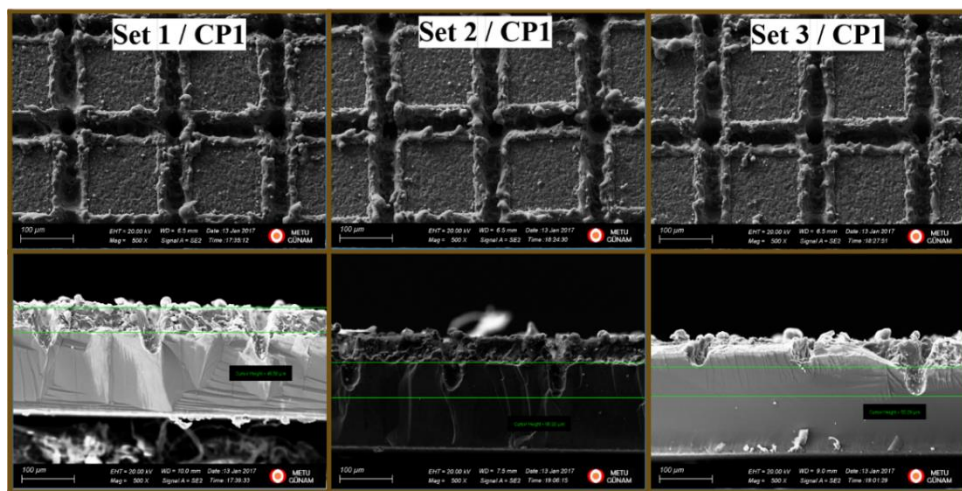
All samples are post-texture cleaned using 1% KOH solution at room temperature.

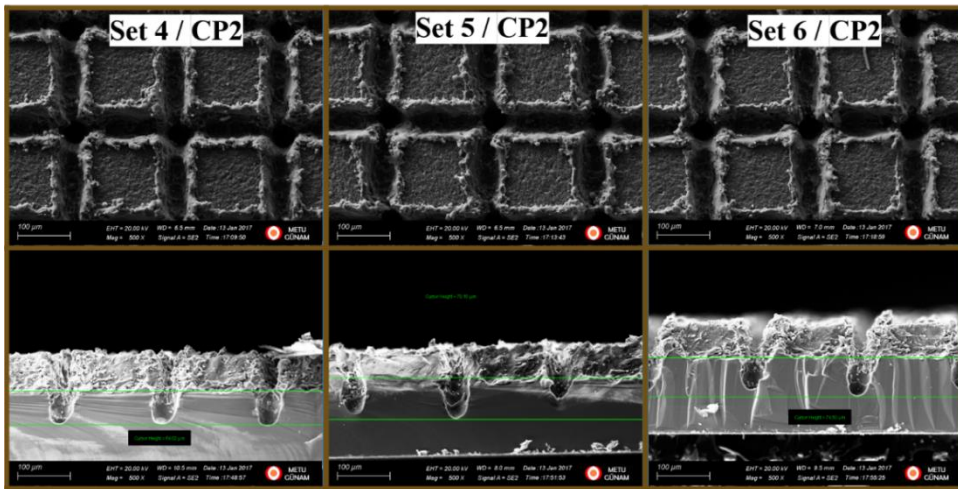
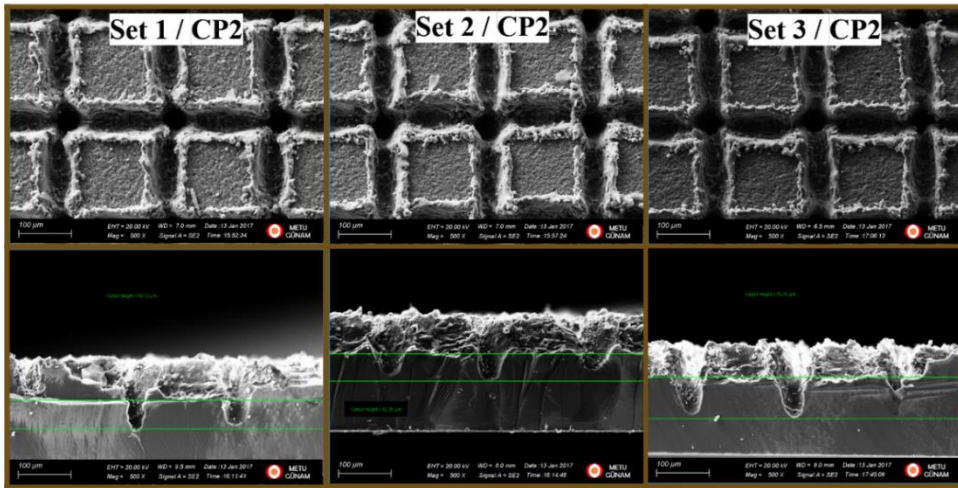
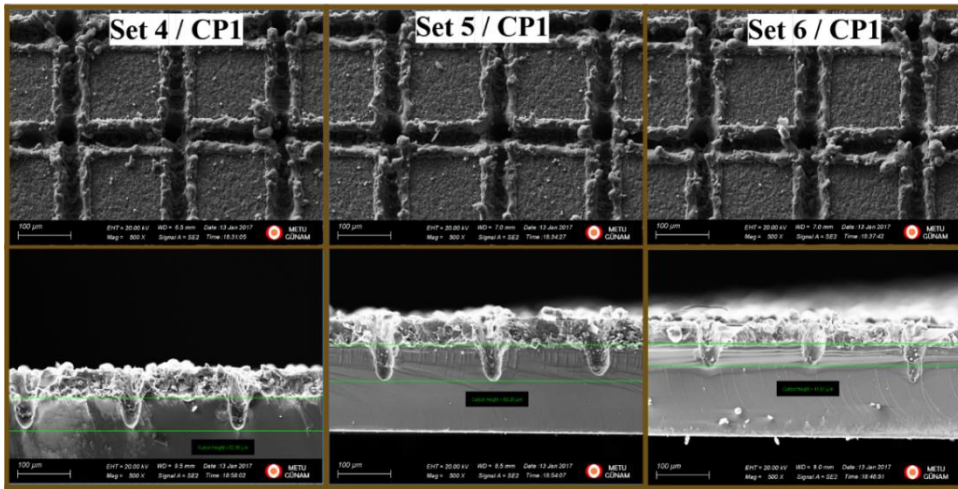
Table 0.1. Common laser texturing parameters for investigating post-texture cleaning

| | | <i>Frequency</i> | <i>Power</i> | <i>Pattern</i> | <i>Draw Step</i> | <i>Step Period</i> | <i>Line Spacing</i> | <i>Iteration</i> |
|--------------------|-----|------------------|--------------|----------------|------------------|--------------------|---------------------|------------------|
| | | <i>kHz</i> | <i>%</i> | | <i>LSB</i> | <i>μs</i> | <i>μm</i> | <i>#</i> |
| Common Parameter 1 | CP1 | 55 | 100 | Criss-Cross | 25 | 120 | 100 | 2 |
| Common Parameter 2 | CP2 | 55 | 100 | Criss-Cross | 25 | 120 | 100 | 3 |

Table 0.2. Changing laser texturing parameters for investigating post-texture cleaning

| | <i>Duration</i> | | <i>Duration</i> |
|-------|-----------------|-------|-----------------|
| | <i>s</i> | | <i>s</i> |
| Set 1 | 10 | Set 4 | 40 |
| Set 2 | 20 | Set 5 | 50 |
| Set 3 | 30 | Set 6 | 60 |

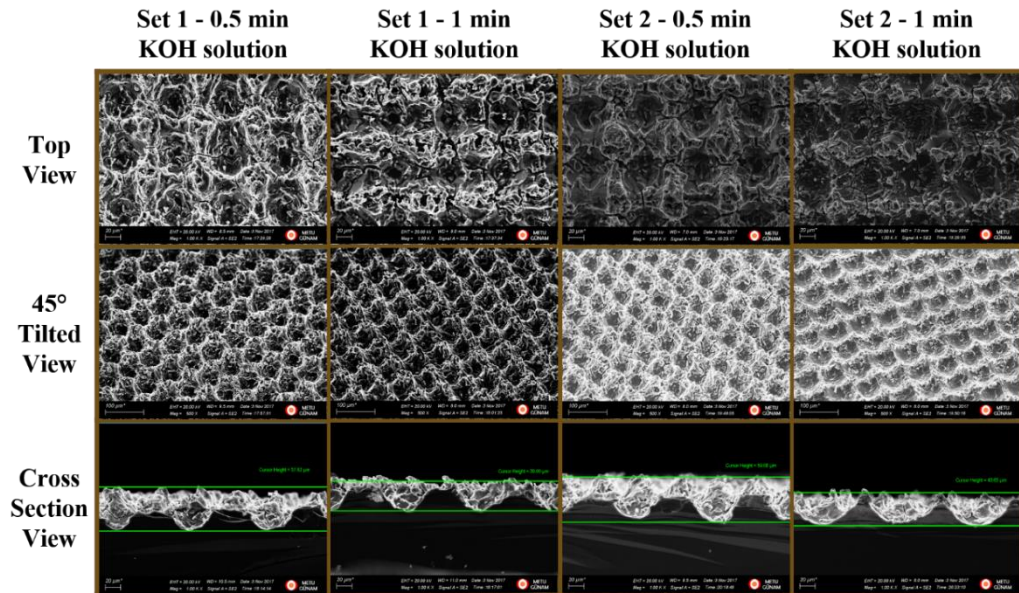




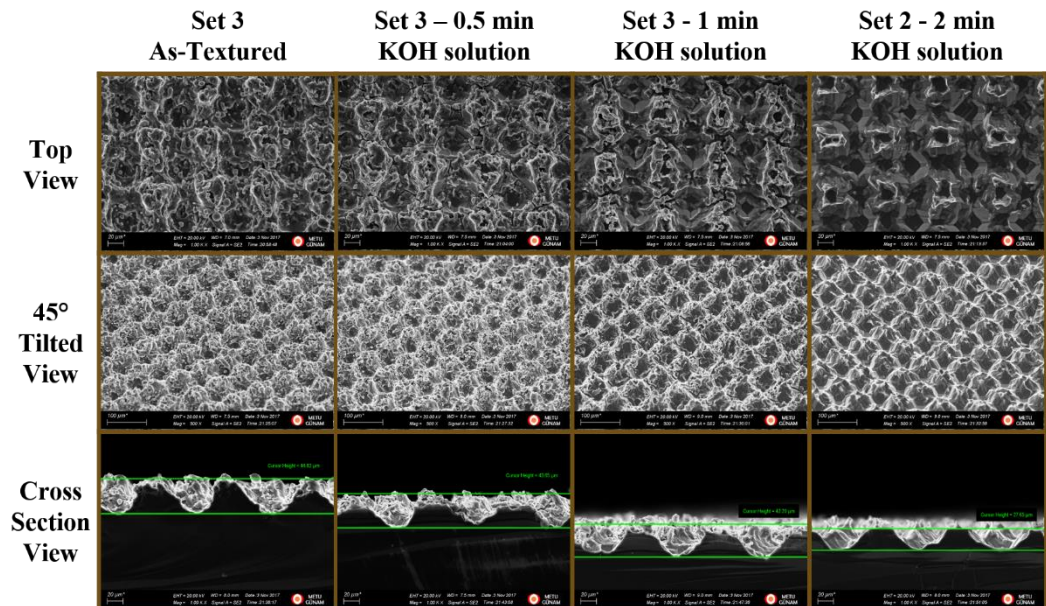
F. Effects of ARC and Passivation Layer

Related to Section 4.3.

- SEM Images of Set 1 and Set 2 post-texture cleaned for 0.5min and 1min.



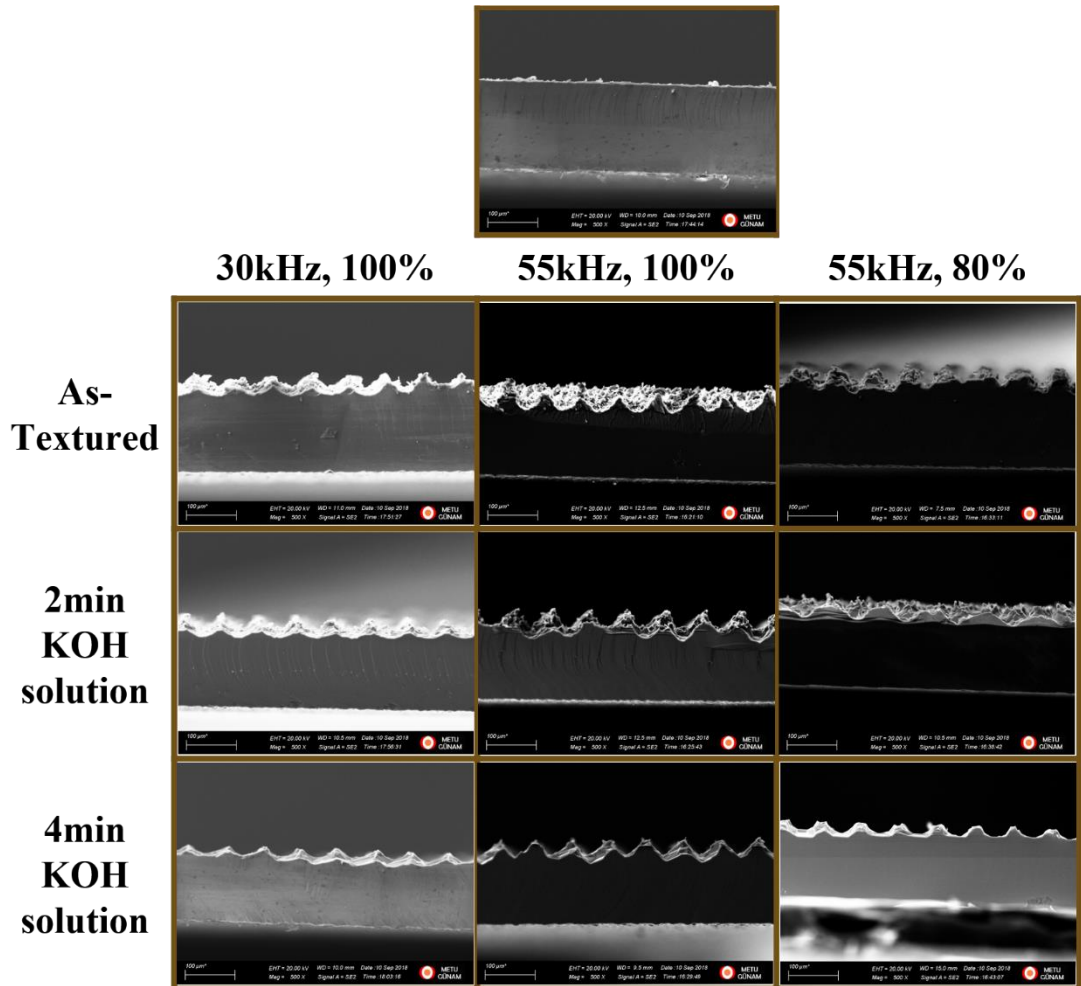
- SEM Images of Set 3 as-textured and post-texture cleaned for 0.5min, 1min, and 2min



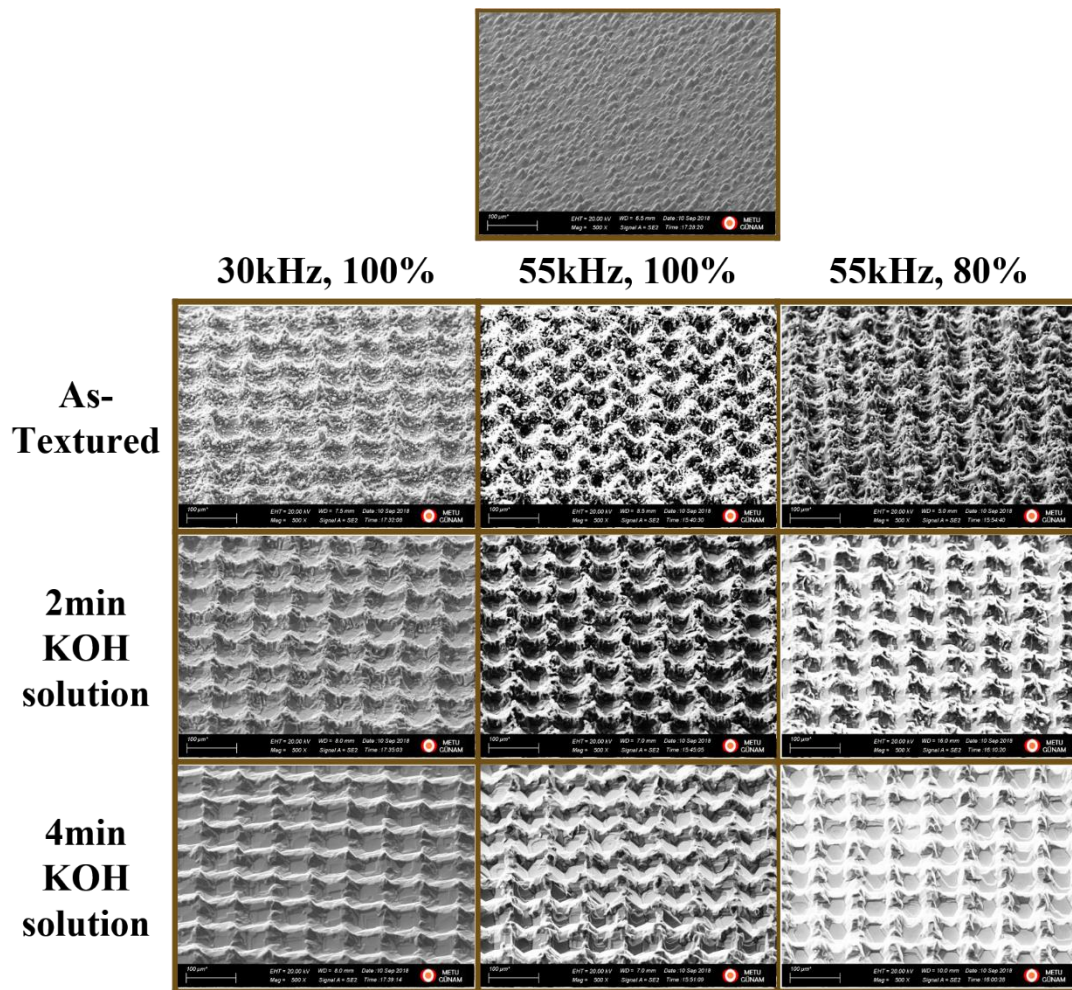
G. SEM Images of Solar Cells

Related to Section 4.4.

1. Top view SEM Images



2. Cross section view SEM Images



H. Reflection Curves of Solar Cells

Related to Section 4.4. Reflection curves of samples after post-texture cleaning.

